Université de Lille

École Doctorale ENGSYS

ULR 7512 - Unité Mécanique de Lille

Thèse

Présentée pour l'obtention du grade de DOCTEUR
DE L'UNIVERSITÉ DE LILLE

par

Thaynan Alves Oliveira

Implementation numérique sur des méthodes hybrides pour la simulation vibroacoustique en moyennes et hautes fréquences

---

Spécialité : Mécanique

Soutenue le 16 Septembre 2024 devant un jury composé de :

Rapporteur	**Prof. Dr. Eric Brandão**	(Universidade Federal de Santa Maria, UFSM)
Rapporteur	**Prof. Dr. Paulo Mareze**	(Universidade Federal de Santa Maria, UFSM)
Examinateur	**Prof. Dr. Erchiqui Fouad**	(Université du Québec)
Examinateur	**Prof. Dr. Raquel Lobosco**	(Universidade Federal do Rio de Janeiro)
Président	**Prof. Dr. Gilmar Mompean**	(Université de Lille, UML)
Directeur de thèse	**Prof. Dr. Mhamed Souli**	(Université de Lille, UML)

Affiliation :



Thèse effectuée au sein de **l'ULR 7512 - Unité Mécanique de Lille - Joseph Boussinesq (UML)**

de l'Université de Lille
Bâtiment ESPRIT
F-59000 Lille, France

In memory of my father Joni, my mother Neuza, and my aunt Eloá.

When education gives wings to transformation it is possible to fly further.
OZIRES SILVA

Résumé

La vibroacoustique fait référence à l'interaction entre les systèmes dynamiques solides et fluides qui propagent le son. La vibroacoustique classique s'est développée au fil des années à partir de méthodes déterministes et statistiques. Chaque technique a ses limites en termes de coût de calcul impliqué dans les simulations de systèmes complexes ou de représentativité des réponses dans différentes plages de fréquences d'analyse. Grâce à des techniques prédictives, différents phénomènes d'excitation présents en pratique peuvent être combinés pour évaluer le contenu acoustique ou vibratoire total dans un environnement donné. L'objectif de cette étude se concentre sur les approches numériques efficaces sur les méthodes hybrides dans le contexte de la vibroacoustique. La thèse envisage une gamme d'approches vibroacoustiques utilisées dans les secteurs académiques et industriels concernant la simulation efficace aux moyennes et hautes fréquences. Des modèles classiques de matériaux poreux et leur caractérisation ont été démontrés. La méthode des matrices de transfert (TMM) a été abordée dans le cadre de la modélisation des traitements de contrôle du bruit (NCT) dans des configurations multicouches. Dans ce contexte, une nouvelle fonction numérique a été proposée pour analyser des échantillons poreux finis, y compris des arrangements multicouches, ce qui a une application essentielle dans les environnements acoustiques réverbérants. Le couplage du TMM avec le SEA a également été abordé, sur la base de calculs de perte d'insertion, d'absorption acoustique et d'amortissement structurel du traitement considéré dans le sous-système d'origine. Enfin, le couplage de ces techniques informatiques efficaces avec la méthode des éléments finis (FEM) a été discuté. Il a été vérifié que les connexions FEM-SEA se produisent à partir de la matrice de rigidité dynamique de champ direct ajoutée à la rigidité dynamique du problème FE. De même, le couplage FE-TMM se produit à partir de l'ajout de la matrice dynamique du traitement. Une méthode basée sur les fonctions d'ondelettes a été utilisée pour calculer ces matrices de couplage, et une contribution numérique pour améliorer l'efficacité de calcul de la solution a été proposée. Plusieurs techniques d'analyse vibroacoustique ont été traitées. Les outils développés serviront de base à de futures recherches dans le cadre de cette thèse.

Numerical implementation of hybrid vibroacoustic methods for mid and high frequency analysis

Abstract

Vibroacoustics refers to the interaction between solid and fluid dynamic systems that propagate sound. Classical vibroacoustics has developed over the years from deterministic and statistical methods. Each technique has its limitations in terms of the computational cost involved in complex system simulations or the representativeness of responses in different analysis frequency ranges. Based on predictive techniques, different excitation phenomena present in practice can be combined to evaluate the total acoustic or vibrational content in a given environment. The objective of this study focuses in efficient numerical approaches on hybrid methods in the context of vibroacoustics. The thesis contemplate a range of vibroacoustic approaches used in the academic and industrial sectors regarding effective simulation at mid and high frequencies. Classical models of porous materials and the characterization were demonstrated. The transfer matrix method (TMM) was approached regarding the modeling of noise control treatments (NCT) in multi-layer configurations. In this context, a new numerical function was proposed to analyze finite porous samples, including multilayer arrangements, which has an essential application in reverberant acoustic environments. The coupling of TMM with SEA was also approached, based on calculations of insertion loss, sound absorption, and structural damping of the treatment being considered in the original subsystem. Finally, the coupling of these computational efficient techniques with the finite element method (FEM) was discussed. It was verified that the FEM-SEA connections occur from the direct field dynamic stiffness matrix being added to the dynamic stiffness of the FE problem. Similarly, the FE-TMM coupling occurs from the addition of the dynamic matrix of the treatment. A method based on wavelet functions was used to calculate these coupling matrices, and a numerical contribution for improving the computational efficiency of the solution was proposed. Several vibroacoustic analysis techniques were treated. The developed tools will serve as a basis for future research in the context of this thesis.

Aknowledgements

My parents, Joni and Neuza Oliveira, did not have the chance to see this work finished. I open this section by recognizing the importance that both of them had in my achievements. Their valuable legacy and affection gave me the strength to continue walking after their passing.

I am grateful to my wife, Tamara, for the love and strength she gave me during this period. To my son Davi for all the happiness provided in every smile. To my brother Joni, for teaching me to see the life from a different perspective.

I am thankful to the University of Lille, especially the Unité Mecanique de Lille and all its members, for the reception and great appreciation throughout my period in France. Thank you everyone for the pleasant moments.

I thank my supervisor, prof. Mhamed Souli, for the granted opportunity to be part of this institution, his tenacious help in the development of tools, and his human sensitivity in understanding my moments of most significant difficulty throughout this project.

I express gratitude to the committee members Eric Brandão, Paulo Mareze, Erichi Fouad, Azma Putra, Raquel Lobosco and Gilmar Mompeam, for giving their time to evaluate and make contributions to this work.

Thank you, professor Rogério Pirk, for encouraging me to take on this challenge and for all the support you gave me during the selection process.

Thank you Dalay, Dario, Mia and Vinícius for the friendship and essential help on my adaptation in France. I would like to thank Matheus Pereira for his valuable advice and exchange of experiences in the initial phase of this work.

Finally, thank all family members, work colleagues, friends, and people who contributed, supported, and encouraged this achievement.

Contents

1 Introduction **1**

Introduction **1**

1.1 Work contributions 3

1.2 Goals 4

1.3 Organization of the thesis 4

2 The Transfer Matrix Method (TMM) **7**

2.1 Introduction 7

2.2 Characterization of a porous sample 8

2.2.1 Acoustic Impedance 8

2.2.2 Reflection and absorption coefficients 10

2.2.3 Sound transmission through infinite porous samples 11

2.2.4 Classical models of fibrous materials 11

2.2.5 Classical experimental method for porous samples 14

2.2.6 Optimization of macroscopic parameters 16

2.2.7 Sound absorption analysis and the application of inverse methods 18

2.3 Transfer matrices 21

2.3.1 Fluid layer 23

2.3.2 Solid layer 23

2.3.3 Septum and thin plate layers 26

2.3.4 Poroelastic layer 26

2.4 Numerical procedure of the TMM 29

2.4.1 Assembling of the global transfer matrix 30
2.4.2 Applying the boundary conditions 33
2.4.3 Direct solution: intial condition 36
2.4.4 TMM indicators 36
2.5 Finite-size Transfer Matrix Method 37
2.5.1 Radiation impedance and size effects 38
2.5.2 Numerical procedure 39
2.5.3 Sound absorption of finite-size systems 40
2.5.4 Numerical improvements on FTMM integral comparable to Integral2 function 46
2.5.5 Sound transmission of a finite size system 48
2.6 Summary 52

3 Statistical Energy Analysis (SEA) 53
3.1 Introduction 53
3.2 SEA equations 54
3.2.1 Modal densities for structural plates and acoustic cavities . . . 57
3.2.2 Coupling factors for cavity-plate area connections 58
3.2.3 Dissipation loss factor 59
3.2.4 Energy variables 60
3.3 Case studies 60
3.4 SEA/TMM coupling 62
3.4.1 Sound absorption from the TMM 63
3.4.2 Insertion Loss (IL) from the TMM 64
3.4.3 Damping loss factor from TMM 69
3.5 Summary 70

4 Hybrid methods on vibroacoustics 73
4.1 Introduction 73
4.2 The Finite Element Method applied to hybrid techniques 74
4.2.1 Response to random excitations 76

4.2.2 Modal finite element method 77
4.2.3 Hybrid FE-SEA 79
4.2.4 Direct-field dynamic stiffness using wavelet functions 81
4.2.5 Direct-field dynamic stiffness using the space integration 88
4.2.6 The Hybrid FE-SEA step-by-step 90
4.2.7 FEM and SEA subsystems 94
4.2.8 Case of a SEA cavity coupled to FE 96
4.3 Hybrid FE-TMM 98
4.3.1 Fundamentals 100
4.3.2 Locally reacting FE/TMM 102
4.3.3 Modal FE/TMM 103
4.3.4 Non-locally reacting FE/TMM 103
4.3.5 Analysis and discussion 104

Conclusions and perspectives **107**

A Numerical examples in Octave/Matlab **111**
A.1 Simple TMM plate-fiber problem 112
A.2 Importing the Insertion Loss to the SEA model 116

Bibliography **129**

Chapter 1

Introduction

The dynamic analysis of complex vibroacoustic systems is a technique of great interest in academic and industrial environments. In the academy, new solutions concerning mathematical formulations and numerical alternatives to improve computational efficiency have been constantly studied, expanding current techniques to cover the analysis of more complex systems. In the industrial field, computational vibroacoustic methods are essential to define project and design parameters, acoustic and vibratory environment predictions, and noise and vibration control strategies in new products and systems.

Vibroacoustics refers to the interaction between solid and fluid dynamic systems that propagate waves. The ability of a moving structure to generate sound when in contact with an elastic fluid is characterized by radiation, which controls the vibroacoustic coupling. When coupled to a fluid medium, this structural system changes its dynamic properties, such as damping and mass, experimenting with fluid loading and dynamic forces if sound waves propagate close to the structure Atalla [2017].

Classical vibroacoustics has been developed over the years from deterministic and statistical methods Hambric et al. [2016]. Each technique has limitations regarding the computational cost involved in complex system simulations or the representativeness of responses in different analysis frequency ranges. Classical deterministic methods consider the calculation of local system responses, making them unfeasible in high frequency since the necessary number of representative points of the global system grows with the maximum analysis frequency. In contrast, statistical methods are based on mean responses or variances of global systems, which makes them imprecise in low-frequency responses dominated by local modes.

Considering deterministic techniques, the finite element method (FEM) and boundary element method (BEM) are prevalent Atalla and Sgard [2015]. FEM uses the discretization of a complex domain in elements characterized by simpler mathematical formulations. This potential for representing any system from interconnected elements makes the method robust and globally used in multiphysics simulations. BEM, in turn, considers the discretization of a single boundary and uses mathematical functions capable of representing the rest of the domain to calculate the response outside this boundary Alia [2006]. In vibroacoustics, Green's functions are used to characterize the response at any point of a fluid environment, not requiring its complete discretization as in the finite element method.

The Transfer Matrix Method (TMM) is a suitable alternative for high frequencies. TMM is a classic method that considers simple solutions of the wave equation of different physical systems, evaluated at two specific points, to characterize transfer matrices of a fluid, solid or porous domain Allard and Atalla [2009]. This method is widely used in vibroacoustics to model multi-layer systems of noise control treatments quickly and efficiently based on the weak coupling between layers and energy exchange between them.

Another traditional computational method of vibroacoustics is Statistical Energy Analysis (SEA) Fahy [1994]; Lyon et al. [1995]; Pirk and Souto [2014]. SEA applies to high frequencies based on the power exchange between physical domains called subsystems that represent components of the product under analysis. These subsystems allow for estimating acoustic or vibrational responses of specific spatial regions of the global model from its calculated average energy. This method stands out for its computational efficiency and simplicity, allowing preliminary knowledge of the product with a low level of detail, being entirely appropriate in the design phase.

Different excitation phenomena present in practice can be combined to evaluate the total acoustic or vibrational content in a given environment through vibroacoustic techniques. In aeronautical/aerospace engineering, the turbulent boundary layer (TBL) exciting an aircraft in flight can be represented as a structural load over the fuselage. It is possible to consider air-borne and structure-borne noise from engines and systems as well Cordioli et al. [2004a]; Pirk and Souto [2014].

In the automotive industry, powertrain noise and air-borne noise from tires and exhaust can be characterized and applied as excitation to obtain an estimate of the internal acoustic environment of the final vehicle Cordioli et al. [2004b]; Rao [2003]. Other product development industries also use vibroacoustic tools to get useful predic-

tive information for directing the project design phases.

1.1 Work contributions

The initial proposal of this work considers a context for creating and documenting new tools, starting from a statistical energy analysis code in the initial development phase referenced as SEA-module, for vibroacoustic simulation at medium and high frequencies. A first version of this code was proposed by Massahel [2016] in a partial contribution of his doctoral thesis. The orginal code have SEA point, line, area junctions, which provides basic connection between structural and acoustic subsystems. Previous research on vibroacoustics at the research unity is also complemented by a full Boundary Element Method framework developed by Alia [2006].

In this thesis, SEA-module was improved in terms of implementing noise control treatments being applicable to SEA connections. Material characterization strategies, as using optimization, was presented. Infinite-size and finite-size transfer matrix method was studied, to allow considering this class of materials in full vibroacoustic models. In this context, a new form of the transfer matrix of a solid layer was proposed, through a symbolic calculation.

In the ambit of TMM, a remarkable contribution of this work presented a new Finite-Size Transfer Matrix Method (FTMM) numerical function on the computation of the sound absorption coefficient and transmission loss for finite size samples under diffuse field conditions, including analysis for multi-layer systems. The exposed results demonstrated good agreement with experimental data, and the computational efficiency of the numerical approach demonstrated good performance taking into account different implementation procedures available in the literature.

Concerning SEA-TMM connections, three indicators are involved in the application of noise control treatment (NCT) on a solid surface: the sound insertion loss (IL), the absorption coefficient and the damping loss factor of the structural system. A complete framework was presented to model these parameters in order to have a full vibroacoustic prediction using computational efficient methods.

Expanding the vibroacoustic analysis, hybrid vibroacoustic methods merging finite elements (FE) and SEA (FE-SEA) and TMM (FE-TMM) were investigated. These methods are dependent of a proper dynamic stiffness matrix to be added to the FE part. An important contribution of this work on this topic is related to the numerical

calculation of the parameter, considering convergence of the real and imaginary part. A variable discretization along a single wavenumber grid was proposed in order to have good convergence of the full complex matrix. The new proposal avoids using a large number of Gauss points in the integration domain to have a proper convergence of the parameter.

1.2 Goals

- Validating and improving SEA-module;
- Implementation of porous materials on SEA-module considering a new in-house Transfer Matrix Method (TMM) tool to predict and apply noise control treatment responses on a SEA model. The TMM tool considers:
  - Classical equivalent fluid models;
  - Full implementation of poroelastic materials;
  - Finite-size Transfer Matrix Method (FTMM), with new numerical contributions.
- Application of porous models with experimental and inverse techniques;
- Modal form of finite elements (FE) and investigation of hybrid methods on SEA-module considering Hybrid FE-SEA and Hybrid FE-TMM approaches.
  - New contributions on the numerical calculation of the Dynamic Stiffness Matrix of a SEA cavity on the Hybrid FE-SEA;
  - Implementation of the FE-TMM in modal domain, using the same approach to calculate the Dynamic Stiffness Matrix of the noise control treatment.

1.3 Organization of the thesis

Chapter 2 brings a study on the application of the transfer matrix method in vibroacoustic analysis, as well as the implementation of these methods and their considered models. This chapter discusses different techniques for modeling treatments for noise control, such as equivalent fluid, poroelastic and solid elements. This chapter also studies TMM applied to samples of finite size, where analyses of the computational

efficiency of the implemented techniques are presented. Chapter 3 deals with Statistical Energy Analysis and the vibroacoustic coupling between SEA and TMM models. A case study is evaluated considering the sound transmission loss of a SEA+TMM system. An example MATLAB/OCTAVE code for the system covered in this study is provided in the Appendix. The structural damping imposed by treatment when coupled to the structure is also investigated in Chapter 3. Chapter 4 brings the application of hybrid methods, considering the finite element modal approach (FEM) as a deterministic basis. The first part of Chapter 4 deals with the FE-SEA coupling based on the calculation of the dynamic stiffness matrix of the direct and reverberant fields, where two numerical approaches were investigated and compared. In the second part of Chapter 4, the FE-TMM hybrid method is exposed, based on three numerical techniques implemented. Finally, in Chapter 5 are the conclusions regarding the proposed study and suggestions for future work.

Chapter 2

Transfer Matrix Method (TMM)

Partial content of this chapter was published in the following Oliveira [2021]

Author	Thaynan A. Oliveira
Title	Noise control treatments modeling using statistical energy analysis and the transfer matrix method
Book	Multiphysics Simulations in Automotive and Aerospace Applications
Editors	Mojtaba Moatamedi, Thurai Rahulan and Hassan Khawaja

2.1 Introduction

Passive noise control treatments are widely used in aerospace and automotive industries, whose primary function is the dissipation of vibration (or acoustic) energy of a vibroacoustic system. Sound packages containing a sequence of high dissipative porous materials and thin solid layers are generally employed to combine the high energy loss into a poroelastic media with the sound insulation capacity of double-wall systems.

For high-frequency analysis, analytical methods are generally used for the performance assessment of a noise control treatment. The Transfer Matrix Method (TMM) is a valuable tool capable of characterizing a multilayer treatment from the resolution of a simple linear system. Computational efficiency makes this method extensively used in industrial applications for design purposes Blanchet and Feist-Muench [2020]; Cordioli et al. [2004a]. This chapter presents an overview of the TMM approach combined with classical semi-phenomenological models of porous media. Experimental and numerical techniques for obtaining sound absorption and transmission results of porous samples

are detailed.

The characterization of porous samples regarding their acoustic parameters is first presented. Natural kenaf fibers are used as the test material, and the proposed methodology is applicable to other natural fibers. The modeling technique employs the inverse method using the Johsnon-Champoux-Allard model Mareze [2013]; Pereira et al. [2019], where five acoustical parameters are obtained from an optimization process from the experimental data of sound absorption coefficient. It is demonstrated that the inverse method can be used as a fast and practical solution for the acoustic characterization of new materials. The transfer matrix method (TMM) is then employed as an alternative to model multilayer treatments since the characterization process of individual samples is done.

This chapter also provides an estimation of the finite-size response of a porous material based on the radiation impedance of rectangular samples. This technique, well known as Finite-size Transfer Matrix Method (FTMM) Allard and Atalla [2009]; Ghinet and Atalla [2001]; Rhazi and Atalla [2010], can make it possible to model the diffuse-field response of the material numerically with the assumption of the finite lateral extent of the samples to capture the diffraction effects on the edges, that proved to have significant contributions to the response, mainly at low frequencies, when considering experimental conditions.

2.2 Characterization of a porous sample

This section discusses the theory of sound propagation through porous media. The concepts of acoustic impedance are presented, and the importance of that parameter to describe more usual indicators, like the absorption and reflection coefficients, is discussed. Some semi-phenomenological models of porous media are mentioned, as well as the macroscopic properties that constitute the fluid phase of a porous material. From these theoretical models, it is possible to characterize a medium that can be used to approximate the indicators of a SEA subsystem.

2.2.1 Acoustic Impedance

The concept of impedance appears in several areas of engineering. It is given by the ratio between a potential quantity and a kinetic quantity. In acoustics, the variable that can be associated with potential energy is the sound pressure and the one associated to

the kinetic energy is the particle velocity or volume velocity. There are different types of acoustic impedance. The *point* or *specific impedance* is given by the ratio between effective sound pressure and particle velocity (both in frequency domain) at a single point located inside an acoustic medium Beranek [1954], that is

$$\tilde{Z}(f) = \frac{\tilde{p}(f)}{\tilde{u}(f)} \qquad \mathrm{Ns/m^3\ or\ rayls}\ , \tag{2.1}$$

where $\tilde{Z}(f)$ is the complex specific impedance, $\tilde{p}(f)$ is the sound pressure and $\tilde{u}(f)$ the particle velocity at the point.

The *characteristic impedance* Z_c is general quantity related to the acoustic medium. That one represents the the ratio pressure/velocity when we consider free field propagation of plane waves inside the fluid medium Beranek [1954]. The relationship between Z_c and the physical properties of the fluid is given by

$$Z_c = \rho\, c \ \ [rayls]\ , \tag{2.2}$$

with ρ being the density function and c the sound velocity in the propagating medium.

Surface impedance

The surface impedance is the most important parameter for the acoustic characterization of a porous sample. From this parameter, it is possible to calculate the reflection and the absorption coefficient and, in some cases, the transmission loss of a porous treatment Allard and Atalla [2009]. This quantity is given by the ratio of the sound pressure to the normal particle velocity at the surface between two medias. An example is given by considering a porous interface between a fluid and a rigid wall, represented by the Figure 2.1.

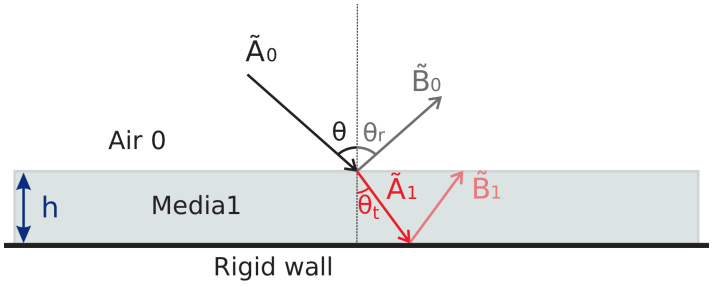

Figure 2.1: Sample between the fluid and the rigid wall.

The Figure 2.1 shows a fluid, e.g. the air (0), in contact with a porous material with thickness h_1 (media 1) backed by a rigid surface. The variable $\tilde{A}_0$ is the complex wave amplitude that incides on the material with angle θ relative to the normal direction in the air 0. Part of the wave is reflected to 0, with amplitude B_0 and $\theta_r = \theta$ if assuming smooth surface. A portion of energy is refracted to the media 1, with A_1 and θ_t being the amplitude and the angle of this wave. The rigid wall is perfectly reflective and B_1 is the amplitude of the reflected wave inside the material. The surface impedance for this problem, is given by

$$\tilde{Z}_s(\omega) = -\mathrm{j}\,\frac{\tilde{Z}_c}{\cos\theta_t}\cot(\tilde{k}_c\cos(\theta_t)h)\ , \tag{2.3}$$

where $\tilde{k}_c = \omega/\tilde{c}$ is the complex wave number in the media 1, $\tilde{Z}_c$ is the characteristic impedance of the porous sample and $\mathrm{j} = \sqrt{-1}$ is the complex operator.

2.2.2 Reflection and absorption coefficients

The reflection coefficient R is a quantity that contains the relevant acoustic properties to express how much the surface reflects the sound wave. When $|R| = 1$, the surface is perfectly reflective like a rigid wall Kuttruff [2007]. Considering the situation presented in Figure 2.1, this parameter can be computed as

$$R = \frac{\tilde{Z}_s\cos\theta_i - \rho_0 c_0}{\tilde{Z}_s\cos\theta_i + \rho_0 c_0} \tag{2.4}$$

with $\tilde{Z}_s$ the surface impedance of the sample Allard and Atalla [2009].

Another important quantity to be presented in this section is the sound absorption coefficient. This amount represents the fraction of incident energy that is not reflected by the sample, related to the energy dissipation into the material or the transmission of the sound wave through the media Kuttruff [2007]. Considering the sample between air and rigid surface (2.1), the absorption coefficient α will be

$$\alpha = 1 - |R|^2\ . \tag{2.5}$$

In this case, all the energy that is not reflected to the medium 0 is dissipated by the material, since it is on a rigid wall. This is one of the mechanisms that provide mathematical support for impedance tube measurements.

2.2.3 Sound transmission through infinite porous samples

The sound transmission is also a very important concept in noise control. When an incident wave with acoustic power W_i excites a dissipative sample composing a partition between two elastic mediums, a portion of the energy is absorbed into the material generating a dissipated power W_d, and a parcel of the incidence amplitude is transmitted, represented by the power W_t, as illustrated in Figure 2.2.

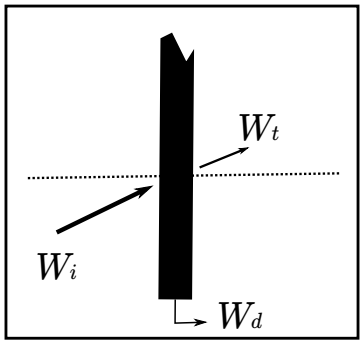

Figure 2.2: Power balance in a simple transmission problem.

In this context, we are interested in the barrier capacity of the sample, which can be represented by the ratio of the acoustic power in back and front of the wall. From this definition, an important parameter can be introduced as the sound transmission coefficient τ given by

$$\tau = \frac{W_t}{W_i} \, . \tag{2.6}$$

The sound transmission loss (TL) of a system excited by a plane wave impinging at an incidence angle θ is calculated in logarithmic scale as

$$TL(\omega, \theta) = 10 \log_{10} \left(\frac{1}{|\tau(\omega, \theta)|^2} \right) = -10 \log_{10}(|\tau(\omega, \theta)|^2) \, . \tag{2.7}$$

The transmission loss is positive when the transmitted power is smaller than the incidence power, which results in a transmission coefficient smaller than 1.

2.2.4 Classical models of fibrous materials

There are several semi-phenomological models designed to characterize the acoustic behavior of porous materials. These models take into account macroscopic properties, and consideration of parameters varies from different theories. This section presents the

semi-empirical model of Delany-Bazley, which is one of the simplest in terms of calculation, and also the Jhonson-Champoux-Allard model, which considers five macroscopic parameters to characterize the sound propragation in the porous media: the flow resistivity σ, porosity ϕ, tortuosity α_∞, dissipation characteristic length Δ, and thermal characteristic length Δ'.

Delany-Basley Model

In the Delany-Basley model, the acoustic characteristics of the sample depend entirely on the flow resistivity σ Delany and Bazley [1970]. The characteristic impedance Z_c can be obtained from the Equation (2.8)

$$Z_c = \rho_0 c_0 \left[1 + 0,057 \left(\frac{\rho_0 f}{\sigma}\right)^{-0,754} - \mathrm{j}\ 0,087 \left(\frac{\rho_0 f}{\sigma}\right)^{-0,732}\right], \tag{2.8}$$

as well as the characteristic wave number of the sample k_c

$$k_c = \left[1 + 0,0978 \left(\frac{\rho_0 f}{\sigma}\right)^{-0,700} - \mathrm{j}\, 0,189 \left(\frac{\rho_0 f}{\sigma}\right)^{-0,595}\right] k_0, \tag{2.9}$$

where σ is the flow resistivity.

Johnson-Champoux-Allard (JCA) Model

The JCA model is more sophisticated compared to the Delany-Basley model as it incorporates the five parameters which are able to influence the sound propagation within the porous material. Johnson et al. [1987] present the effective density parameter ρ_{ef}, given by

$$\rho_{ef} = \rho_0 \left[\alpha_\infty + \frac{\nu\phi}{\mathrm{j}\ \omega q_0}\left(1 + \frac{4\,\alpha_\infty^2 q_0^2}{\Lambda^2 \phi^2 \nu}\,\mathrm{j}\,\omega\right)^{1/2}\right]. \tag{2.10}$$

where $\nu = \eta/\rho_0$ is the kinematic viscosity of the medium, $\eta = 1.8410^{-}5\,[\mathrm{Pa\,s}]$ is the static viscosity of the air, the viscous permeability of the fiber q_0 may be approximated by $q_0 = \eta/\sigma$. Allard and Champoux [1992] present the effective bulk modulus K_{ef}, given by

$$K_{ef} = \gamma P_0 / \left[\gamma - \frac{\gamma - 1}{1 + \frac{\nu'\phi}{\mathrm{j}\,\omega q_0'}\left(1 + \frac{\mathrm{j}\,\omega(\Lambda')^2}{16\nu'}\right)^{1/2}}\right], \tag{2.11}$$

where $\nu' = \nu/\mathrm{Pr}$ is the thermal viscosity, $\mathrm{Pr} = 0.77$ is the Prandtl number, q'_0 is the thermal permeability which is given by $q'_0 = \phi(\Delta')^2/8$ under the hypotesis that the pores can be approximated by circular cross-shaped tubes.

The characteristic impedance and the complex wave-number of a porous sample is computed from the equivalent fluid theory as Zwikker and Kosten [1949]

$$\tilde{Z}_c = \frac{\sqrt{\rho_{ef} K_{ef}}}{\phi} , \tag{2.12}$$

$$\tilde{k}_c = \frac{\omega\sqrt{\rho_{ef}/K_{ef}}}{\phi} . \tag{2.13}$$

Figure 2.3 shows a comparison of the normal incidence absorption coefficient ($\theta_i = 0$) for a fibrous material, calculated from the models presented in this section. The material properties considered for this simulation is given by the Table 2.1.

Table 2.1: Material properties.

	σ	ϕ [%]	α_∞ [-]	Λ [μm]	Λ' [μm]
Glass fiber	22000,0	98,0	1,1	105,0	340,0

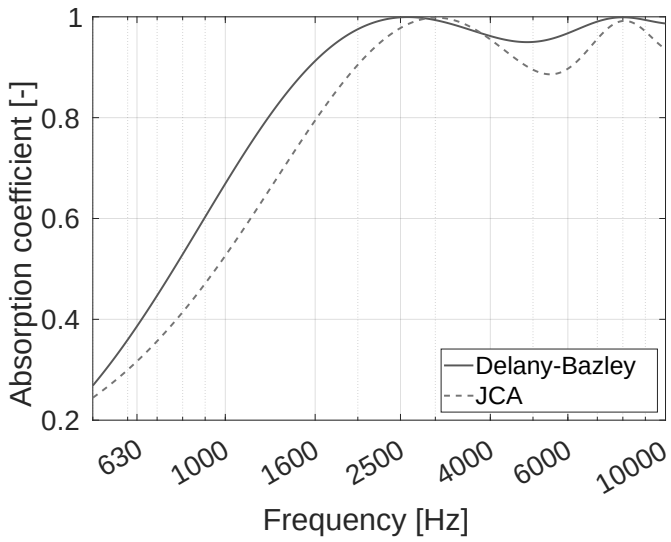

Figure 2.3: Sound absorption coefficient computed from the Delany-Bazley model and Johnson-Champoux-Allard (JCA) model for a 30 mm thick glass fiber.

As it can be seen in Figure 2.3, there are some important differences between the two models. However, if considering a statistical point of view, the result shown

a similar tendency for both curves. The Delany-Bazley approach can be seen as a simplest but useful tool for representing fiber materials in some applications on SEA.

2.2.5 Classical experimental method for porous samples

The Transfer Function Method is a very traditional approach for acoustic characterization of porous materials in impedance tubes. This procedure is standardized by the ISO 10534-2 (*Determination of Sound Absorption Coefficient and Impedance in Impedance Tube*) 2001. Such an apparatus allows considering plane waves in a limited frequency range of analysis and, consequently, normal incidence of sound to the surface of the tested sample.

The standardized measurement consists of an impedance tube with sufficiently rigid walls equipped with a loudspeaker at one side and porous material at the other. Two microphones for capturing the sound signal are also demanded, as shown in Figure 2.4.

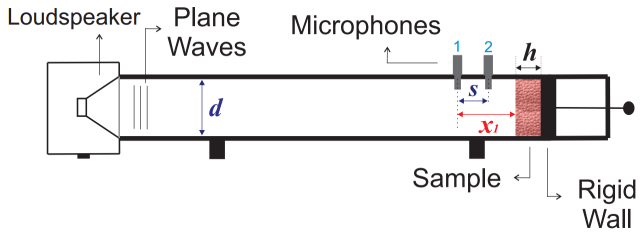

Figure 2.4: Impedance tube aparattus acording to ISO 10534-2. Adapted from (Thaynan Oliveira [2016]).

Figure 2.4 illustrates two microphones spaced at a distance s, with Microphone 1 at a distance x_1 from the sample, which has a thickness h. The tube has a diameter d, which allows the calculation of the maximum frequency of analysis so that plane waves can be considered inside it (cutoff frequency). This frequency, according to ISO 10532-2 is given by:

$$f_c = \frac{1,84\, c_0}{\pi\, d}\ , \tag{2.14}$$

where f_c is the cutoff frequency of the tube and c_0 m/s is the speed of sound in the air. In addition to the cut-off frequency, the spacing between microphones also influences the analysis frequency, as can be seen in the standard.

The method described in ISO:10534-2 [2001] would be feasible from a simple

transfer function $H(f)$ between the microphones, given by:

$$H(f) = \frac{P_2(f)}{P_1(f)} \ , \tag{2.15}$$

$P_1(f)$ and $P_2(f)$ being the pressures collected by Microphones 1 and 2, respectively, in the frequency domain.

However, it is recommended that there is a kind of calibration to the transfer function, from the exchange of positions between microphones, due to possible errors that may be associated with non-identical responses between sensors and channels of the acquisition system. In this way, a new measurement is performed with the inverted position of the sensors and the calculation shown in Equation (2.15) is performed, resulting in a new transfer function $H^*(f)$. The calibrated transfer function H_{12}, in this way, is given by

$$H_{12}(f) = \frac{[H(f)]^{0,5}}{[H^*(f)]^{0,5}}. \tag{2.16}$$

The sound absorption coefficient is derived from the reflection coefficient R. This parameter, in turn, can be obtained from the calibrated transfer function, Equation (2.16), since the properties such as the wave number in the air ($\widetilde{k}_0$) and the distance between the microphones s are known. Reflection coefficient is then calculated, according to the ISO 10534-2 2001 recommendation

$$R = \frac{H_{12}(f) - \mathrm{e}^{-\mathrm{j}\,\widetilde{k}_0 s}}{\mathrm{e}^{\mathrm{j}\,\widetilde{k}_0 s} - H_{12}(f)}\,\mathrm{e}^{2\widetilde{k}_0 s} \ , \tag{2.17}$$

where $\widetilde{k}_0$ is the normalized complex wave number in air, given as

$$\widetilde{k}_0 = \left(\frac{\omega}{c_0}\right) - \mathrm{j}\ 0,0194\left(\frac{\sqrt{f}}{c_0\, d}\right) \ , \tag{2.18}$$

with f being the frequency in Hertz and $\omega = 2\pi f$ is the angular frequency under analysis. From the reflection coefficient R, the surface impedance Z_s of the material can be obtained from

$$\tilde{Z}_s = \frac{1-R}{1+R}. \tag{2.19}$$

Thus, the absorption coefficient can be estimated by considering normal incidence from

$$\alpha = 1 - |R|^2 \ . \tag{2.20}$$

In addition to the calculations presented in this section, the standard ISO 10534-2 2001 also sets out a series of precautions and good practices for carrying out measurements for the characterization of porous materials.

2.2.6 Optimization of macroscopic parameters

The identification of macroscopic parameters of porous materials from measurements in an impedance tube is a widely used method concerning the characterization Allard and Atalla [2009]; Mareze [2013]. In this scenario, the method based on the adjustment of curves using a propagation model, usually rigid or limp structure, stands out. The optimization method uses the measured surface impedance or absorption coefficient from the test sample as parameters to define the objective function.

The accuracy of the method will depend on the chosen model and the cost of the used function in the inverse algorithm. The model needs to represent the measured acoustic properties, that is, should be sufficiently sensitive to variations of the parameters. The most common phenomenological models consider rigid frame for the solid structure of the fiber and incorporates five macroscopic fluid parameters, namely:

a. Flow resistivity, σ

b. Porosity, ϕ

c. Tortuosity, α_∞

d. Viscous characteristic length, Λ

e. Thermal characteristic length, Λ'

A sensitivity analysis of the absorption coefficient as a function of these five main macroscopic parameters is presented in Figure 2.5.

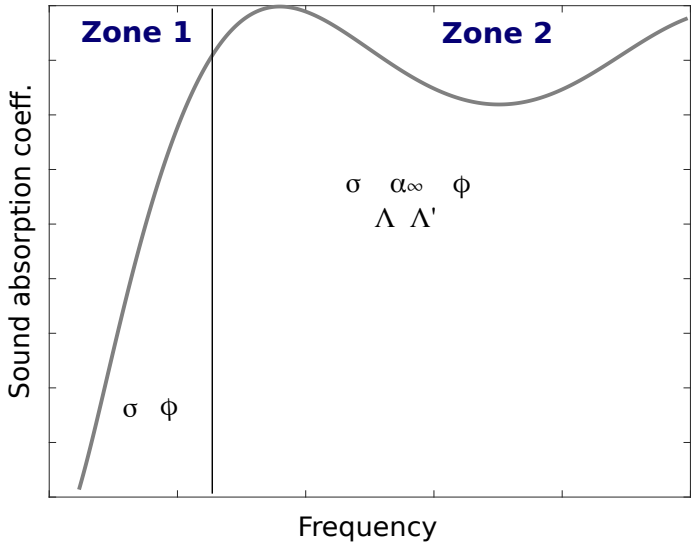

Figure 2.5: Importance of macroscopic parameters in the sound absorption coefficient.

Figure 2.5 is an adaptation of a graphic based on simulation of various porous materials adopting a rigid structure model Atalla [2017]. This demonstrates that the low frequency is sensitive to the flow resistivity σ and porosity ϕ, while the tortuosity α_∞, viscous length Λ and thermal length Λ' affect the level of absorption coefficient at medium and high frequencies. The presentation of this trend is important for evaluating if the impedance tube used in the characterization has a proper cutoff frequency for computing the required variables. If the cutoff frequency is low, it is evident that the measured data can be insufficient in the spectral range in which these parameters have significant effect. According to Mareze [2013], the determination of the characteristic lengths is quite complex and may be inaccurate using the genetic algorithm, but such a method becomes an important tool when direct measurements are not viable.

The objective function of the genetic algorithm used in this work is based on the comparison between the measured absorption coefficient $\alpha^{(\text{exp})}$ and the theoretical absorption coefficient $\alpha^{(\text{teo})}$ computed from the Johnson-Champoux-Allard (JCA) model Allard and Champoux [1992]; Johnson et al. [1987] using a rigid frame equivalent fluid approach. The objective function in this case is given by

$$\beta = \sum_{n=1}^{N} \left| \frac{\alpha_n^{(\text{exp})} - \alpha_n^{(\text{teo})}}{\alpha_n^{(\text{exp})}} \right|^2 \tag{2.21}$$

with n being the sample and N is the total number of samples in the measurement.

This technique was also applied by Pereira et al. [2019] for porous concrete mate-

rial characterization, where the concrete was modeled by using the Horoshenkov-Swift model Horoshenkov and Swift [2001].

The optimization code used in this work is based on the *ga* function in MATLAB/OCTAVE, that finds the minimum error to the objective function β in Eq. (2.21) based on genetic algorithms. Although direct measurement of each parameter is beneficial for a more robust characterization of the samples, the information of optimized parameters can be sufficient to represent the material in ordinary commercial codes of energy-based methods, like Statistical Energy Analysis (SEA) and Transfer Matrix Method (TMM).

2.2.7 Sound absorption analysis and the application of inverse methods

This section presents the optimized results and the comparison to experimental data. The experiments were done in Technical University of Malasya Malacca. This contribution resulted in a book chapter publication by *et al.* Putra et al. [2021].

A set of measurements for different thicknesses of the kenaf fibres are evaluated. It is important to consider that the rigid frame equivalent fluid model does not consider the frame properties, which means that different acoustic parameters should be given for each structural configuration. Otherwise, the acoustic parameters should be valid for all the geometrical setup, that is, different thickness setups.

The explained method was used to estimate the macroscopic parameters of the fiber, taking into account the measured absorption coefficient. The initial parameter entries are informed as well as the intervals that limit the range of optimization of these variables. To choose the initial parameters, typical values of the macroscopic properties for mineral fibers are considered Cox and D'Antonio [2009]. The input parameters used in this work are presented in Table 2.2.

Table 2.2: Algorithm input parameters.

	σ [kN/m^4]	ϕ [-]	α_∞ [-]	Λ [μm]	Λ' [μm]
Starting shot	20	0.75	1.02	100	150
Upper limit	50	0.80	1.06	180	400
Lower limit	10	0.65	1.00	60	100

In addition to the parameters reported in Table 2.2, it is evident that the sample

thickness and the sound absorption coefficient of the sample obtained experimentally are also necessary for the optimization of the analytical curve. The analysis was performed up to 5.5 kHz.

In this study, the samples were characterized taking into account the proposed model. Each simulation has an objective error value and a time limit for solution. Table 2.3 presents the mean obtained values from 5 runs of this optimization process, considering the kenaf samples.

Table 2.3: Numerical macroscopic parameters for the kenaf fiber.

	σ [kN/m^4]	ϕ [-]	α_∞ [-]	Λ [μm]	Λ' [μm]
Kenaf fiber 178 [kg/m^3]	25.543	0.701	1.1	84.5	102.3

The experimental results of kenaf are compared with the obtained numerical sound absorption coefficient in Figure 2.6.

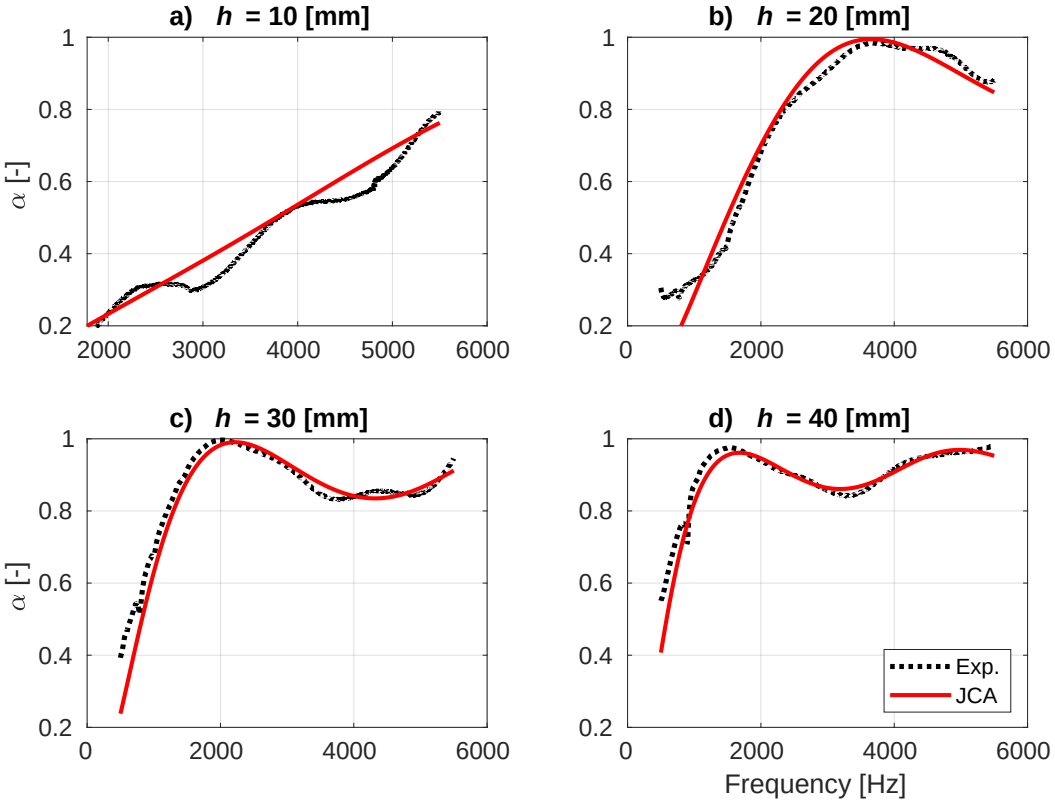

Figure 2.6: Comparison of optimized and experimental results for the kenaf fiber with different thicknesses (density 178 kg/m^3).

It can be seen in Figure 2.6 that the optimized parameters shown in Table 2.3 represent well the sound absorption coefficient of the fiber for the different values of thickness by using the JCA model. Notice that the lowest thickness of 10 mm in the experimental result in Figure 2.6(a) has some anti-resonances shown by the fluctuation of the absorption coefficient. It may be related to the frame vibration phenomena that cannot be modeled by rigid frame models, as well as the difficulty of experimental mounting conditions for very low thickness fibers in the impedance tube.

The normalized surface impedance $\tilde{Z}_s$ (as in Eq (2.3)) of the sample was also evaluated experimentally and numerically. Figure 2.7 shows the real and imaginary part of the normalized impedance measured for four different thicknesses. Figure 2.8 shows the obtained results from the inverse characterization. It can be noticed the same tendency of the impedance in most parts of the spectrum, although discrepancy between experimental (Figure 2.7) and theoretical (Figure 2.8) results are observed in the real part of the impedance at very low frequencies.

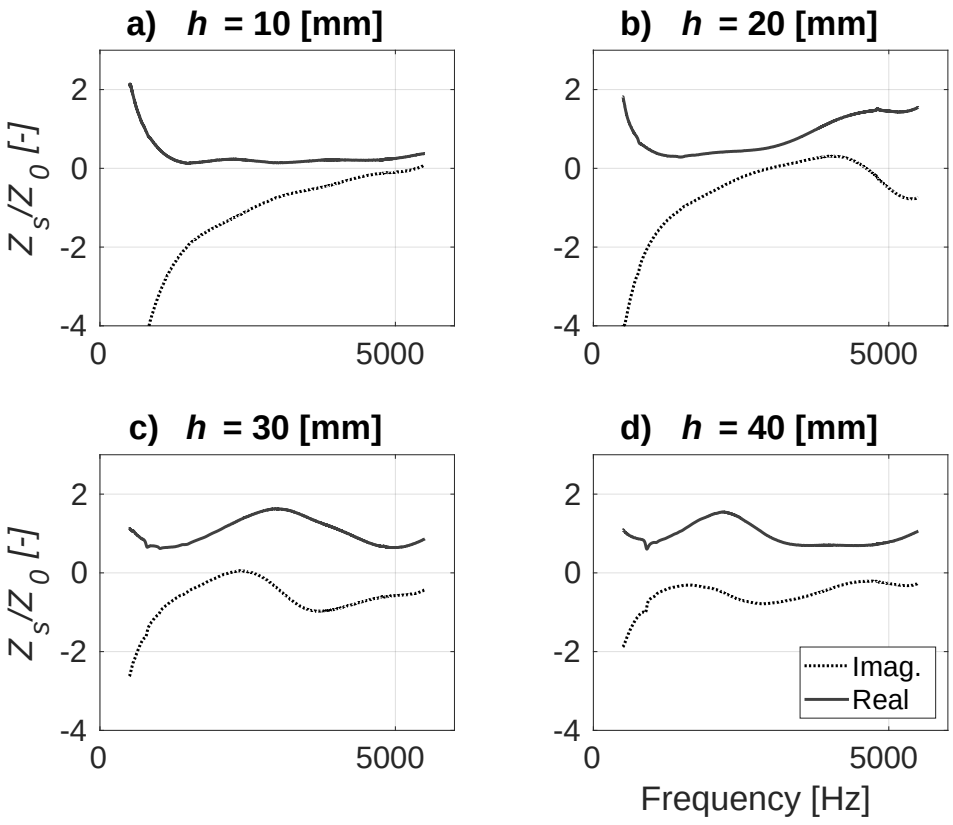

Figure 2.7: Experimental surface impedance normalized by $Z_0 = \rho_0 c_0$ for the kenaf fiber (density 178 kg/m^3).

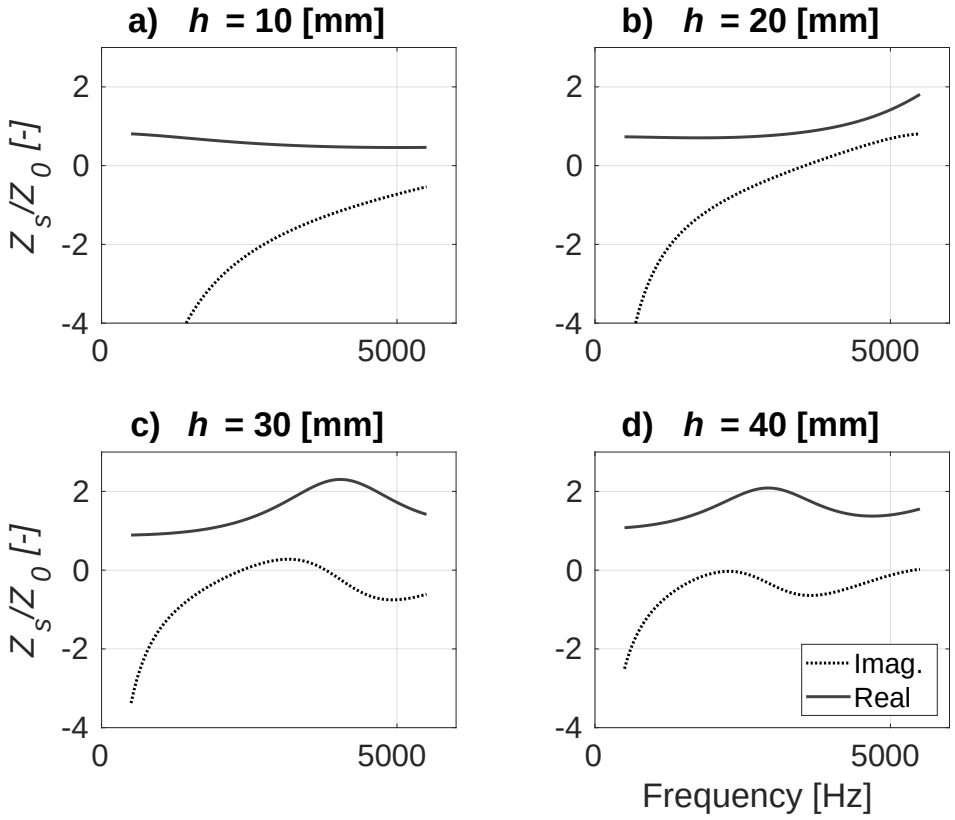

Figure 2.8: Numerical surface impedance normalized by $Z_0 = \rho_0 c_0$ for the kenaf fiber (density 178 kg/m^3).

It is important to clarify that this optimization process considers the porous materials as equivalent fluids. It means that the simulated acoustic properties should change for different solid frame properties, for example for different fiber density of the sample.

2.3 Transfer matrices

Multilayer panels are often used in the context of noise control. The mechanisms that involves the application of a noise control treatment (NCT) on a face of a structural system are: the sound insertion loss (IL), which can change the acoustic radiation and the mass law transmission of a structure, the sound absorption seen by the acoustic medium in contact with the surface and the added structural damping. The methodology of the Transfer Matrix Method (TMM) Allard and Atalla [2009] is based on

the theory of plane wave propagation in a given layer. The material of each layer is assumed homogeneous, isotropic and the surface of the treatment is considered infinite in this formulation. Figure 2.9 shows an incident plane acoustic wave upon a media with thickness h, at an incident angle θ.

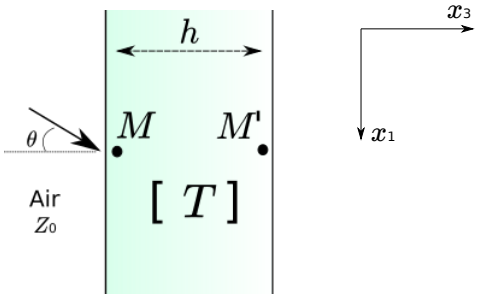

Figure 2.9: Ilustration of an infinite extent layer on the Tranfer Matrix Method.

By considering oblique incidence, the x_1 component of the propagating wavenumber, also denoted as trace wavenumber k_t, is given by

$$k_t = k_0 \sin(\theta) \tag{2.22}$$

Note that k_0 represents the wavenumber in the surrounding fluid. The sound propagation inside the layer is represented by a transfer matrix T

$$V(M) = [T]V(M') \, , \tag{2.23}$$

where V is a vector containig the response for each degree of freedom of the media at the points M and M' set close to the foward and the backward of the layer Allard and Atalla [2009]. Thomson 1950 suggested the transmission matrices representing the propagation of plane elastic waves through stratified mediums. In this study, solid and fluid domains were initially approached, but the final equations in this formulation were limited to some special cases. The boundary conditions based on continuity of stresses and velocities proposed by Thompson was also used by Folds and Loggins 1977, who derived the transfer matrices of paralel solid plates excited by oblique incidence plane waves.

The most important definition of this method is the transfer matrix of the layer media, which can be seen as a frequency response function of the linear system. In this section, the fluid, solid and poroelastic matrices are presented, as well as the continuity conditions between them. These parameters are used for assembling the global matrix

and allowing the resolution of the linear problem.

2.3.1 Fluid layer

A linear acoustic fluid domain can be characterized by two independent degrees of freedom: the pressure p and the particle velocity v_3^f in the longitudinal direction x at a point into the medium. In the notation exposed in Equation (2.23), the response vector at the point M will be given as

$$V^f(M) = [p(M)\ v_3^f(M)]^{\mathrm{T}}\ , \tag{2.24}$$

where the index 3 represents the longitudinal direction of propagation Allard and Atalla [2009] and T indicates the tranposed operation. The longitudinal propagating wavenumber into the fluid is given as

$$k_3 = \sqrt{k_{eq}^2 - k_t^2}; \tag{2.25}$$

where k_{eq} is the characteristic wavenumber of the medium, which can be complex if the layer is a porous material represented by an equivalent fluid (see Equation (2.13)).

The transfer matrix of a fluid is derivated from the solution of the 1D wave equation, by calculating the pressure and velocity field at the points M and M'. If considering $M' = 0$, the distance between 2 points wil be represented by the thickness h of the layer and the position of $M = -h$. In this context, the transfer matrix $[T^f]$ will be given as

$$[T^f] = \begin{bmatrix} \cos(k_3 h) & \mathrm{j}\,\frac{\omega\rho_0}{k_3}\sin(k_3 h) \\ \mathrm{j}\,\frac{k_3}{\omega\rho_0}\sin(k_3 h) & \cos(k_3 h) \end{bmatrix}\ , \tag{2.26}$$

For more details on the solution of the acoustic wave-equation, references Beranek [1954] and Kuttruff [2007] can be consulted.

2.3.2 Solid layer

According to Lauriks et al. [1992] four waves can propagate in a complete description of a solid media: two longitudinal and two shear waves (incident and reflected). For an isotropic solid, the propagating wavenumbers associated to each direction depends

on the Lamé coefficients, wich is given as

$$\begin{aligned} \lambda &= \frac{E(1+\mathrm{j}\,\eta)\,\nu}{(1+\nu)(1-2\nu)}\ ; \\ \mu &= \frac{E(1+\mathrm{j}\,\eta)}{2(1+\nu)}\ , \end{aligned} \tag{2.27}$$

being E the Young's modulus, ν the Poisson's ratio, η the dissipation loss factor, λ and μ the first and second Lamé coefficients of the plate, respectively. Both parameters are used for calculating the characteristic wavenumber in the longitudinal δ_1 and shear δ_2 directions

$$\begin{aligned} \delta_1 &= \sqrt{\frac{\omega^2\rho}{\lambda+2\mu}} \\ \delta_3 &= \sqrt{\frac{\omega^2\rho}{\mu}} \end{aligned} \tag{2.28}$$

where ρ is the density of the solid elastic material.

Folds and Loggins [1977] presented the velocities v_1, v_3 and stress components σ^s_{33} and σ^s_{13} in function of displacement potentials of the longitudinal and shear waves. The response vector of a structural layer at the point M becomes

$$V^s = [v^s_1(M)\ v^s_3(M)\ \sigma^s_{33}\ \sigma^s_{13}]^{\mathrm{T}} \tag{2.29}$$

In order to obtain the transfer matrix of the elastic solid, the vector V at the points M and M' should be connected with the four by four system that depends on the four amplitudes of the propagating waves cited before, wich can be expressed as

$$V^s(M) = [\Gamma(M)]W \tag{2.30}$$

$$V^s(M') = [\Gamma(M')]W \tag{2.31}$$

where W is the amplitude vector extracted from the potential relations and Γ is a position dependent matrix given as

$$[\Gamma(x_3)] = \begin{bmatrix} \omega k_t \cos(k_{13}x_3) & -\mathrm{j}\,\omega k_t \sin(k_{13}x_3) & \mathrm{j}\,\omega k_{33} \sin(k_{33}x_3) & -\omega k_{33} \cos(k_{33}x_3) \\ -\mathrm{j}\,\omega k_{13} \sin(k_{13}x_3) & \omega k_{13} \cos(k_{13}x_3) & \omega k_t \cos(k_{33}x_3) & -\mathrm{j}\,\omega k_t \sin(k_{33}x_3) \\ -D_1 \cos(k_{13}x_3) & \mathrm{j}\,D_1 \sin(k_{13}x_3) & \mathrm{j}\,D_2 k_{33} \sin(k_{33}x_3) & -D_2 k_{33} \cos(k_{33}x_3) \\ \mathrm{j}\,D_2 k_{13} \sin(k_{13}x_3) & -D_2 k_{13} \cos(k_{13}x_3) & D_1 \cos(k_{33}x_3) & -\mathrm{j}\,D_1 \sin(k_{33}x_3) \end{bmatrix}, \tag{2.32}$$

where $k_{13} = \sqrt{\delta_1^2 - k_t^2}$ is the shear propagating wavenumber, $k_{33} = \sqrt{\delta_3^2 - k_t^2}$ is the normal wavenumber on the x_3 direction, $D_1 = \lambda(k_t^2 + k_{13}^2) + 2\mu k_{13}^2$ and $D_2 = 2\mu k_t$ are elastic coefficients Allard and Atalla [2009].

By considering the origin point $M' = 0$ and $M = -h$ (see Figure 2.9), the transfer matrix of an elastic solid can be calculated from the ratio between Equations (2.30) and (2.31), which is

$$V^s(-h) = [T^s]V^s(0) = [\Gamma(-h)][\Gamma(0)]^{-1}V^s(0) \tag{2.33}$$

$$T^s = [\Gamma(-h)][\Gamma(0)]^{-1}\,, \tag{2.34}$$

where $[T^s]$ is the transfer matrix of the elastic solid layer. This approach fixes the inversion of Γ at the point zero, which allows to obtain an inverse matrix independent of the thickness h

$$[\Gamma(0)]^{-1} = \begin{bmatrix} \frac{D_2}{\omega(D_1+D_2k_t)} & 0 & \frac{-1}{D_1+D_2k_t} & 0 \\ 0 & \frac{D_1}{k_{13}(D_1+D_2k_t)} & 0 & \frac{-k_t}{k_{13}(D_1+D_2k_t)} \\ 0 & \frac{D_2}{\omega(D_1+D_2k_t)} & 0 & \frac{1}{D_1+D_2k_t} \\ \frac{-D_1}{\omega(D_1k_{33}+D_2k_tk_{33})} & 0 & \frac{-k_t}{D_1k_{33}+D_2k_tk_{33}} & 0 \end{bmatrix}, \tag{2.35}$$

Eq. (2.35) was solved by a symbolic calculation of an original code of this work and differs from Allard and Atalla [2009], being an alternative form of obtaining the inverse matrix $[\Gamma(0)]^{-1}$. The derivation of $\Gamma(x3)$ from the potential displacements are detailed in references Allard and Atalla [2009] and Folds and Loggins [1977].

2.3.3 Septum and thin plate layers

Some modifications of the elastic solid can be useful for more simple modelling strategies. An interesting alternative is to model the plate as a thin elastic solid in bending. It means that the thickness of the layer is sufficiently small and normal waves are much more important then shear waves.

Even simpler, a septum layer is a limp thin layer. It means that the layer is assumed to have no stiffness and can be fully described by the mass per unit area of the material. The for of the equation of motion of this kind of media is given by

$$Z_s(\omega)v_3(M') = \sigma_{33}(M') - \sigma_{33}(M) \tag{2.36}$$

where $Z_s(\omega)$ is the mechanical impedance of the panel, with

$$\begin{aligned} Z_s &= \mathrm{j}\,\omega m'' , \quad \text{for a septum} \\ Z_s &= \mathrm{j}\,\omega m'' \left(1 - \frac{Dk_t^4}{\omega^2 m''}\right), \quad \text{for a thin plate} \end{aligned} \tag{2.37}$$

with D being the bending stiffness and m'' the mass per unit area of the plate. The 2-degrees of freedom response vector of the mecanical field in a point M is $V^t(M) = [\sigma_{33}(M)v_3(M)]^{\mathrm{T}}$, and the tranfer matrix for this media is given by

$$[T^t] = \begin{bmatrix} 1 & -Z_s \\ 0 & 1 \end{bmatrix} . \tag{2.38}$$

If the septum is considered massless, the mechanical impedance becomes zero and the transfer matrix reduces to identity. This case can simulate a thin impervious screen used to protect a porous material in pratical meanings.

2.3.4 Poroelastic layer

According to the Biot's theory of propagation of elastic waves in a fluid saturated porous solid Biot [1956], two compressional waves and shear wave can propagate in a porous material. These wave equations were used by *et al.* Lauriks et al. [1992] to evaluate the tranfer matrix of a poroelastic material containing 6 degrees of freedom, with reponse vector given by

$$V^P(M) = [v_1^s \; v_3^s(M) \; v_3^f(M) \; \sigma_{33}^s(M) \; \sigma_{13}^s(M) \; \sigma_{33}^f(M)]^{\mathrm{T}} \tag{2.39}$$

where v_1^s and v_3^s are the x_1 and x_3 components of the solid frame velocity, v_3^f is the fluid particle velocity component, σ_{13}^s and $\sigma_3 3^s$ are the shear and normal components of the solid stress tensor and σ_{33}^f the longitudinal component in the fluid stress.

For the problem ilustrated in Figure 2.9, the x_3 component of the propagating wavenumber is given by

$$k_{i3} = \sqrt{(\delta_i^2 - k_1^2)} \quad i = [1, 2, 3] \tag{2.40}$$

with δ_i being the wavenumbers for each wavetype i.

Similary to the solid layer procedure, the transfer matrix of a poroelastic media is evaluated from the auxiliar matrix $\Gamma(x_3)$ which relates the degrees of freedom at a point with the incident and reflected amplitudes of the wave potential realations Allard and Atalla [2009]. Analogous to Equation (2.35), the TM of a poroelastic material is computed by

$$[T^P] = [\Gamma(-h)][\Gamma(0)]^{-1} \,, \tag{2.41}$$

The six columns of $\Gamma(x)$ are given in Table 2.4, where D_i and E_i are elastic functions that depends on the elasticity coefficients Biot parameters, presented with details in references Lauriks et al. [1992] and Allard and Atalla [2009].

Table 2.4: Auxiliar matrix $\Gamma(x)$ for a poroelastic material Allard and Atalla [2009].

The three first columns

$$\begin{bmatrix} \omega k_t \cos(k_{13}x_3) \\ -\mathrm{j}\,\omega k_{13} \sin(k_{13}x_3) \\ -\mathrm{j}\,\omega k_{13}\mu_1 \sin(k_{13}x_3) \\ -D_1 \cos(k_{13}x_3) \\ \mathrm{j}\,2Nk_tk_{13} \sin(k_{13}x_3) \\ -E_1 \cos(k_{13}x_3) \end{bmatrix} \quad \begin{bmatrix} -\mathrm{j}\,\omega k_t \sin(k_{13}x_3) \\ \omega k_{13} \cos(k_{13}x_3) \\ \omega k_{13}\mu_1 \cos(k_{13}x_3) \\ \mathrm{j}\,D_1 \sin(k_{13}x_3) \\ -2Nk_tk_{13} \cos(k_{13}x_3) \\ \mathrm{j}\,E_1 \sin(k_{13}x_3) \end{bmatrix} \quad \begin{bmatrix} \omega k_t \cos(k_{23}x_3) \\ -\mathrm{j}\,\omega k_{23} \sin(k_{23}x_3) \\ -\mathrm{j}\,\omega k_{23}\mu_2 \sin(k_{23}x_3) \\ -D_2 \cos(k_{23}x_3) \\ \mathrm{j}\,2Nk_tk_{23} \sin(k_{23}x_3) \\ -E_2 \cos(k_{23}x_3) \end{bmatrix}$$

The three last columns

$$\begin{bmatrix} -\mathrm{j}\,\omega k_t \sin(k_{23}x_3) \\ \omega k_{23} \cos(k_{23}x_3) \\ \omega k_{23}\mu_2 \cos(k_{23}x_3) \\ \mathrm{j}\,D_2 \sin(k_{23}x_3) \\ -2Nk_tk_{23} \cos(k_{23}x_3) \\ \mathrm{j}\,E_2 \sin(k_{23}x_3) \end{bmatrix} \quad \begin{bmatrix} \mathrm{j}\,\omega k_{33} \sin(k_{33}x_3) \\ \omega k_t \cos(k_{33}x_3) \\ \omega k_t\mu_3 \cos(k_{33}x_3) \\ 2\,\mathrm{j}\,Nk_tk_{33} \sin(k_{33}x_3) \\ N(k_{33}^2 - k_t^2) \cos(k_{33}x_3) \\ 0 \end{bmatrix} \quad \begin{bmatrix} -\omega k_{33} \cos(k_{33}x_3) \\ -\mathrm{j}\,\omega k_t \sin(k_{33}x_3) \\ -\mathrm{j}\,\omega k_t\mu_3 \sin(k_{33}x_3) \\ -2Nk_{33}k_t \cos(k_{33}x_3) \\ -\mathrm{j}\,N(k_{33}^2 - k_t^2) \sin(k_{33}x_3) \\ 0 \end{bmatrix}$$

Figure 2.10 shows simulated results of the normal incidence absorption coefficient of a melamine foam if considering equivalent fluid or poroelastic formulations for a baseline sample whose properties are presented in Table 2.5. The reference thickness is 2 in.

Table 2.5: Properties of a baseline melamine foam.

	σ [kN/m^4]	ϕ [-]	α_∞ [-]	Λ [μm]	Λ' [μm]	η [-]	E [kPa]	ν [-]
Melamine foam 8.85 [kg/m^3]	12569	0.99	1.02	78	192	0.063	93.348	0.44

The main difference between the plots in Figure 2.10 occurs at the anti-resonance around 500 Hz caused by the compression waves of the solid frame that are considered in the poroelastic modeling approach. This gap can be reduced as the structural damping loss factor increases. Young's modulus and Poisson's ratio of the solid frame control the tuning frequency of this gap. Figure 2.11 shows a sensitivity analysis in the sound absorption coefficient of the same baseline sample considering variations of structural properties.

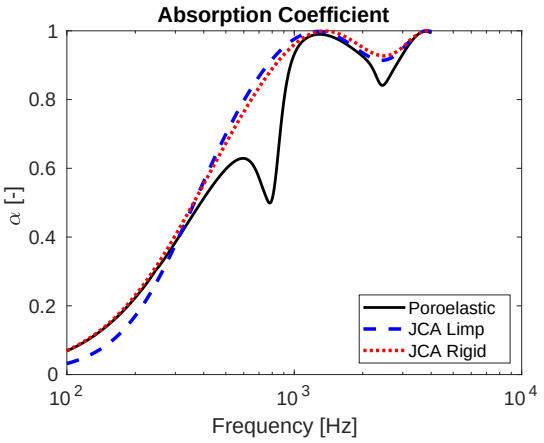

Figure 2.10: Equivalent fluid *vs* poroelastic model absorption coefficient.

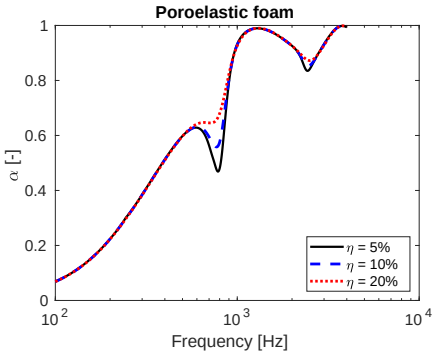

(a) η varying.

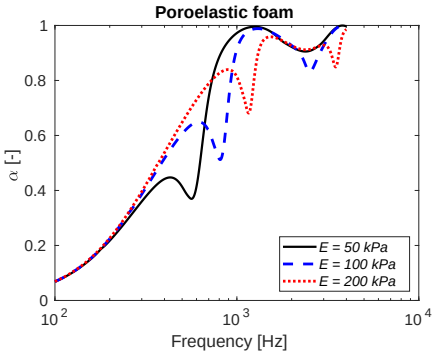

(b) E varying.

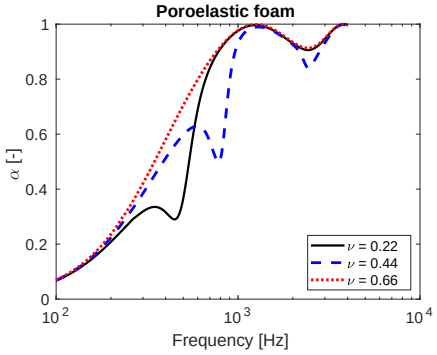

(c) ν varying.

Figure 2.11: Sound absorption coefficient of a poroelastic material considering structural changes.

2.4 Numerical procedure of the TMM

When a multilayered treatment is modeled, the transfer matrices presented in Section 2.3, as well as the continuity conditions between each layer, should be considered.

In this method, these conditions are given in terms of coupling matrices that simplify the assembling process of a global transfer matrix. Figure 2.12 illustrates a multilayer NCT with n layers and $2n$ interface surfaces.

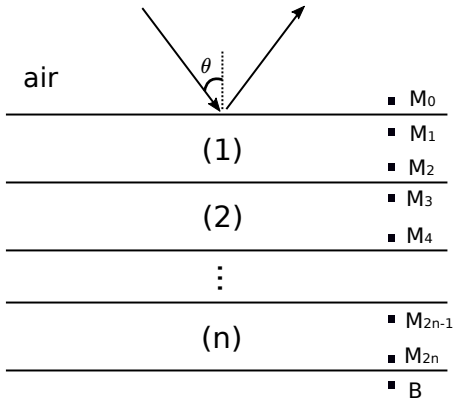

Figure 2.12: Ilustration of a multilayer NCT with n layers and $2n$ continuity interfaces.

If considering the connection between layer (1) and (2), the folowing relation is established

$$V^{(1)}(M_2) = V^{(2)}(M_3) = [T]^{(2)}V^{(2)}(M_4) \tag{2.42}$$

with $[T]^{(2)}$ being the transfer matrix of the layer 2. At the continuity surfaces, the relationship between degrees of freedom of each layer should be explained. This relashionship is given by interface matrices $[I]$ and $[J]$ that imposes the conditions in wich Equation (2.42) can be valid. Taking into account these parameters, Equation (2.42) can be rewrited as

$$[I_{(1)(2)}]V^{(1)}(M_2) + [J_{(1)(2)}][T^{(2)}]V^{(2)}(M_4) = 0 \tag{2.43}$$

Where $[I_{(1)(2)}]$ and $[J_{(1)(2)}]$ are the interface matrices between layer (1) and (2).

2.4.1 Assembling of the global transfer matrix

The process of assembling the global transfer matrix is similar to a finite element process. As the interface matrices are not square, a simple vectorial product cannot be used to make it. If considering Figure 2.12, the generalization of Equation 2.43 is given as follows

$$I_{(n)(n+1)}V^{n}(M_{2(n)}) + J_{(n)(n+1)}T^{(n+1)}V^{(n+1)}(M)_{2(n+1)} = 0\ . \tag{2.44}$$

The incident media (air) is assumed as layer zero (0) in this generalization. By following Equation (2.44), using the local transfer matrices and the interface matrices presented in this section, the global matrix GM_0 is assembled as follows

$$[TG_0] = \begin{bmatrix} [I_{(01)}] & [J_{(01)}][T^{(1)}] & [0] & \dots & [0] & [0] \\ [0] & [I_{(12)}] & [J_{(12)}][T^{(2)}] & \dots & [0] & [0] \\ \vdots & \vdots & \vdots & \ddots & \vdots & \vdots \\ [0] & [0] & [0] & \dots & [I_{(n-1)(n)}] & [J_{(n-1)(n)}][T^{(n)}] \end{bmatrix} \tag{2.45}$$

and the rigth-hand side

$$V_0 = [V^{(0)}(A)\ V^{(1)}(M_2)\ V^{(2)}(M_4)\ \dots\ V^{(n)}(M_{2n})]^{\mathrm{T}}\,. \tag{2.46}$$

The global transfer matrix TG_0 is not square and do not have same number of lines as V_0, but it follows the dimension of the continuity matrices presented in the following section. If N is the number of degrees of freedom of the problem, TG_0 in this step has $N-4$ lines if the last layer is a porous, $N-3$ if it is a solid and $N-2$ if the last media is a fluid. It means that extra equations are necessary to complete the linear problem. These equations are given by the boundary and initial conditions.

2.4.1.1 Continuity between layers

A compilation of the continuity matrices for different connection types are presented in Table 2.6. The most important matrices were extracted from reference Allard and Atalla [2009]. It is used the index f for fluid, s for solid and p for porous. With layers of different nature, the matrices should be permuted if the reverse order is required, it means

$$[I_{ij}] = [J_{ji}] \qquad i,j = [f\,s\,p]\,. \tag{2.47}$$

Table 2.6: Continuity matrices.

$I_{ff} = \begin{bmatrix} 1 & 0 \\ 0 & 1 \end{bmatrix}$	$J_{ff} = -\begin{bmatrix} 1 & 0 \\ 0 & 1 \end{bmatrix}$
$I_{ss} = \begin{bmatrix} 1 & 0 & 0 & 0 \\ 0 & 1 & 0 & 0 \\ 0 & 0 & 1 & 0 \\ 0 & 0 & 0 & 1 \end{bmatrix}$	$J_{ss} = -\begin{bmatrix} 1 & 0 & 0 & 0 \\ 0 & 1 & 0 & 0 \\ 0 & 0 & 1 & 0 \\ 0 & 0 & 0 & 1 \end{bmatrix}$
$[I_{pp}] = \begin{bmatrix} 1 & 0 & 0 & 0 & 0 & 0 \\ 0 & 1 & 0 & 0 & 0 & 0 \\ 0 & 1-\frac{\phi_2}{\phi_1} & \frac{\phi_2}{\phi_1} & 0 & 0 & 0 \\ 0 & 0 & 0 & 1 & 0 & 1-\frac{\phi_2}{\phi_1} \\ 0 & 0 & 0 & 0 & 1 & 0 \\ 0 & 0 & 0 & 0 & 0 & \frac{\phi_2}{\phi_1} \end{bmatrix}$	$[J_{pp}] = -\begin{bmatrix} 1 & 0 & 0 & 0 & 0 & 0 \\ 0 & 1 & 0 & 0 & 0 & 0 \\ 0 & 0 & 1 & 0 & 0 & 0 \\ 0 & 0 & 0 & 1 & 0 & 0 \\ 0 & 0 & 0 & 0 & 1 & 0 \\ 0 & 0 & 0 & 0 & 0 & 1 \end{bmatrix}$
$I_{sf} = \begin{bmatrix} 0 & 1 & 0 & 0 \\ 0 & 0 & 1 & 0 \\ 0 & 0 & 0 & 1 \end{bmatrix}$	$J_{sf} = \begin{bmatrix} 0 & -1 \\ 1 & 0 \\ 0 & 0 \end{bmatrix}$
$I_{pf} = \begin{bmatrix} 0 & (1-\phi) & \phi & 0 & 0 & 0 \\ 0 & 0 & 0 & 1 & 0 & 0 \\ 0 & 0 & 0 & 0 & 1 & 0 \\ 0 & 0 & 0 & 0 & 0 & 1 \end{bmatrix}$	$J_{pf} = \begin{bmatrix} 0 & -1 \\ (1-\phi) & 0 \\ 0 & 0 \\ \phi & 0 \end{bmatrix}$
$I_{sp} = \begin{bmatrix} 1 & 0 & 0 & 0 \\ 0 & 1 & 0 & 0 \\ 0 & 1 & 0 & 0 \\ 0 & 0 & 1 & 0 \\ 0 & 0 & 0 & 1 \end{bmatrix}$	$J_{sp} = -\begin{bmatrix} 1 & 0 & 0 & 0 & 0 & 0 \\ 0 & 1 & 0 & 0 & 0 & 0 \\ 0 & 0 & 1 & 0 & 0 & 0 \\ 0 & 0 & 0 & 1 & 0 & 1 \\ 0 & 0 & 0 & 0 & 1 & 0 \end{bmatrix}$

Septum and thin plate layers can be considered as equivalent fluids with similar

continuity conditions of a fluid layer, but the acoustic pressure is equivalent to the negative value of normal stresses $p(M) = -\sigma_{33}(M')$, wich demand a sign changing in the column of $[I]$ and $[J]$ relative to the normal stresses.

It is also possible to do a simple multiplication of matrices in same type layers connection, which means that a single block with equivalent properties will be considered for a group of layers of same nature connectd simultaniously. However, in case of porous-porous junction, the difference of porosities should be taken into account. The $[I]$ matrices are used to consider this condition and the equivalent matrix is given by

$$[T_{eq}^{(n)}] = [T^{(n-1)}][I_{(n-1)(n)}][T^{(n)}] \; . \tag{2.48}$$

Equation (2.48) is valid only for layers of same nature.

2.4.2 Applying the boundary conditions

A noise control treatment in SEA analysis can change three main parameters: the damping of a cavity from the surface absorption of the NCT, the radiation impedance of a plate in contact with the air and the damping of a structural system. Different boundary conditions are appropriated for computing each parameter, based on typical SEA simulation approaches Atalla and Sgard [2015].

2.4.2.1 Rigid wall or pressure release terminations

If the multilayer is backed by a rigid wall, the velocities at the last interface are equal to zero, which characterize the infinite impedance condition at the boundary. The number of equations will depend on the number of velocity degrees of freedom of the last layer. For poroelastic materials, 3 conditions are necessary. If the las layer is a solid, 2 equations should be added. Finally, one equation for the normal velocity is requested if the last layer is a fluid.

These conditions can be rearranged for being presented in a matrix form. In this context, a boundary matrix $[Y^{(n)}]$ can be found as

$$[Y^{(n)}]V^{(n)}(M_{2n}) = 0 \; . \tag{2.49}$$

Equation (2.49) needs to indicate that the velocity components in the vector $V^{(n)}$ are zero. The non-zero term of the matrix $[Y^{(n)}]$ should be given in according to the position

of that components at the degrees of freedom vector. Table 2.7 shows a compilation of the boundary matrix for three cases of termination, where the index p, s and f represents poroelastic, solid and fluid terminations, respectively.

Table 2.7: Rigid wall boundary arrays

$[Y^p]$	$[Y^s]$	$[Y^f]$
$\begin{bmatrix} 1 & 0 & 0 & 0 & 0 & 0 \\ 0 & 1 & 0 & 0 & 0 & 0 \\ 0 & 0 & 1 & 0 & 0 & 0 \end{bmatrix}$	$\begin{bmatrix} 1 & 0 & 0 & 0 \\ 0 & 1 & 0 & 0 \end{bmatrix}$	$\begin{bmatrix} 1 & 0 \end{bmatrix}$

A similar approach is used for the pressure release condition, which means that the pressure/stress components are equal to zero at the termination, characterizing the state of infinite admitance at the boundary. Table 2.8 shows the boundary matrices if considering this case.

Table 2.8: Pressure release boundary arrays

$[Y^p]$	$[Y^s]$	$[Y^f]$
$\begin{bmatrix} 0 & 0 & 0 & 1 & 0 & 0 \\ 0 & 0 & 0 & 0 & 1 & 0 \\ 0 & 0 & 0 & 0 & 0 & 1 \end{bmatrix}$	$\begin{bmatrix} 0 & 0 & 1 & 0 \\ 0 & 0 & 0 & 1 \end{bmatrix}$	$\begin{bmatrix} 0 & 1 \end{bmatrix}$

These matrices will compose the last lines of the global matrix $[TG]$, at the termination columns (related to the last degrees of freedom of the vector $V^{(n)}$), wich is

$$[TG] = \begin{bmatrix} [\dots & \dots & TG_0 & \dots & \dots] \\ [0] & \dots & [0] & \dots & [Y^{(n)}] \end{bmatrix} . \tag{2.50}$$

The terms non related with the last layer are completed with zeros in the global transfer matrix. The global response vector in this case is composed by the original degrees of freedom of the problem $V_G = V_0$ (Equation 2.46).

2.4.2.2 Semi-infinite fluid termination

For semi-infinite fluid termination, an extra air layer with a characteristic impedance $Z_0 \cos(\theta)$ is added at the end of the global matrix and two more degrees of freedom $V(B) = [p(B)\, v(B)]^{\mathrm{T}}$ will be added to the response vector V_0. Firstly, the continuity equations will be applied as an extension of the Equation (2.44) for the connection between the last layer and the semi-infinite fluid, then

$$[I_{(n)f}]V^{(n)}(M_{2n}) + [J_{(n)f}]V^{f}(B) = 0 . \tag{2.51}$$

Where n can be p, s or f according to the nature of the last layer. When the continuity is done, the impedance condition is applied in the fluid B by means of a boundary vector $[Y^{(sif)}]$ given by

$$[Y^{(sif)}] = [-1 \;\; Z_B \cos\theta] , \tag{2.52}$$

As expected, this vector has the same size as the $[Y^{f}]$ presented in the Table 2.7. The proper application of the characteristic impedance can be evaluated by checking the relation

$$[Y^{(sif)}]V^{f}(B) = 0 . \tag{2.53}$$

In terms of global matrix, the continuity matrices and the boundary vector is applied as follows

$$[T_G] = \begin{bmatrix} \dots & & & [0] \\ & D_0 & & [0] \\ \dots & & & [0] \\ \dots & & I_{(n)f} & J_{(n)f} \\ \dots & & [0] & [Y^{(sif)}] \end{bmatrix} \tag{2.54}$$

with the new global response vector being $V_G = [V_0 \;\; V_B]^{\mathrm{T}}$.

2.4.3 Direct solution: intial condition

If executing all the steps presented in the previous sections, one line will be missing for the global transfer matrix to become square. It is possible to extract the acoustical parameters from determinants of the global matrix, but this approach is computationally inefficient and it will not be presented in this section. A more efficient way includes an input excitation (velocity or pressure), which allows calculating a direct solution of a global linear system.

If fixing an arbitrary value for the initial velocity and eliminating the second column of T_G and second line of V_G, a constant velocity piston excitation is considered. This excitation should be informed in the right-hand side of the system of equations, which means that the eliminated column becomes an excitation vector P, that is

$$[T_G]^F V_G^F = -v_0 P \ , \tag{2.55}$$

where $[T_G]^F$ and V_G^F are the global matrix and response vector after eliminating the excitation degree of freedom, respectively, and v_0 is the amplitude of the input velocity. In Equation (2.55), $[T_G]^F$ becomes square and a simple linear system can be solved for each frequency and incident angle, by using traditional numerical methods,

2.4.4 TMM indicators

Two acoustic indicators are important for the application studied in this chapter: the acoustic surface impedance Z_s of the multilayer and the transmission factor T. The acoustic impedance for a given frequency and incident angle is given by

$$Z_s(\omega, \phi) = \frac{V^F(1)}{v_0} \ , \tag{2.56}$$

where $V^F(1)$ is the first degree of freedom in the global response vector, which is the acoustic pressure at the surface in contact with the incident medium. The transmission factor is related to the sound insulation capacity of the treatment, that is

$$T(\omega, \theta) = (1 + R)\frac{V_1(n-1)}{V_1(1)} \ , \tag{2.57}$$

where $R = (Z_s \cos(\theta) - Z_0)/(Z_s \cos(\theta) + Z_0)$ is the reflection coefficient of the NCT. As it is a transmission problem, Equation (2.57) assumes that there is an acoustic medium

in the reception side, it means that a semi-infinite fluid is considered as the termination condition. For absorption problems, a rigid wall termination is more representative for practical experiments.

2.5 Finite-size Transfer Matrix Method

The class of porous materials is widely used for performance with respect to the sound quality of environments and noise control, given its ability to absorb sound energy. The dissipation of energy within a porous material occurs in a viscous, thermal, and structural character. Viscous dissipation is associated with shearing fluid close to the solid surface. The thermal mechanism comes from the creation of layers with different temperatures related to the heat flow between the fluid and the solid. The structural dissipation comes from the irreversible losses associated to the flexural movement of the fibers composing the structure Fahy [2000].

Numerical ways for calculating the properties of a noise control treatment subjected to an acoustic diffuse-field are available in the literature, but many of them cannot approximate the measured data in the reverberant room ia a realistic way, according to ISO 354 2003. The most common technique considers the integration of plane waves with different incidence angles impinging over the surface of an infinite sample. In this context, the Transfer Matrix Method (TMM) Allard and Atalla [2009] is generally used for considering multilayer structures under diffuse excitation. However, the assumption of lateral infinite extent of the samples is not capable to capture the diffraction effects on the edges, that proved to have important contributions to the response, mainly at low frequencies, when considering experimental conditions.

The finite-size correction is based on the spatial windowing of an infinite size sample. This technique was firstly proposed by Villot et al. [2001], that applied an approach for correcting the sound transmission loss of a multilayered system by applying the radiation impedance of a rectangular sample in the wavenumber domain, based on its surface geometry. Ghinet and Atalla [2001] proposed a mathematical variation to adapt the equations in a numerical form. Rhazi and Atalla [2010] proposed an analytical simplification of the radiation impedance in order to improve the computational efficiency. An approach similar to the one proposed in Ghinet and Atalla [2001] was presented by Brunskog [2012] for calculating the radiation impedance of single leaf walls, based on Li and Gibeling [2000] studies. A more detailed study about the numerical efficiency of these methods is not available in the literature.

Bonfiglio et al. [2016] proposed a reduce-order integral formulation to account finite size effects for same lateral dimension panels and expanded it for rectangular plates. The numerical results was compared with experimental data and has presented good performance in terms of computational cost for non greatly different lateral dimensions of the samples.

This section treats of a numerical investigation on the finite-size transfer matrix method problem. Implementation aspects are proposed in order to compare the computational efficiency of the solution. The influence of the surface mesh and integration points are explored and the results are presented against experimental data.

2.5.1 Radiation impedance and size effects

The case exposed in Figure 2.1 assumes that the sample dimensions are infinite in the lateral directions. Therefore, this prediction tends to underestimate the acoustic parameters if compared to experimental results for finite size samples, due to the radiation phenomena. It is possible to consider the influence of a radiation impedance Zr of a finite size sample by considering a rectangular geometry and taking into account the width (a) and length (b) of a simple panel. In order to demonstrate it, a surface of a single equivalent fluid layer is illustrated in Figure 2.13.

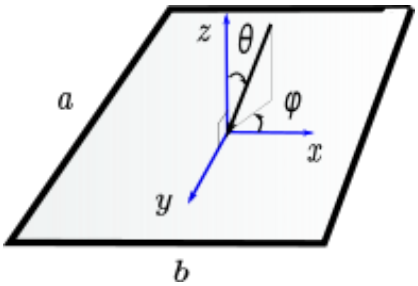

Figure 2.13: 3D sound wave impinging at the surface of a porous sample.

It can be noticed that the angle ϕ represents the azimuth angle of the incident plane wave, varying from 0 to 2π. The normalized radiation impedance for a baffled rectangular plate, as the example shown in Figure 2.13, can be represented as a quadruple integral over the plate surface in the near field formulation. In therms of the geometrical and physical parameters, this equation is well presented by Brunskog [2012] as

$$Z_R = \frac{\tilde{Z}_{\text{rad}}(\theta,\phi)}{Z_0} = \frac{\mathrm{j}\,k_0}{2\pi ab}\int_0^a\int_0^b\int_0^a\int_0^b \mathrm{e}^{\mathrm{j}\,k_0(\mu_x(x-x')+\mu_y(y-y'))}\,\frac{\mathrm{e}^{-\mathrm{j}\,k_0 R}}{R}\,\mathrm{d}\,x'\,\mathrm{d}\,y'\,\mathrm{d}\,x\,\mathrm{d}\,y \tag{2.58}$$

where $R = \sqrt{(x-x')^2+(y-y')^2}$ is the distance between two points, $\mu_x = \sin(\theta_i)\cos(\phi)$ and $\mu_y = \sin(\theta_i)\sin(\phi)$ are oscillating functions and $Z_{rad}(\theta,\phi)$ is the non-normalized radiation impedance. As the quadruple integral is not well suited for obtaining a numerical solution, a new coordinate system can be introduced Brunskog [2012]; Li and Gibeling [2000], where $\kappa = x - x'$, $\tau = y - y'$, $\zeta = x + x'$ and $\gamma = y + y'$. In this case, taking into account that $\int_\kappa^{2a-\kappa}\mathrm{d}\,\zeta = 2(a-\kappa)$, the double integral in the x and x' coordinates is given by

$$\int_0^a\int_0^a \mathrm{e}^{\mathrm{j}\,k_0(\mu_x(x-x')+\mu_y(y-y'))}\,\frac{\mathrm{e}^{-\mathrm{j}\,k_0 R}}{R}\,\mathrm{d}\,x\,\mathrm{d}\,x` = \int_0^a (\mathrm{e}^{-\mathrm{j}\,k_0(\mu_x\kappa+\mu_y\tau)} + \mathrm{e}^{-\mathrm{j}\,k_0(-\mu_x\kappa+\mu_y\tau)}) \times \frac{\mathrm{e}^{-\mathrm{j}\,k\sqrt{\kappa^2+\tau^2}}}{\sqrt{\kappa^2+\tau^2}}(a-\kappa)\,\mathrm{d}\,\kappa \tag{2.59}$$

Same procedure exposed in Equation (2.59) is considered for y and y' coordinates Li and Gibeling [2000] and the radiation impedance can be found, giving in total

$$Z_R(\theta,\phi) = \frac{\mathrm{j}k_0}{2\pi ab}\int_0^a\int_0^b 4\cos(k_0\mu_x\kappa)\cos(k_0\mu_y\tau)\frac{\exp(-jk_0\sqrt{\kappa^2+\tau^2})}{\sqrt{\kappa^2+\tau^2}}(a-\kappa)(b-\tau)\mathrm{d}\kappa\mathrm{d}\tau \tag{2.60}$$

Equation (2.60) can be evaluated numerically by applying a variable changing and using 2D Gauss' integration.

2.5.2 Numerical procedure

A remarkable contribution of this work presented a new Finite-Size Transfer Matrix Method (FTMM) numerical function on the computation of the sound absorption coefficient and transmission loss for finite size samples under diffuse field conditions, **including analysis for multi-layer systems**. The implemented FTMM consists in a 4-integral based code, being 2 in the surface coordinates and 2 concerning the plane wave angles. An ilustration of the numerical discretization is shown in Figure 2.14.

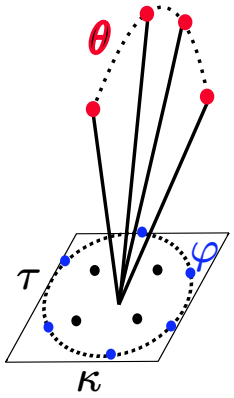

Figure 2.14: Numerical discretization of a single element. Red circles represent the integration points in theta, blue ones for the phi domain and black points for the $\kappa\tau$ space.

A function calculates the double integral of Z_R presented in Equation (2.61) for each Gauss point on the azimuth ϕ space. A rectangular grid is projected over the surface and the integration function $f(\kappa, \tau)$ in Equation (2.60) can be numerically evaluated using the relationship

$$Z_R(\theta,\phi) = \int_0^a \int_0^b f(\kappa,\tau)\mathrm{d}\kappa\mathrm{d}\tau = \int_{-1}^1 \int_{-1}^1 f(\kappa',\tau')\mathrm{d}\kappa'\mathrm{d}\tau' = \sum_{nx}\sum_{ny} C_{nx}C_{ny}f(\kappa',\tau')J_f \tag{2.61}$$

$$\kappa' = x_n + \frac{dx}{2}x_g(nx) + \frac{dx}{2}\,, \quad \tau' = y_n + \frac{dy}{2}x_g(ny) + \frac{dy}{2}\,. \tag{2.62}$$

where xn and yn are the coordinates of the first node into the element, x_g is the gauss point coordinate, κ' and τ' are the new space variables, dx and dy are element lengths, $J_f = dxdy/4$ is the Jacobian for the new integration limits, C_x and C_y are the weight functions at the Gauss points nx and ny distributed over the elements on the grid.

2.5.3 Sound absorption of finite-size systems

In this section, experimental results are compared to numerical results obtained from the *SEA Module*. The diffuse sound absorption coefficient was obtained experimentally by following the guidelines of the standard ISO 354 ISO:354 [2003], as illustrates Figure 2.15.

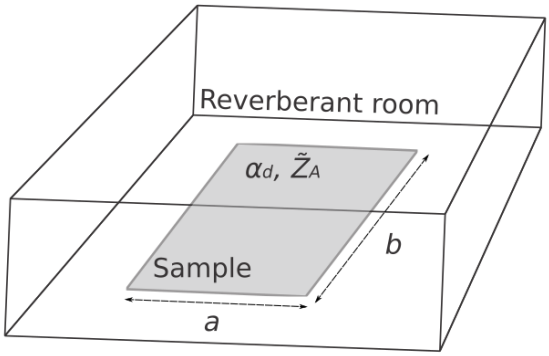

Figure 2.15: Ilustration of the test and parameters extracted from the experiments folowing the standard ISO 354.

Based on a variational approach Thomasson [1980], the angle dependent absorption for highly absorptive materials can be written as Vercammen and Lautenbach [2012]

$$\alpha(\omega, \theta, \phi) = \frac{4\mathrm{Re}(Z_A)/\cos(\theta)}{|Z_A + Z_R|^2}\ , \tag{2.63}$$

where Z_R is the normalized radiation impedance of the porous panel that also depends on a azimuth angle ϕ. The normalized radiation impedance for an infinite sample is $Z_{inf} = 1/\cos(\theta)$.

In a practical point of view, the noise control treatment is generally applied to sound fields that can be represented by plane waves impinging at the surface from several incidence angles. The sound absorption coefficient can be calculated from the integration over the angles between the normal incidence angle (zero rad) and the final angle θ_f, leaving out the critical grazing incidence angle ($\pi/2$ rad) to avoid the singularity in Equation 2.63. The random incidence sound absorption coefficient for a finite size sample becomes

$$\alpha_{fin}(\omega) = \frac{\int_0^{2\pi}\int_0^{\theta_f} \alpha(\theta,\phi)\sin(\theta)\cos(\theta)\mathrm{d}\theta\mathrm{d}\phi}{\int_0^{2\pi}\int_0^{\theta_f} \cos(\theta)\sin(\theta)\mathrm{d}\theta\mathrm{d}\phi}\ , \tag{2.64}$$

in which $\alpha(\theta, \phi)$ depends on Z_R, computed from Equation 2.63. In order to avoid high computational cost, Z_R for a given θ can be approximated by the average value over ϕ, then

$$Z_{R,avg}(\theta) = \frac{1}{2\pi}\int_0^{2\pi} Z_R(\theta,\phi)\mathrm{d}\phi. \tag{2.65}$$

In this case, Equation (2.63) becomes independent of ϕ by using $Z_{R,avg}$ and the random

incidence absorption coefficient can be calculated as an infinite sample as follows

$$\alpha_d(\omega) = \frac{\int_0^{\theta_f} \alpha(\omega,\theta)\sin(\theta)\cos(\theta)\mathrm{d}\theta}{\int_0^{\theta_f} \sin(\theta)\cos(\theta)\mathrm{d}\theta}\,. \tag{2.66}$$

The Gauss' quadrature can also be applied in Equation (2.66) for improving the computational efficiency.

The studied samples consist on a melamine foam with 4 different thicknesses and top area of 4x3 m^2. The macroscopic parameters used with the JCAL-Limp model Allard and Champoux [1992]; Johnson et al. [1987] are flow resistivity $\sigma = 12$, 1 kNs/m^4, porosity $\phi = 0.98$, tortuosity $\alpha_\infty = 1.0$, viscous $\Lambda = 115\,\mu$m and thermal $\Lambda' = 116\,\mu$m characteristic lengths, and finally the total apparent density $\rho_1 = 9.6$ kg/m^3. The results for single layer configurations was evaluated up to 5 kHz in one-third ocatave bands. The diffuse-field sound absorption coefficients are presented in Figure 2.16. Macroscopic parameters and experimental results were extracted from Pereira et al. [2021].

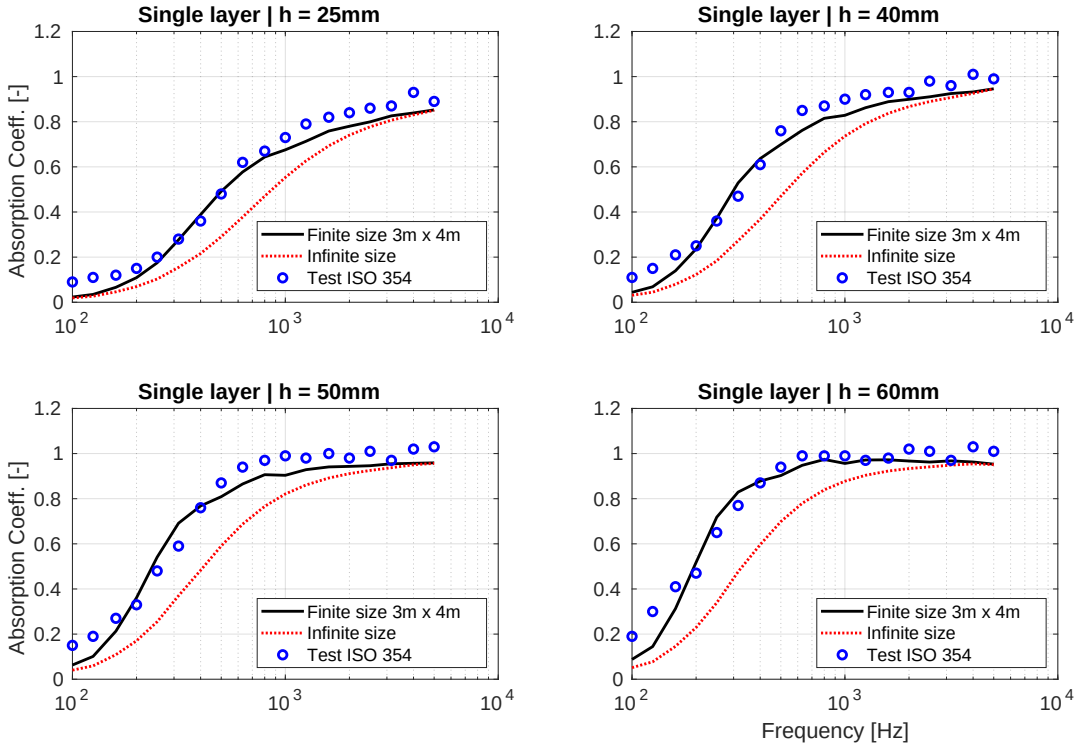

Figure 2.16: Simulated and experimental data for a 3×4 m^2 melamine sample.

Figure 2.16 shows the importance of considering the size effects in the calculation

of the sound absorption material when compared with diffuse field experimental data. It can be noticed that a simple integration over θ domain considering the infinite model is not capable of simulating properly the low frequency response of a reverberant test, due to the edge effects of the large sample. Figure 2.16 also shows an expected tendency of improving the sound absorption coefficient at lower frequencies for thicker samples if comparing 25 mm, 40 mm, 50 mm, 60 mm thick porous samples.

2.5.3.1 Numerical sensitivity

A numerical analysis was proposed for evaluating the efficiency of the presented approach. Four different meshes were generated containing 100, 200, 400 and 600 elements. The numerical convergence for each mesh was checked by varying the number of integration points in θ. The number of integration points in ϕ was fixed in 6, since the average value is less sensitive to the integration.

The global error ϵ between experimental and numerical data was calculated as

$$\epsilon = \sum_{i=1}^{N} \frac{|\alpha_i^{num} - \alpha_i^{exp}|}{N} , \tag{2.67}$$

where α^{num} is the numerical absorption coefficient, α^{exp} is the experimental data and N is the number of frequency points in analysis. The global error for the 60 mm thick sample and the solution time from an ordinary quad-core *i7* computer considering 15 frequency steps and all the integration processes are presented in Table 1 and 2, respectively.

Table 2.9: Global error between experimental and numerical results.

MESH	NGP			
	6	10	14	20
10 x 10	13.50%	6.77%	3.66%	3.64%
10 x 20	11.19%	3.66%	3.66%	3.64%
20 x 20	3.73%	3.66%	3.64%	3.64%
20 x 30	4.04%	3.65%	3.64%	3.64%

Table 2.10: Solution time for different meshes and integration points.

MESH	NGP			
	6	10	14	20
100 el.	1.06 s	1.84 s	2.82 s	5.27 s
200 el.	1.70 s	3.04 s	5.06 s	9.70 s
400 el.	2.60 s	5.24 s	9.75 s	18.94 s
600 el.	3.24 s	7.70 s	14.24 s	27.97 s

Table 1 shows the minimum error around 3.6% for the simulated data, but this value increases substantially for coarse meshes and small number of integration points in the space domain. The results for six Gauss points demonstrated poor performance for all the studied meshes. However, Table 1 also shown that the new tool reached the convergence for the minimum error when considering the proposed problems.

The time of resolution of the presented method (Table 2) proved the high computational efficiency of the numerical implementation. Bonfiglio et al. [2016] presented the analysis for diffuse sound absorption using different methodologies, and the minimum solution time obtained in that work was comparable to the implemented approach in this work.

The presented results shown that the size effects function of the developed SEA-module can provide a quick and representative estimation of the finite-size transfer matrix method for single-layer setups.

2.5.3.2 Multilayered systems

When applying an air gap in between the sample and a rigid wall, the efficiency of a sound absorber can be improved due to the distance of the material in relation to the boundary with minimum particle velocity. The higher is the wave propagation velocity into the absorbing layer, more relevant the thermal and viscous effects become in the energy exchanging. By using the transfer matrix approach, a double layer system composed by the melamine sample and an air gap was also approached. This analysis is an important contribution of this work, since single layer analysis are mostly considered in the literature (Mareze et al. [2019], Allard and Atalla [2009]).

Figure 2.17 shows the results for this configuration, if considering different thickness of the air and porous layers. Experimental results were extracted from a reference manual made available from BASF, a porous materials producer, for samples with

$h = 25$ mm and $h = 50$ mm thick backed by air gaps with thicknesses $h_g = 200$ mm and $h_g = 400$ mm. A technical manual that contains single and multilayer results for normal and diffuse incidence was made available in cooperation to this research BASF [2015]. In this simulation, 400 elements were used in the mesh. The total time of the solution was around 10.4 seconds.

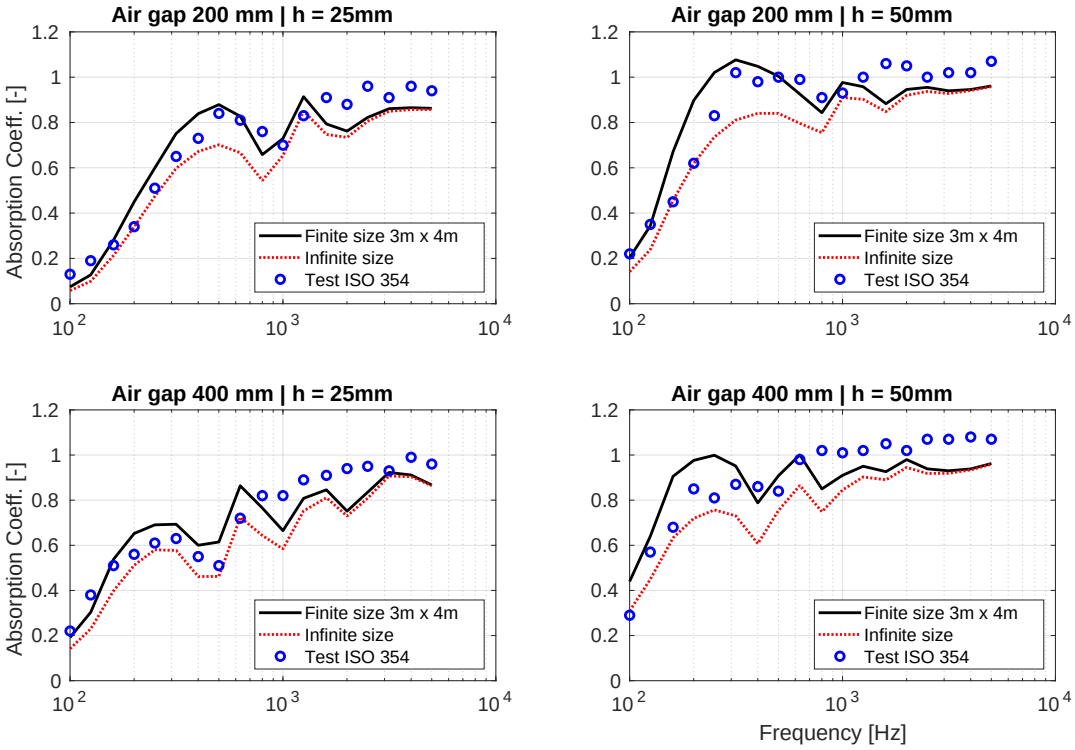

Figure 2.17: Simulated and experimental results for the double layer systems.

Figure 2.17 shows that the formulation of the FTMM is less representative of experimental procedures when considering multilayered panels. It can be seen that some analyses present the absorption coefficient grater than 1, which indicates that the surface area of the specimen is smaller than the absorption footprint, since the guidelines of experimental tests considers the ratio of the mean absorption by the specimen surface. This higher dissipation can be related to the edge/diffraction effects, Although less representative compared to single layer configurations, the finite-size corrected simulation demonstrated to be a better alternative than the infinite-size technique for modeling the diffuse field sound absorption coefficient of this multi-layer problem.

2.5.4 Numerical improvements on FTMM integral comparable to Integral2 function

Matlab's function Integral2 is generally used in academic studies concerning the finite-size absorption of porous samples Mareze et al. [2019]; Pereira et al. [2021]. In this section, this approach is compared to the developed numerical methodology already mentioned in Section 2.5.2.

In the following simulation, the sound absorption coefficient for the samples presented in Section 2.5.3 was solved using the proposed code and plotted against the results from the Integral2 code. The parameters for the Integral2 function were set to guarantee minimal convergence. Figures 2.18, 2.19, 2.20 and 2.21 show the results comparison and running time considering the in-house tool (*SEA-Module*) and Matlab's tool, plotted against the experimental data for 25 mm, 40 mm, 50 mm, and 100 mm sample thickness.

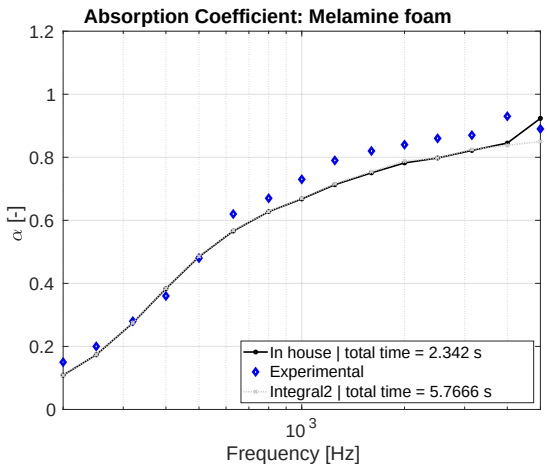

(a) NGP = 14.

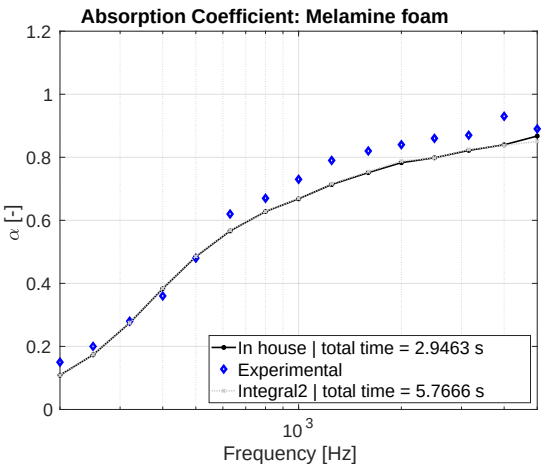

(b) NGP = 16

Figure 2.18: 25 mm.

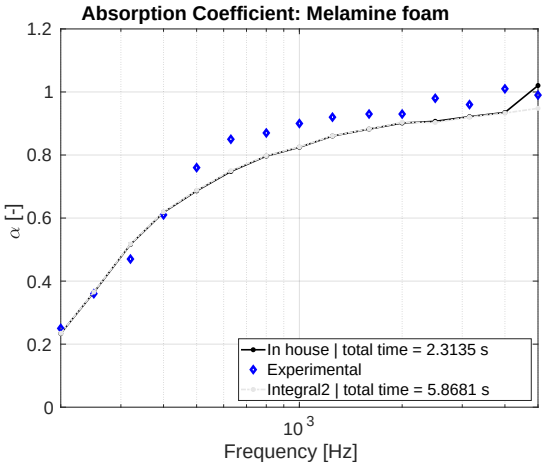

(a) NGP = 14.

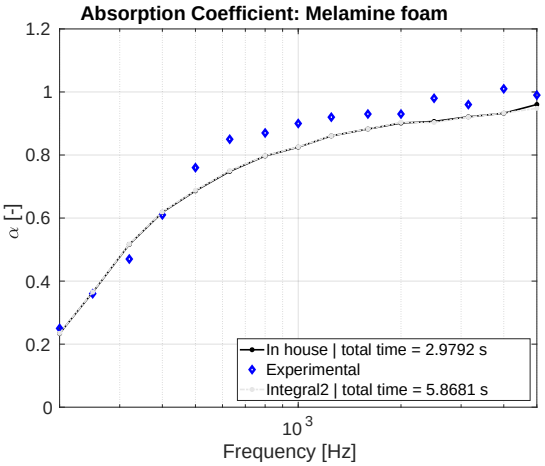

(b) NGP = 16

Figure 2.19: 40 mm.

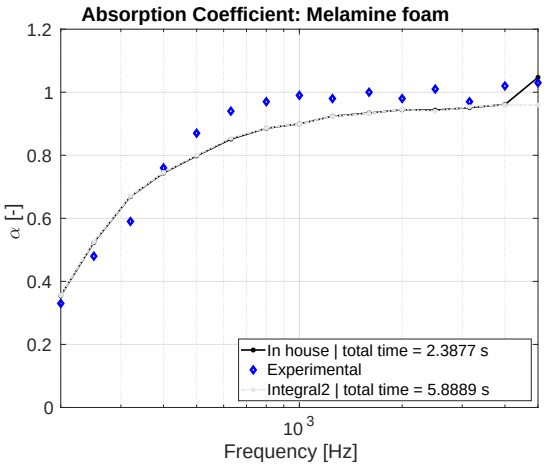

(a) NGP = 14.

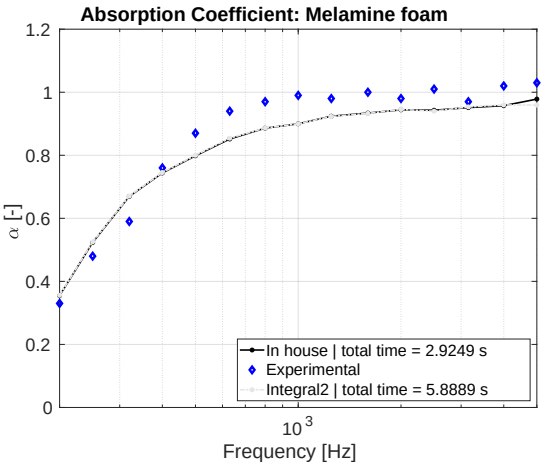

(b) NGP = 16

Figure 2.20: 50 mm.

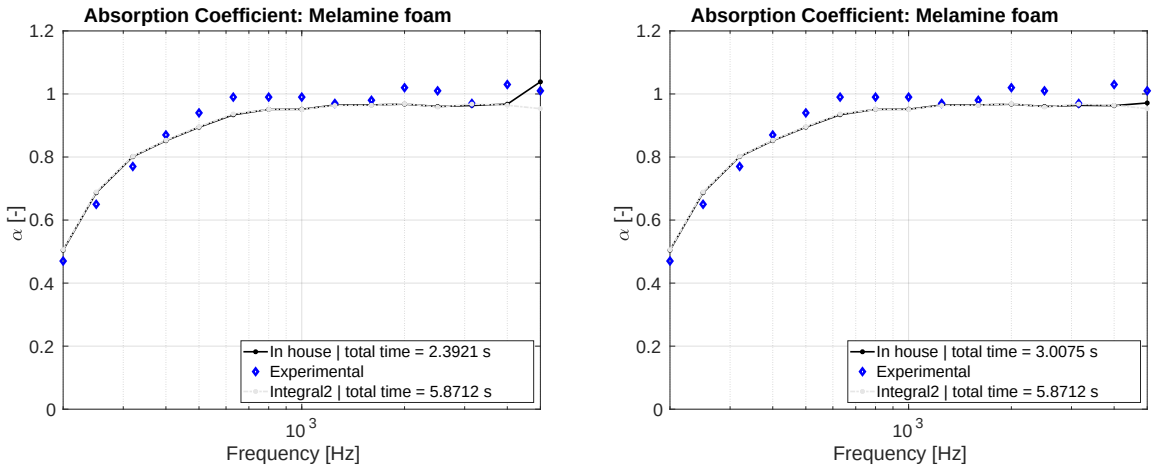

(a) NGP = 14. (b) NGP = 16

Figure 2.21: 100 mm.

Table 2.11 shows the mean CPU time and mean error numerical *vs* experimental considering all the runs of the selected samples.

Table 2.11: Mean time and mean error of all the runs.

Parameters	**In-house NGP = 14**	**In-house NGP = 16**	**Integral2**
Mean CPU Time	2.36 s	2.93 s	5.82 s
Mean Error (%)	4.7	4.7	4.7

Considering the proposed analysis, the following improvements was found:

- 60 % improvement of CPU time using NGP = 14 compared to *integral2*;
- 50 % improvement of CPU time using NGP = 16 compared to *integral2*;

2.5.5 Sound transmission of a finite size system

The sound transmission coefficient of a finite sample depends on the radiation efficiency of the system, which is the real part of the radiation impedance. Taking into account the analytical formulation presented in Section 2.5.1, the radiation efficiency can be represented by an average value relative to ϕ coordinate. Analogous to Equation (2.65),

the mean radiation efficiency is given by

$$\sigma_{rad,avg}(\omega,\theta) = \frac{1}{2\pi}\int_0^{2\pi} \text{Real}[Z_R(\theta,\phi)]\text{d}\phi. \tag{2.68}$$

The transmission coefficient of a finite size sample will be affected by the ratio of finite and infinite radiation efficiencies. It is known that the radiation impedance of an infinite size rectangular plate is real, represented by $Z_{inf} = \sigma_{inf} = 1/\cos(\theta)$. The transmission coefficient τ is

$$\tau_{fin}(\omega,\theta) = \tau_{inf}(\omega,\theta)\frac{\sigma_{rad,avg}(\omega,\theta)}{\sigma_{inf}(\theta)} = \tau_{inf}(\omega,\theta)\sigma_{rad,avg}(\omega,\theta)\cos(\theta) \tag{2.69}$$

where τ_{inf} is the infinite size transmission coefficient given by Equation (2.69) extracted from the TMM solution. Analogous to Equation (3.24), the diffuse field transmission coefficient is computed from the integration of the modulus of this parameter in θ domain

$$\tau_d(\omega) = \frac{\int_0^{\theta_f} |\tau(\omega,\theta)|^2 \sin(\theta)\cos(\theta)\text{d}\theta}{\int_0^{\theta_f} \sin(\theta)\cos(\theta)\text{d}\theta}\ . \tag{2.70}$$

Sound Transmission Loss TL is then computed from Equation (2.7).

In this section, the sound transmission loss of a a 3-layer sample is computed by using the finite-size transfer matrix method and the obtained results are compared to experimental data and statistical energy analysis (SEA) simulation. The experimental results are extracted from reference Villot et al. [2001], that also presents a technique based on spatial windowing of plane waves for considering finite size radiation. The system properties are given in Table 2.12.

Table 2.12: Material properties Villot et al. [2001].

	Solid		FOAM
	Steel 1	**Laminate 2**	**Mineral wool**
Thickness h [mm]	0.75	3	30
Young's Modulus E [Pa]	210E9	0.6E9	0.4E6
Poisson's ratio μ [-]	0.3	0.15	0
Density ρ [kg/m^3]	7850	1360	90
Damping [-]	3%	15%	18%
Flow Resistivity σ [kN/m^4]	-		34
Porosity ϕ [-]	-		0.955
Tortuosity α_∞ [-]	-		1.00
Viscous char. length Δ [μm]	-		40
Thermal char. length Δ' [μm]	-		80

The SEA simulation was done using an in-house code, which takes into account the Leppington's model Leppington et al. [1982] for the radiation efficiency of flat structures. The transmission loss in this case is computed from the energy of reception and source acoustic cavities in the model. More information about the SEA procedure is presented in another research work related to this project Oliveira [2020].

In this simulation, the foam was modeled using the Biot's Theory for poroelastic materials composed by a solid non-rigid skeleton and immerse in a fluid Biot [1956]. The laminate layer is considered as an equivalent solid so the solid formulation is applied Allard and Atalla [2009]. The results for the transmission loss of the plate-foam-lamite system are presented in Figure 2.22.

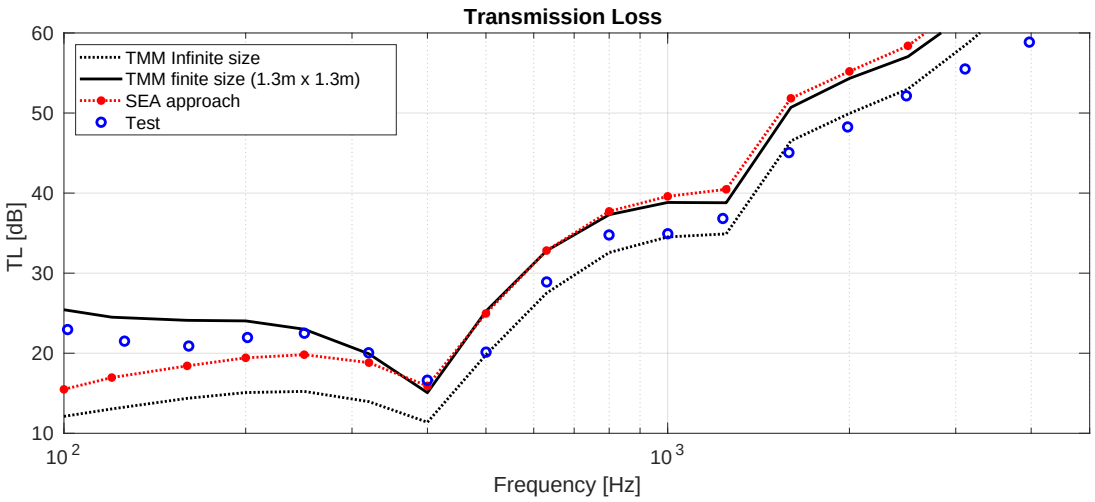

Figure 2.22: Transmission loss of a multi-layered system.

Figure 2.22 shows the better convergence of the simulated data at low frequencies when finite size correction is applied. For high frequencies, the radiation efficiency overestimates the sound transmission if comparing with experimental data, but the difference in this region of the spectra is relatively low. In general, the presented method is capable of correcting an important imprecision of about 10 dB if compared with the infinite model in low frequencies. The results from FTMM has also demonstrated better convergence than the results from the SEA method.

2.6 Summary

This chapter presented the noise control treatment models and numerical procedures to implement the Transfer Matrix Method. Numerical sound absorption coefficient was presented for different kind of modeling approach included in the developed computational tool, that considered fluid, solid and poroelastic layers.

The main contribution of this chapter refers to the validation of a new FTMM function on the computation of the sound absorption coefficient and transmission loss for finite size samples under diffuse field conditions. The exposed results demonstrated good agreement with experimental data, and the computational efficiency of the numerical approach presented in this section demonstrated good performance taking into account different implementation procedures available in the literature.

The evaluated indicators, as the diffuse field absorption and the transmission loss, can be used within the vibroacoustic modeling techniques framework to account for the effect of sound package in full system configurations, such as cars or aerospace models.

Chapter 3

Statistical Energy Analysis (SEA)

Partial content of this chapter was published in Reference Oliveira [2020].

Author	Thaynan A. Oliveira
Title	Numerical evaluation of the sound transmission of a structural system with attached noise control treatments using statistical energy analysis
Book	Proceedings of the International Conference on Structural Dynamics 2020
Editor	M. Papadrakakis, M. Fragiadakis, C. Papadimitriou

3.1 Introduction

Acoustical and structural systems are often found in engineering, whose importance of dynamic responses to random excitation is extended to high frequencies. Examples of such situations include:

- The calculation of sound pressure into a car;
- The structural response of an aerospace payload in flight;
- The vibration result of a structure under diffuse field conditions;
- The dynamical analysis of an aircraft structure (fuselage) due to jet noise and other dynamical sources;

Classical numerical methods, as the Finite Element Method and modal analysis, are suitable in the area of vibration and acoustics at low frequencies. For high frequency,

these tools cannot be used due to the small size of the wavelength, which requires a large number of degrees of freedom in the model and the high computational cost for obtaining the solution Fahy [1994]. For solving dynamical problems at high frequencies, statistical approaches has been developed. Statistical Energy Analysis (SEA) is one of them, which has proved to be a promising tool, mainly for solving acoustic and vibration problems in complex structures.

The SEA method allows the user to model a given system as an interaction of modes associated with isolated parts of the system (subsystems), considering each mode group as a single-degree-of-freedom oscillator described by his average energy response. The responses are obtained from the analysis of the energy distribution through the system, excited by a power source. This technique is based on the power balance equations for each mode group Lyon et al. [1995].

Some hypotheses are assumed in the determination of a model in statistical energy analysis. The most important is that the vibrational energy varies from a subsystem to another with a rate proportional to the difference between the modal energy and the dissipated energy into the subsystem. Another important hypothesis assumes the weak coupling condition, based on the magnitude of the coupling loss factors and the dissipation loss factors of the coupled subsystems, presented in the following sections Fahy [1994]. The weak coupling condition is valid if the internal dissipation of the subsystem is more important than the coupling path in the total loss of energy. This makes the ratio between the coupling factors and the internal dissipation factors considerably less than 1. Thus, the energy flow between the subsystems may be based on the difference between the energies of the decoupled subsystems Langhe [1996].

Additionally, it is important to ensure that the input powers are uncorrelated, and they can be simply summed. It guarantees the linearity of the equations that govern the SEA problem. Natural frequencies must also be distributed within the frequency range of interest, as well as the energy distribution is assumed to be egalitarian for all modes of a subsystem present in a given frequency band.

3.2 SEA equations

As it was previously mentioned, the system is divided in SEA into physical elements in which the vibroacoustic characteristics, such as damping, excitation and coupling properties, can be considered similar. Subsystems directly excited by external sources will transmit energy to the others by means of coupling characteristics. The main

mechanism in SEA is based on the relationship between power inputs and outputs from each subsystem. Figure 3.1 shows some simple problems that can be considered using statistical energy analysis.

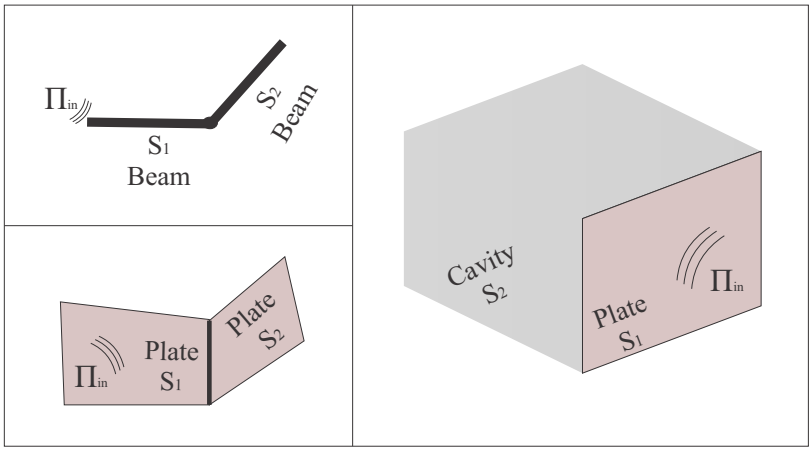

Figure 3.1: Examples of simple SEA problems.

Figure 3.1 shows the coupling of two SEA subsystems. However, it is common to have more robust models with a high number of elements. Considering a subsystem i coupled to a number of n subsystems, the power flow is

$$\Pi_i^{in} = \Pi_i^{\text{absorbed}} + \sum_{j \neq i}^{n} \Pi_{i;j}^{\text{transmited}} , \tag{3.1}$$

where Π represents the power in Watts. Equation (3.1) shows that there are a dissipated portion of the input power into a subsystem (controlled by the energy dissipation capacity of the media) and a transmitted portion of that, controlled by the coupling nature. If considering the simple problems exposed in Figure 3.1, the power flow can be illustrated by Figure 3.2.

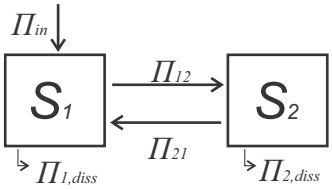

Figure 3.2: Two subsystems SEA flow.

It is possible to obtain the equations of the power flow illustrated in the Figure 3.2,

for each subsystem, as

$$\text{Subsystem 1:}\quad \Pi_{in} + \Pi_{21,trans} = \Pi_{1,diss} + \Pi_{12,trans} \tag{3.2}$$

$$\text{Subsystem 2:}\qquad \Pi_{12,trans} = \Pi_{2,diss} + \Pi_{21,trans}\ . \tag{3.3}$$

The power Π is related to the energy from

$$\Pi_i = \omega \eta_i E_i\ , \tag{3.4}$$

where ω is the angular frequency, η_i is the loss factor and E_i is the energy of a subsystem i. The dissipated and the transmitted power will be given by

$$\Pi_{i,diss} = \omega \eta_{i,diss} E_i \qquad [i = 1, 2]\ ; \tag{3.5}$$

$$\Pi_{ij,trans} = \omega \eta_{ij} E_i \qquad [i \neq j]. \tag{3.6}$$

with η_{ij} being the coupling loss factor that control the energy exchanging between two subsystems. Substituting Equation (3.5) and (3.6) into (3.2), considering the subsystems 1 and 2, the following linear system of equations is obtained

$$\omega(\eta_{1,diss} E_1 + \eta_{12} E_1 - \eta_{21} E_2) = \Pi_{in}\ , \tag{3.7}$$

$$\omega(-\eta_{12} E_1 + \eta_{21} E_2 + \eta_{2,diss} E_2) = 0\ . \tag{3.8}$$

It can be observed that the SEA method is based on the resolution of linear systems for calculating the energy in each subsystem. In the matrix form, the energy balance will be

$$\omega \begin{bmatrix} \eta_{1,diss} + \eta_{12} & -\eta_{12} \\ -\eta_{21} & \eta_{2,diss} + \eta_{21} \end{bmatrix} \begin{Bmatrix} E_1 \\ E_2 \end{Bmatrix} = \begin{Bmatrix} \Pi_{in} \\ 0 \end{Bmatrix}\ . \tag{3.9}$$

The determination of damping variables for complex subsystems is based on empirical/theoretical models or it comes from direct experimental data. For an area connection (plate-cavity), the transmitted powers by coupling between subsystems will depend on the radiation characteristics and differences between the environments. If the modal densities of the subsystems involved in the problem are known, the coupling loss factors in one direction is required, and the following consistency ratio can be used

to complement the damping matrix by assuming the symmetric SEA approach

$$n_i \eta_{ij} = n_j \eta_{ji} \ , \tag{3.10}$$

where n_i e n_j are the modal densities of the subsystems i and j, respectively. Therefore, it will be necessary to know the following parameters to solve the linear system exposed in Equations (3.9) and (3.10):

- The modal densities of subsystems;
- The dissipation loss factors;
- The coupling loss factors;
- The input power.

Next sections are briefly presenting the parameters related to area connections, which is the most important junctions concerning the application of noise control treatments in SEA.

3.2.1 Modal densities for structural plates and acoustic cavities

The mode count is very important in the SEA method, since it is responsible for representing the capacity to receive and store energy in the subsystem through the resonant modes. In this context, it is possible to highlight three main variables, as the number of modes N in a given frequency band and the modal density n which represents the changing rate of the number of modes as a function of frequency, that is Lyon et al. [1995]

$$n(\omega) = \frac{\mathrm{d}N}{\mathrm{d}\omega} \ . \tag{3.11}$$

The greater number of modes present in a frequency band will result in the creation of a larger number of stationary waves in the domain when excited by a broadband noise (having all frequencies), so it is evident that such parameters govern the energy storage in the concerned subsystem.

Among the SEA parameters, the modal density is usually the most common to be determined using analytical or experimental methods. In experimental terms, such parameter can be extracted from the real part of the mechanical mobility in the case

of structural subsystems, or from the real part of the average acoustic impedance to an acoustic subsystem. However, several analytical models are presented in theory for calculating modal density. For an acoustic cavity, as shown in Figure 3.1, the modal density will be given by

$$n_{cav}(\omega) = \frac{\omega^2 V}{2\pi^2 c^3} \ , \tag{3.12}$$

where V is the volume and c the fluid sound velocity.

For a 2-dimensional non-stiffened structure, there are also studies that identify its modal density commonly used in SEA codes. This parameter is given by

$$n_s(\omega) = \frac{Sk}{2\pi c_g} \ , \tag{3.13}$$

where k is the wavenumber and c_g is the group velocity for bending, longitudinal or shear waves Johansson and Comnell [2010].

An important factor related to the modal characteristics of the subsystem is the *Modal Overlap*. This parameter considers not only the modal density, but also the subsystem damping. It is known that the statistical analysis becomes adequate from the occurrence of a sufficient number of modes in the spectral band, however, a highly damped system may lose some resonant characteristics. The consideration of the damping, besides the modal density, is a qualitative tool to obtain the appropriate response range of analysis. The modal overlap can be calculated as Langhe [1996]

$$M(\omega) = \frac{\pi}{2}\omega n(\omega)\eta_T \ , \tag{3.14}$$

where the η_T is the total loss factor of the subsystem. High values of modal overlap result in small values of variance and narrow confidence intervals, and the mean response may be considered adequate. As a general rule, it is preferable that the parameter be greater than 1.

3.2.2 Coupling factors for cavity-plate area connections

The coupling between acoustic and structural subsystems Figure 3.1 is controlled by different propagation paths. The most important ones are controlled by the resonant and non-resonant sound transmission. The first one is affected by the radiation capacity of the structural system and is important in frequencies above the coincidence spectral region of the plate. On the other hand, the non-resonant path is controlled by the

mass of the structure and it is important for global responses below the coincidence frequency Beranek and Ver [1992]. The radiation loss factor that models the connection between plate s and cavity a is given by

$$\eta_{sa} = \eta_{rad} = \frac{\rho_a c_a S_s}{\omega M_s} \sigma_{rad} \,, \tag{3.15}$$

with ρ_a being the fluid density, c_a the fluid sound velocity, S_s the area of the partition, M_s the structural mass and σ_{rad} the radiation efficiency of the structural system that can be recovered in theoretical models as that one proposed by Leppington et al. [1982]. If a plate is modeled as the partition between two cavities, the non-ressonant loss factor that models the coupling between the two cavities i and j is

$$\eta_{ij} = \eta_{mass} = \frac{c_i A_i \tau_m}{4\,\omega\,V_i} \,, \tag{3.16}$$

where A is the total surface area, V is the volume of the cavity and τ_m is the mass controlled transmission coefficient of the system. The field incidence transmission coefficient can be used in this modeling strategy Beranek and Ver [1992].

3.2.3 Dissipation loss factor

The DLF is a dimensionless quantity that is usually related to other energy loss variables, depending on the physics involved in the system. By definition, it is given by the ratio between the dissipated power and the input power of the system, or

$$\eta_{diss} = \frac{W_{diss}}{W_{input}} \,. \tag{3.17}$$

In structural dynamics, one can highlight the relationship with the viscous damping factor $\zeta = 0.5\eta$. In acoustics, the loss factor can be related to the reverberation time of a subsystem, which is directly related to the energy decay as a function of time, or more common from the mean surface absorption of the subsystem Cockburn and Jolly [1968].

The representation of dissipative quantities are necessary as the experimental methods for characterization of systems are expanded and more natural forms of representing the energy loss arise. On acoustics, the reverberation time T_R can be measured directly from the average impulse response decay of a room. For a structure, it is very common to obtain the modal loss factor from the half-power bandwidth method from

a measured frequency response function. For simple structures, there are empirical data available in the literature that indicate the loss factor in certain systems. The dissipation loss factor of a solid plate can vary between 0.2 % and 3 % Wijker [2009].

3.2.4 Energy variables

With the parameters that govern the SEA equations, one can solve the linear system, as exemplified in (3.9), to obtain the average energy in each SEA subsystem. However, it is often necessary to present the results in function of representative dynamic variables. The energy response of a structural system in terms of the *rms* velocity, which is represented by Johansson and Comnell [2010]; Lyon et al. [1995]

$$< v_{rms}^2 >= \frac{E}{M} , \tag{3.18}$$

where M is the total mass of a subsystem (admitting uniform distribution).

For an acoustic subsystem, it is interesting to convert the average energy of the subsystem into sound pressure. This conversion will depend on the characteristic impedance of the medium and also on the volume of the cavity, so that Johansson and Comnell [2010]

$$p_{rms}^2 = \frac{E}{V}\rho_a c_a^2 . \tag{3.19}$$

It is also common to present this result in terms of the sound pressure level defined as

$$L_p \;=\; 10\log(p_{rms}^2/p_{\text{ref}^2}) , \tag{3.20}$$

where $p_{\text{ref}} = 2.10^{-5}$ [Pa] is the reference pressure which represents the auditory threshold for human beings at 1 kHz.

3.3 Case studies

A SEA model cavity-plate-cavity is approached in this section and the numerical results are compared with experimental data extracted from Kulakauskas [2016]. The SEA problem is composed by the flexural energy of the plate and longitudinal energy of the cavities. Figure A.2 illustrates the proposed example.

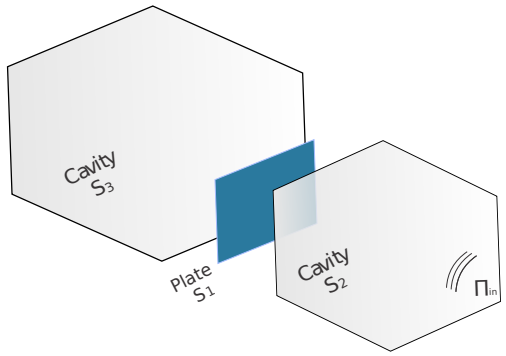

Figure 3.3: Example of a sound transmission loss problem.

The problem shown in Figure A.2 can be represented by the following linear system

$$\omega \begin{bmatrix} \eta_{1,diss}+\eta_{12}+\eta_{13} & -\eta_{12} & -\eta_{13} \\ -\eta_{21} & \eta_{2,diss}+\eta_{21}+\eta_{23} & -\eta_{23} \\ -\eta_{31} & -\eta_{32} & \eta_{3,diss}+\eta_{31}+\eta_{32} \end{bmatrix} \begin{Bmatrix} E_1 \\ E_2 \\ E_3 \end{Bmatrix} = \begin{Bmatrix} 0 \\ \Pi_{in} \\ 0 \end{Bmatrix} . \tag{3.21}$$

The mean square value of the pressure inside the cavities $p_i^2 = E_i \rho_i c_i^2 / V_i$ can be recovered from the solution, with ρ_i being the fluid density, c_i the sound velocity and V_i the volume of the cavity $i = 2, 3$. The transmission loss of the partition can be calculated as ISO:10140-2 [2010]

$$TL = 10 \log_{10}\left(\frac{p_2^2}{p_3^2}\right) + 10 \log_{10}\left(\frac{S}{A_{eq}}\right) , \tag{3.22}$$

where $A_{eq} = 4\omega V_3 \eta_{3,diss}/c_3$ is the equivalent absorption area of the reception cavity and S is the area of the panel, being V_3 the volume and c_3 the sound velocity of subsystem 3.

The emission (S2) and reception (S3) cavities have a volume of 147.54 m^3 and 199.0 m^3, based on the dimensions of the experimental reverberant chambers Kulakauskas [2016]. The total surface area A_1 and perimeter P_1 of the cavity S2 are 190 m^2 and 70.44 respectively. For the cavity S3, these geometrical dimensions are $A_3 = 210$ m^2 and $P_3 = 72.0$ m. The aluminum bare panel covers a whole lateral surface of the cavity with total surface area of $S_1 = 1.0$ m^2. Young's Modulus, density and Poisson's ratio of the structure are considered 71 GPa, 2700 kg/m^3, and 0.33, respectively. An acoustic power source of 1 Watt was applied in the S_1 subsystem. The total mean absorption of the non-treated surfaces of the cavities was considered 1%,

as well as the dissipation loss factor of the solid plate.

The results for the application case are given in one third-octave band, from 250 Hz to 8000 Hz. Figure 3.4 shows good agreement between numerical and experimental data for the considered single-wall system, which indicates a good implementation of the transmission loss modeling for flat structures using statistical energy analysis.

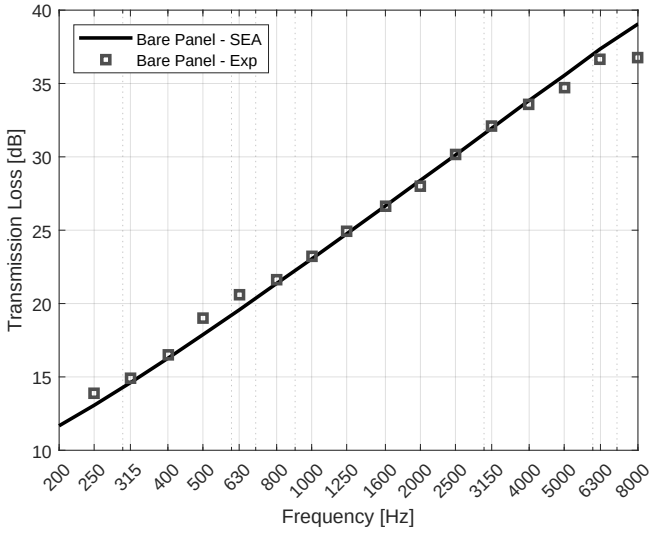

Figure 3.4: Sound transmission loss of an aluminum plate.

This model is resumed in the next sections, where noise control treatments are applied at the surface.

3.4 SEA/TMM coupling

This section presents how to coupling TMM simulation, well explained to the lectors in Chapter 3, with statistical energy analysis (SEA). In this context, three quantities are extremely important for characterization: the sound absorption coefficient (α), which acts on the mean absorption of acoustic cavities, the sound insertion loss (IL), that depends on the transmission coefficient of the treated and untreated subsystem, and the structural damping of the treated system which is characterized by the equivalent dissipation loss factor η.

3.4.1 Sound absorption from the TMM

The first important quantity to be presented in this section is the sound absorption coefficient. This amount represents the fraction of incident energy that is not reflected by the sample, related to the dissipation of energy into the NCT. The angle dependent absorption coefficient α for a sample backed by a rigid wall (see Equation (2.5)) can be also presented as Thomasson [1980]

$$\alpha(\omega,\theta) = 1 - |R(\theta,\omega)|^2 = \frac{4\mathrm{Re}(Z_A)/\cos(\theta)}{|Z_A + 1/\cos(\theta)|^2} \,. \tag{3.23}$$

where $Z_A = \tilde{Z}_s(\omega,\theta)/Z_0$ is the normalized surface impedance of the treatment. If considering random incidence, the sound absorption coefficient should be integrated over the angle being calculated as follows

$$\alpha_d(\omega) = \frac{\int_0^{\theta_f} \alpha(\omega,\theta)\sin(\theta)\cos(\theta)\mathrm{d}\theta}{\int_0^{\theta_f} \sin(\theta)\cos(\theta)\mathrm{d}\theta} \,. \tag{3.24}$$

where θ_f is the final angle value of the integration range. According to Beranek and Ver [1992], $\theta_f = 78°$ represents the field incidence, more indicated for comparing with reverberant chamber data. The Gauss' integration can be applied in Equation 3.24 for improving the computational efficiency.

The surface sound absorption is then used in the dissipation loss factor of the SEA cavity in contact with the surface of the treatment. This parameter is calculated by the following equation

$$\eta = \frac{cA_t\overline{\alpha}}{4\pi f V} \,, \tag{3.25}$$

where c is the fluid sound velocity, A_t is the total surface area of the cavity, V is the volume and $\overline{\alpha}$ the surface mean absorption, given by

$$\overline{\alpha} = \frac{\sum A_i \alpha_d^{(i)}}{A_t} \,. \tag{3.26}$$

where A_i is the absorbing surface area i (e.g. the application area of the NCT) with absorption coefficient $\alpha_d^{(i)}$.

3.4.2 Insertion Loss (IL) from the TMM

The Insertion Loss (IL) is defined as the ratio between the acoustic transmission loss (TL) of a panel with the attached treatment over the TL of the unteated panel. This parameter can be calculated from the TMM simulation if considering a semi-infinite fluid as the boundary condition (fluid in both sides). The insertion coefficient IC will be given by

$$IC(\omega) = \frac{\int_0^{\theta_f} |T_{NCT}(\omega,\theta)|^2 \sin(\theta)\cos(\theta)\mathrm{d}\theta}{\int_0^{\theta_f} |T_{bare}(\omega,\theta)|^2 \sin(\theta)\cos(\theta)\mathrm{d}\theta} \ , \tag{3.27}$$

where T_{NCT} and T_{bare} are the transmission coefficients of the treated and untreated systems, respectively. T_{bare} is computed by runing the TMM problem with a single plate layer, while T_{NCT} is solved considering plate + treatment. The insertion loss $IL(\omega) = -10\log_{10}(IC(\omega))$ is recovered from the insertion coefficient. Finally, this parameter is applied as a scaling factor to the radiation and the mass law coupling loss factors in the SEA problem Atalla [2017], then

$$\eta_{rad} = \eta_{rad}\, IC(\omega) = \eta_{rad}(10^{-IL(\omega)/10}) \ ; \tag{3.28}$$

$$\eta_{mass} = \eta_{mass}\, IC(\omega) = \eta_{mass}(10^{-IL(\omega)/10}) \ . \tag{3.29}$$

The model presented in Figure A.2 is considered again in this section, but different configurations are tested for the bare panel using the TMM approach. A single layer porous treatment is implemented in Setup 1, and a double layer (porous material + solid plate) is considered in Setup 2, which characterizes a double wall configuration, as illustrated in Figure 3.5. In this work, the single and double-wall setups were reproduced in the new code (*SEA-Toolbox*) using two different porous samples, considering the SEA implicit approach. It means that the multi-layer structures were represented by applying the obtained Insertion Loss from the TMM analysis to the SEA coupling factors (see Equations 3.15 and 3.16).

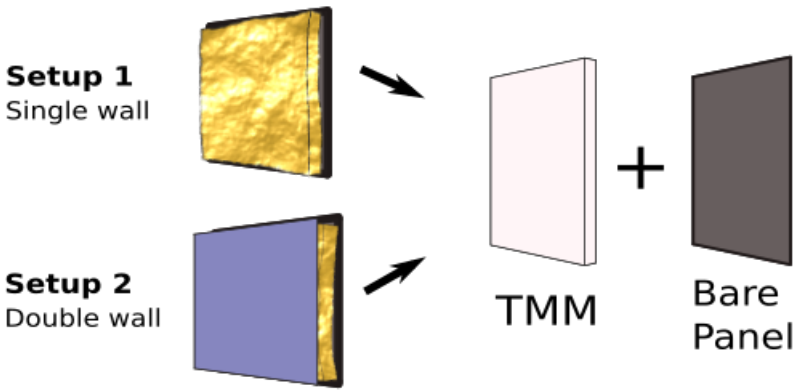

Figure 3.5: Ilustration of the simulated systems.

Based on the experimental procedure, the porous samples were modeled as simply supported limp fibers. The JCA model Allard and Champoux [1992]; Johnson et al. [1987] was used for the characterization of the fluid part in addition to the equivalent density calculated from the simplification of the Biot's Theory for low-stiffness framed materials Allard and Atalla [2009]. This approach avoids artificial clamping between the plate and the porous material, but in case of using the full Biot's Theory (poroelastic material), an air gap should be applied between the structure and the foam to simulate the cited mounting condition. The properties for the solid structures and fibers considered in this work are presented in Table 3.1.

Table 3.1: Materials in this test case simulation Oliveira [2020].

	Solid		**Porous**	
	Plate 1	**Plate 2**	**Material A**	**Material B**
Thickness h [mm]	1.0	0.5	50	58
Young's Modulus E [Pa]	71E9		-	-
Poisson's ratio ν [-]	0.33		-	-
Density ρ [kg/m^3]	2700		27	9.6
Flow Resistivity σ [kN/m^4]	-		5	38.72
Porosity ϕ [-]	-		0.89	0.92
Tortuosity α_∞ [-]	-		1.37	1.06
Viscous charac. length Δ [μm]	-		213	37
Thermal charac. length Δ' [μm]	-		288	148

Figure 3.6 shows the calculated insertion loss (IL) for single and double wall configurations by using a bare plate (Plate 1) and an equivalent fluid porous model.

An extra plate (Plate 2) is added at the extremity of the porous material to simulate the double wall setup. The simplified MATLAB/OCTAVE code for resolution of this problem is presented in Appendix A. Material properties are given in Table 3.1. Since the treated acoustic surface is too small if compared to the total surface area of the reception cavity, the mean absorption of the subsystem 3 would not be significantly altered in this scenario. On the other hand, the loss factor of the structural system can be important for the sound transmission on frequencies above the critical frequency ($\approx$ 12 kHz) for this panel. Therefore, the Insertion Loss (IL) of the treatment is the only parameter that contributes significantly to the numerical transmission loss of the complete system.

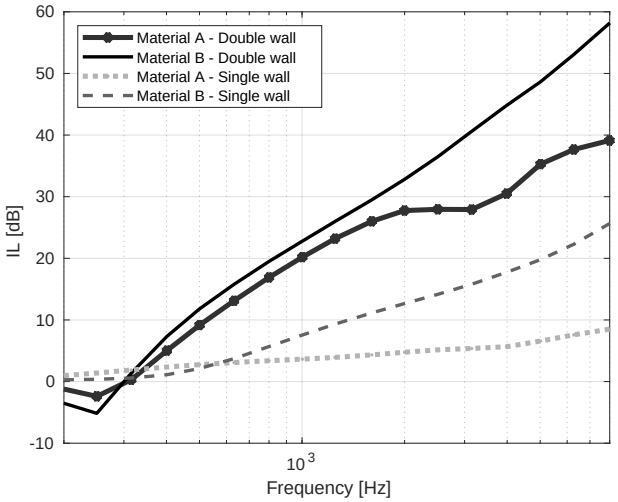

Figure 3.6: Insertion Loss IL obtained from the TMM solver for single and double wall configurations Oliveira [2020].

It can be noticed in Figure 3.6 that the formulation of transfer matrices is capable of capturing the poor performance of the double-wall configuration in frequencies below the resonance of the spring-mass system ($f \approx 300$ Hz), represented by a negative value of the IL. An example code of these insertion loss results applied to a simple SEA simulation is presented in Appendix A. These results also show the importance of the flow resistivity parameter for improving the Insertion Loss of the system, which is expected since this parameter controls the barrier capacity of the porous material. The Insertion Loss was applied to the coupling factors, as presented in Equations 3.16 and 3.15. The Transmission Loss results calculated for the single-wall configurations (plate + porous) are presented in Figure A.3.

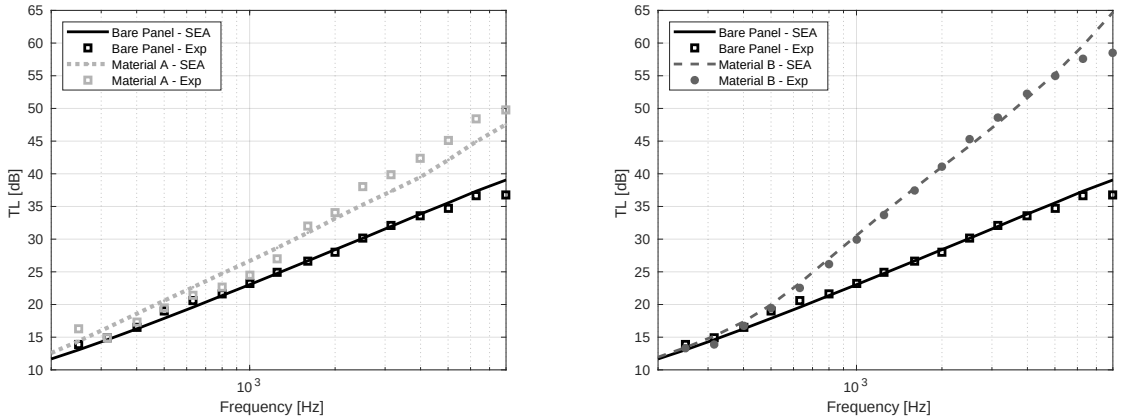

(a) Material A (b) Material B

Figure 3.7: Sound Transmission Loss obtained for the single-wall configurations.

Figure A.3 shows good agreement between numerical and experimental data for the considered single-wall systems, which indicates the efficiency of the presented modeling approach for flat structures. It can be noticed in the obtained result for Material B the drop of TL in high frequency that probably occurs due to the leakage of the sound wave in the experimental condition. This characteristic is more evident in Figure 3.8, that brings the collected Transmission Loss for the double-wall setups (plate - porous - plate) with and without the leakage correction applied to the numerical data.

A propagation way that can be important in experimental procedures is the leakage due to the mounting conditions. According to Beranek and Ver [1992], this phenomena causes a reduction in the Insertion Loss that can be simply modeled as

$$\Delta IL_L = IL_s - IL_L \approx 10 \log_{10}(1 + \beta\, 10^{TL_s/10}) \tag{3.30}$$

where IL_s and IL_L are the insertion losses of the sealed and leaky systems, TL_s the transmission loss of the system and β is the leak ratio factor. Experimentally, the influence of this phenomena becomes more important in high frequencies Kulakauskas [2016]. In this section, the application of the model presented in Equation 3.30 was evaluated in the Transmission Loss of the double wall systems, considering $\beta = S_{leak}/S_{plate} = 2.0\,\mathrm{E} - 6$. The determination of S_{leak} was done by adjusting experimental data.

Figure 3.8 shows that the greater the complexity of the multilayers, the more difficult it becomes to obtain a perfectly sealed condition from an experimental point of view. It can be seen in Figures 3.8 (a) and 3.8 (c) that the experimental TL of the

different systems converges in high frequencies even though it does not occur when the same samples were used in the single-panel setups. It suggests greater importance of leaks in the double wall configurations. Although adjusting the parameter β imposes uncertainties, Figures 3.8 (b) and 3.8 (d) shows that the use of a model for considering this propagation path is necessary when the presence of leaks becomes evident in the experimental results. Nevertheless, the method of SEA/TMM can be a useful tool when due care is taken.

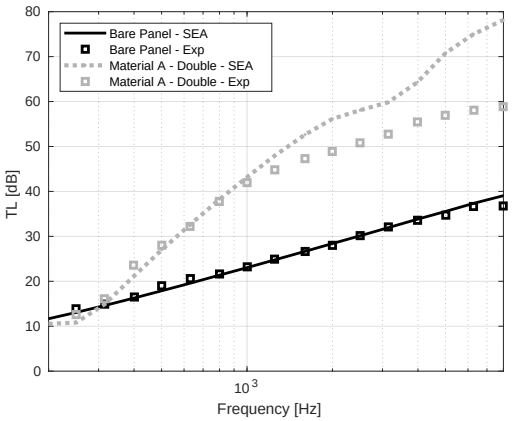

(a) Material A - without correction β

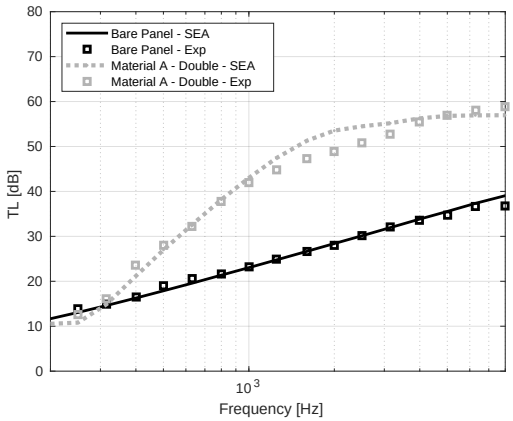

(b) Material A - with correction β

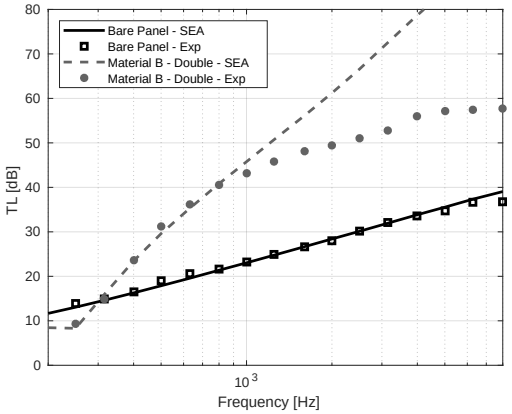

(c) Material B - without correction β

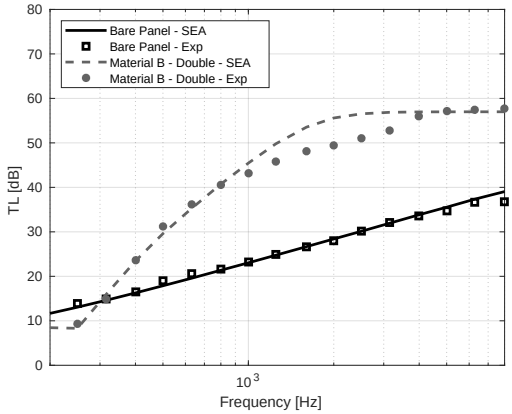

(d) Material B - with correction β

Figure 3.8: Sound Transmission Loss obtained for the double-wall setups.

This section presented an overview of the transmission loss characterization of multilayered structures using Statistical Energy Analysis and the Transfer Matrix Method. The Insertion Loss of the treated systems was calculated by using the TMM and applied to the coupling loss factors of the SEA matrix. Additionally, a model for leaks was presented and applied to the TL results for simulating experimental

conditions of a double-wall system composed by plate-porous-plate. The results obtained from the $SEA-Toolbox$, an open-source code developed in the present project, demonstrated good agreement with experimental data.

3.4.3 Damping loss factor from TMM

When the subsystem is excited by structural forces, it is also possible to apply a noise control treatment in the simulation by using transfer matrices by assuming light coupling between structure and the sound package. In this scenario, the response of the treatment will be modeled as an equivalent loss factor that should be added to the dissipation factor of the solid plate Rhazi and Atalla [2010]. The TMM simulation of this problem consists in a bare plate + NCT system backed by a pressure release boundary condition as ilustrated in Figure 3.9. The propagating wave-number in this case is not angle dependent by assuming normal structural excitation, then $k_t = k_b$ where k_b is the bending wavenumber of the structural system Atalla [2017]. A total loss factor $\eta_{tot} = \eta_s + \eta_{eq}$ represents the equivalent treated SEA subsystem, where η_s is the loss factor of the single solid plate.

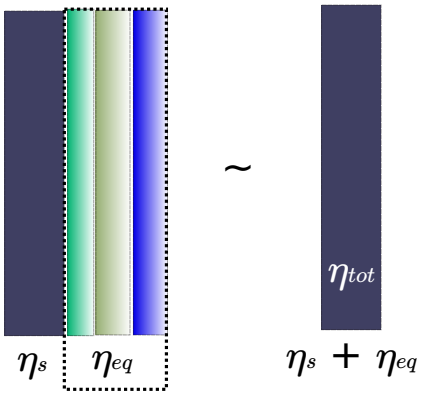

Figure 3.9: Ilustration of a treated panel represented by structure and equivalent loss factors Rhazi and Atalla [2010].

The equivalent loss factor is computed from the ratio between the input power and dissipated powers of the plate which can be extracted from classical SEA power balance equations (see Equation (3.4)). This energy parameter can be written as

$$\eta_{eq} = \frac{\Pi_{input} S}{\omega M < v^2 >} \tag{3.31}$$

where S is the surface area, M is the total mass and $< v^2 >= (v_0/2)^2$ is the mean

square velocity of the SEA bare plate (also applied to the TMM simulation). The Π_{input} is computed from

$$\Pi_{input} = \frac{\mathrm{Re}(p(\omega)\ v0^*(\omega))}{2} \tag{3.32}$$

where p represents the normal pressure at the bare panel rear side, which is obtained after the solving of a full TMM linear system, and v_0 is the input amplitude velocity applied at the front side. As the input excition is a normal incidence wave, the pressure and velocity parameters do not depend on the angle in this situation. Figure 3.10 shows the velocity level of a Plate-FOAM system when the foam is modeled as (a) an equivalent flui and (b) a poroelastic material. The SEA simulation is compared to full FEM simulation extracted from Rhazi and Atalla [2010].

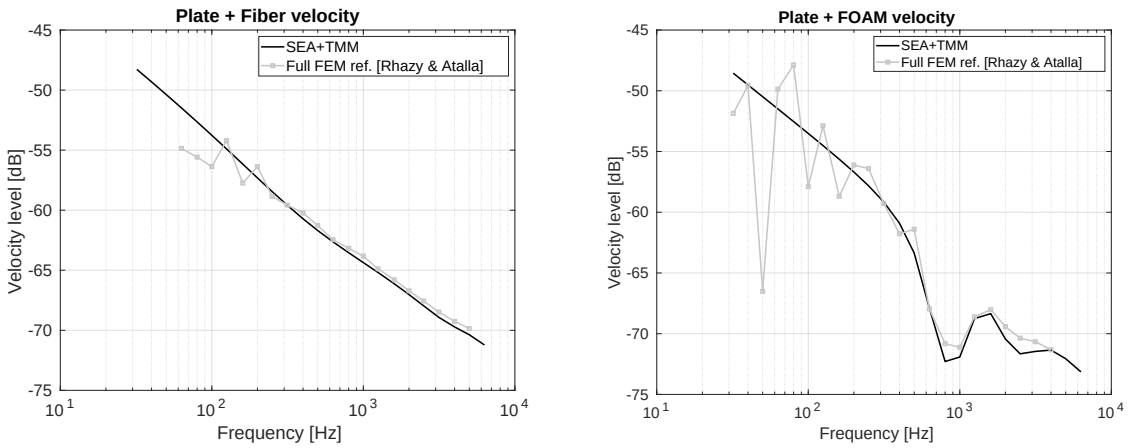

(a) (b)

Figure 3.10: Velocity level of a plate+NCT system: comparison between SEA/TMM and full FEM analysis from Rhazi and Atalla [2010].

It can be seen in Figure 3.10 that the statistical method is not capable of capturing the modal effects in the velocity response at low frequencies. At high frequency, the method shows good agreement with the deterministic result.

3.5 Summary

This chapter presented a technique to include Transfer Matrix Method data in a vibroacoustic model, which is useful in the automotive and aerospace industries for high-frequency analysis. The Statistical Energy Analysis (SEA), a classical method based

on the energy exchanging between subsystems, was introduced and discussed.

Three indicators are involved in the application of an NCT at a surface: the insertion loss (IL), the sound absorption coefficient, and the damping loss factor. The first one is important when a trim is applied at a structural partition since this parameter models the sound transmission loss capacity of the system. The second mechanism is related to the damping of the acoustic media in contact with the surface of the NCT. The application of this kind of treatment in a small room, for example, tends to increase the mean absorption that changes the reverberating characteristics of the acoustic environment. Finally, when the treatment covers the surface of a vibrating solid, the structural damping loss factor is also increased by the equivalent damping of the trim.

The main contribution of this chapter is the presentation of a modeling approach that provides the coupling between the TMM method and SEA for solving acoustic-structural problems with trimmed subsystems. These equations were implemented in the SEA-Module providing a full capacity of applying noise control treatments in SEA palte-cavity connections. Practical results were compared with experimental and numerical reference data.

Chapter 4

Hybrid methods on vibroacoustics

4.1 Introduction

Vibroacoustics deals with the interaction between sound waves and vibrating structures. In this context, the structure can be excited by point or distributed mechanical charges and acoustical loads (e.g. plane waves, diffuse acoustic field, or elementary acoustic sources). Mechanical vibrations on a solid and the acoustic pressure field in a fluid medium are influenced by the mutual interaction of vibroacoustic coupling at the fluid-structure interface. The loading on the structure caused by sound pressure will induce vibration and, analogously, the movement of the vibrating plate will influence the internal sound field of the fluid Fahy [2000].

In computational vibroacoustics, three classifications can be highlighted regarding the type of problem: interior, exterior, and interior/exterior modeling technique. In interior analysis, the fluid is confined, composing an acoustic cavity, and the fluid-structure coupling will depend on both geometry and fluid properties. In this case, it is common to use the finite element method for both domains (structural and acoustic) as a deterministic approach. The coupling in the outer problem, where the domain is not delimited, is governed by the mass of the structure as well as the properties of the external fluid. Such an approach, according to Atalla and Sgard [2015], describes radiation and scattering problems which are commonly modeled in terms of the Boundary Element Method (BEM). Therefore, external problems can be treated with hybrid alternatives by using deterministic approaches such as FEM/BEM or methods that include finite elements and statistical energy analysis (SEA) tools, well known as the Hybrid FE/SEA approach.

For a vibroacoustic system, Smith Jr [1962] presented the diffuse-field reciprocal relation for structures whose response can be described by a single degree of freedom, which indicates that the blocked force on a resonant structural mode under diffuse acoustic field conditions is proportional to the resistive radiation impedance of that mode, radiating in free space. This statement provides therefore to characterize a structural blocked force acting at the structure under diffuse field excitation based on an anechoic (direct field) formulation.

In 2005, Shorter and Langley [2005a] expand Smith's proposition, proving that this relationship can be used for connections having an arbitrary number of degrees of freedom. This study is the basis of the Hybrid FEA-SEA method Shorter and Langley [2005b], which allows considering the contribution of a statistical response in the dynamic equations of a deterministic problem, by using the direct-field dynamic stiffness matrix (D_{dir}).

This chapter presents two modal methods for calculating the referred parameter and compares the numerical efficiency of the solvers developed in this work. The first method is a classical space-domain integration based on Rayleigh's equations Rayleigh [1896] applied to the structural modes of the deterministic subsystem. The second one is a wave-based approach that considers wavelet basis functions independent of the physical parameters of the structure Langley [2007].

4.2 The Finite Element Method applied to hybrid techniques

The finite element method (FEM) has been a widely used numerical prediction technique for solving engineering problems Bathe [1982]. This method consists of determining the field variables distribution in a given domain, governed by a set of equations and appropriate boundary conditions. Acoustic cavities and elastic walls, for example, can be studied in a vibroacoustic FE model submitted to harmonic or random excitation loads.

FEM consists of discretizing complex domains to represent the system by a group of subdomains called elements, which generally have simple primitive geometries in one, two or three dimensions. For each element, nodal points are defined and point responses are approximated based on the weak (or variational) formulation of the physical problem. Nodes can be shared between subdomains since the continuity conditions between

elements can be satisfied Atalla and Sgard [2015]. From the nodal degrees of freedom and the element interpolation functions it is possible to compose the elementary matrix to be assembled in a global matrix by means of the element connectivity. The numerical solution is obtained from the resolution of a system of equations.

The element types to be considered in this work are called isoparametric, that is, the geometric interpolation along the element and the interpolation of nodal variables are given by the same functions Desmet and Vandepitte [2002]. Such elements are usually linear or quadratic, depending on the order of the shape functions that describe the approximation, but it is also possible to implement high order elements, with a larger number of nodes. An element having two nodes in a given dimension will be described by linear interpolation functions, while in the case of three nodes it will be approximated by quadratic functions. Quadratic elements, therefore, have more point response and, consequently, demand a higher computational cost. It is important to highlight the 3-node triangular linear elements for discretization of the structural domain of shells, as well as the linear tetrahedral (4-node) or quadratic (10-node) acoustic element as presented in Figure 4.1.

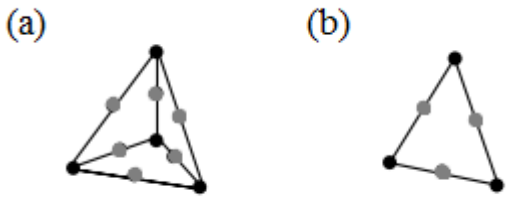

Figure 4.1: (a) 3D tetrahedral element. (b) 2D triangular element. Adapted from Hambric et al. [2016].

Among the factors that can affect the quality of the solution is the error due to discretization problems. Such error is induced by the creation of the mesh and by the approximation used for the geometry and the solution (type of elements, mesh density and geometry acuity). The size of the elements must be small enough to generate good results. However, care must be taken to avoid prohibitive computational time or exceed the available memory size. Smaller elements must be considered if the analyzed quantity changes abruptly along the studied domain. Larger elements can be used where the solution is expected to not vary greatly. In practice, the choice of the number of elements is dictated by the element type (linear, quadratic) and the maximum frequency of interest. Typically, in vibroacoustics, a minimum convergence criterion

for structural and fluid domains is the use of at least six elements per wavelength, considering linear elements, or four elements per wavelength for quadratic elements Desmet and Vandepitte [2002].

In vibroacoustics, developed formulations in terms of structural modes and rigid cavity wall modes in large systems are generally used, which results in a significantly lower computational cost using efficient algorithms to solve the eigenvalue problem. In this section, the finite element method is presented and different methods of solution are investigated.

4.2.1 Response to random excitations

Even though the system is deterministic, typical loads in aerospace systems, such as acoustic excitations or turbulent boundary layer (TBL), are random. These types of excitation can be better described by their static properties, highlighting the power spectral density. The sound pressure on the surface of a structural system can be transformed into a vector of spatially correlated forces. Random excitement will be characterized by

$$S_{ff} = S_{ff,ij}(\omega) = \int_{-\infty}^{\infty} R_{ff,ij}(\tau)\, \mathrm{e}^{\mathrm{j}\,\omega\tau}\, \mathrm{d}\,\tau \tag{4.1}$$

where $R_{ff,ij}$ is the cross-correlation function described by

$$R_{ff,ij} = \lim_{T\to\infty} \frac{1}{T} \int_{-T/2}^{T/2} f_i(t) f_j(t+\tau)\ opdt \tag{4.2}$$

The index ff denotes the spectrum crossed along the degrees of freedom i and j of the vector of external forces F. In other words, in a multi-degree-of-freedom system, $[S_{ff}]$ will be described by a matrix containing the power spectral densities of the exciter forces applied to the various degrees of freedom of the system Nieuwenhof et al. [2008], that is

$$S_{ff}(\omega) = \begin{bmatrix} S_{f1f1}(\omega) & S_{f1f2}(\omega) & \dots & S_{f1fn}(\omega) \\ S_{f2f1}(\omega) & S_{f2f2}(\omega) & \dots & S_{f2fn}(\omega) \\ \vdots & \vdots & \ddots & \vdots \\ S_{fnf1}(\omega) & S_{fnf2}(\omega) & \dots & S_{fnfn}(\omega) \end{bmatrix}. \tag{4.3}$$

The randomly excited system response will be described by the response spectral density matrix obtained through Peiffer [2016]

$$S_{xx} = D^{-1}(\omega) S_{ff} D^{-H} \tag{4.4}$$

where $[.]^H$ indicates the Hermitian conjugate of the dynamic matrix.

4.2.2 Modal finite element method

The application of the finite element method in real acoustic engineering problems usually involves large models and requires a large amount of memory allocation and computational efforts. However, model sizes and consequently computational efforts must be substantially reduced when the modal expansion technique is used.

High discretized systems have large global matrices in terms of dimension, which implies a long resolution time for obtaining a direct solution. Physical coordinates can be represented by a set of modal vectors and its respective amplitudes in the reconstructed vibration pattern, which means that the linear dynamic behaviour is given by a superposition of its natural properties.

The modal response approach considers the expansion of dynamic variables in terms of the modes of the considered system. The calculation of the modal forms of an interior acoustic or structural system, in which the boundary surface is assumed to be perfectly rigid, is obtained without taking into account the damping matrix and the external excitation vector in the finite element model. As stiffness and mass matrices are frequency independent, the calculation of modal forms is done from the following eigenvalue problem,

$$[K_a]\{\Phi_a\} = \omega_m^2[M_a]\{\Phi_m\} \quad (m = 1..n_a) \tag{4.5}$$

where n_a denotes the number of degrees of freedom of the acoustic problem and each eigenvector $\{\Phi_a\}$ $(n_a \times 1)$ represents a modal form, with the associated eigenvalue corresponding to the square of natural frequency that way. Likewise, the modal forms of the *in vacuo* problem for the structural system is given by

$$[K_s]\{\Phi_s\} = \omega_m^2[M_s]\{\Phi_m\}. \tag{4.6}$$

In dynamic analysis, the frequency response of a complex linear vibratory system can be described completely from the superposition of an infinite number of modes (base functions). Not only in mechanics, but this premise is also valid for other physics and domains, such as in linear signal analysis, where the representation of a complex signal (having several spectral components) is given from the superposition of harmonic signals (frequency only).

The possibility of obtaining, therefore, a relatively precise answer from a truncation of modes are taken into account and significantly reduces the number of degrees of freedom of the forced problem. Even so, the extraction of eigenvalues and eigenvectors (modal response) takes into account the number of elements in the mesh, however, the free vibration analysis involves less complexity of resolution in computational terms. This is evident in the case of a forced analysis.

When undamped modes are considered, the eigenvalue problem is

$$(K - \omega^2 M)\{u\} = \{0\} \ , \tag{4.7}$$

where u is the displacement, K and M are the stiffness and mass matrices of the system, respectively. If the undamped modes of the system are known, the mass normalized movement equation in modal domain can be written as

$$\left(-\omega^2 \left[\mathrm{I}\right]_{N\times N} + [\omega_m^2]_{N\times N}\right) \{U_m\}_{N\times 1} = \{F_m\}_{N\times 1} \ , \tag{4.8}$$

where m is the mode index, N is the total number of modes in the analysis, U_m is the modal displacement, $[\omega_m^2]$ is a diagonal matrix of squared modal frequencies (or eigenvalues) and F_m is a vector which contains the external modal loads. An equivalent damping can be implemented in terms of a complex dynamic stiffness which is controlled by a modal loss factor η_m leading to

$$\left(-\omega^2 \left[\mathrm{I}\right]_{N\times N} + (1 + \mathrm{j}\,\eta_m)[\omega_m^2]_{N\times N}\right) \{U_m\}_{N\times 1} = \{F_m\}_{N\times 1} \ , \tag{4.9}$$

The term on the left hand side multiplying the modal displacement U_m is also called modal dynamic stiffness matrix in the following sections. Figure 4.2 shows the *rms* velocity of a single plate if comparing full solution or modal solution.

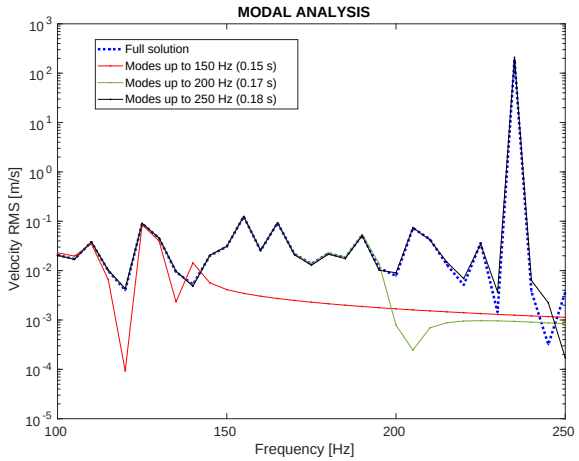

Figure 4.2: *RMS* velocity of a flat plate considering different number of modes in the simulation.

4.2.3 Hybrid FE-SEA

The FEM-SEA modeling considers that the deterministic domain is represented by a group of degrees of freedom (either nodal or modal), whereas the representation is given by the energy level in the statistical analysis. The coupling between these two types of description makes up the central idea of the technique. A force generated from the reverberant part represented by the SEA subsystem in contact of a FE structural system can be calculated from a relationship between acoustic energy and radiation characteristics of the degrees of freedom of the deterministic model, represented by a direct field matrix. Figure 4.3 illustrates the hybrid junction between a FE plate and a SEA cavity subsystem.

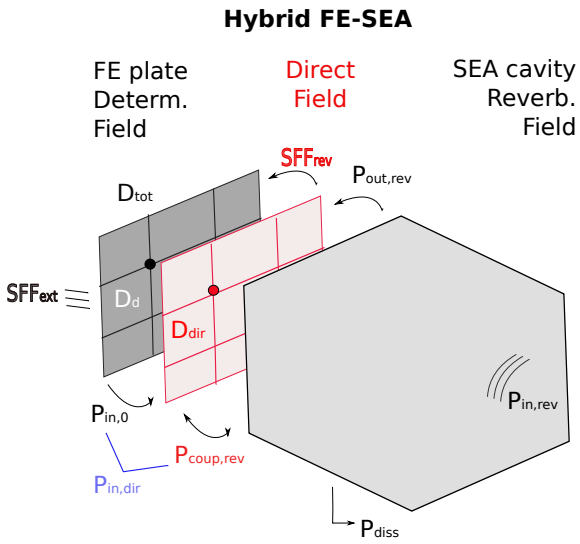

Figure 4.3: Illustration of a FE structure with a SEA cavity model.

Figure 4.3 presents six power variables that controls the SEA power balance in the statistical part of the problem. $P_{in,0}$ represents the input power from the external excitation of FE system, $P_{coup,rev}$ is the power controled by the coupling loss factor of the hybrid junction, and $P_{in,dir}$ is the total input power from the direct field, which will be given by a combination of the external power and the coupling power. The dissipated power P_{diss} and reverberant input power $P_{in,rev}$ controls the SEA damping and the SEA excitation, therefore they are not related to the hybrid junction but to the individual statistical subsystem. $P_{out,rev}$ is the output power that will represent the SEA contribution to the reverberant force to be applied back in the FE part.

The power spectral density of the force imposed on the structure through the application of the SEA subsystem depends on the internal energy of the statistical part and the energy storage capacity in the frequency represented by the modal density parameter. The imaginary part of an impedance parameter complements the excitation from the fluid to the structural part, which results in

$$S_{ff,rev} = \left(\frac{4E_{tot}}{\omega \pi n_{tot}} \right) \mathrm{Im}\{D_{dir}\} \, , \tag{4.10}$$

where E_{tot} and n_{tot} are, respectively, the total energy and the modal density of the SEA subsystem, D_{dir} is the direct field dynamic stiffness matrix that represents the load that the external fluid imposes on the structure at a given frequency, already projected in the structural degrees of freedom Shorter and Langley [2005a]. The direct field matrix is an alternative way to reference the radiation impedance matrix of the panel, for

each mode. The imaginary part of such a matrix, considered in Equation (4.10), is associated with the kinetic energy (mass loading) of the fluid movement in the vicinity of the structure. A quick way to calculate this matrix, according to Cordioli and Cotoni [2009], assumes that the face in contact with the fluid is flanged and radiates in an infinite hemispherical space, defined by a flat and rigid baffle.

Thus, for a better representation of the problem, the direct-field dynamic stiffness matrix already designed for the structural degrees of freedom D_{dir}, also influences the structural dynamic stiffness matrix of the FEM problem, resulting in

$$D_{tot} = \left[\; D_s + D_{dir} \; \right] \; , \tag{4.11}$$

where D_s is the modal dynamic stiffness presented in the left hand side of Equation (4.9) if considering mass normalized modes as degrees of freedom of the FE part. The total excitation of the FE plate will be given by the sum of the external load and the fluid's reverberant load, resulting in

$$S_{ff,tot} = S_{ff,ext} + S_{ff,rev} \; , \tag{4.12}$$

where $S_{ff,ext}$ is the initial structural excitation of the FE system. Finally, the random response of the global system will be obtained considering

$$S_{nn} = D_{tot}^{-1} \left[S_{ff,tot} \right] D_{tot}^{-H} \; , \tag{4.13}$$

where the index n denotes the degrees of freedom of the vibroacoustic problem.

4.2.4 Direct-field dynamic stiffness using wavelet functions

An approach for calculating the acoustic dynamic stiffness matrix of a baffled structure was introduced by Langley [2007], where a wavelet description of either the surface displacement or the surface pressure is derived. This study modifies Williams and Maynard (1982) formulation which presented the wavenumber representation of the radiated pressure in terms of spatial Fourier transforms on the surface degrees of freedom.

The wavelet formulation offers a numerically efficient alternative since it avoids the need to calculate the Fourier transform of the shape functions used to describe the

system. The dynamic stiffness matrix expressed in wavelet coordinates is given by

$$D_{mn} = \frac{1}{2\pi}\int_0^\infty G(k)|U(k)|^2\,\mathrm{J}_0(kr)k\,\mathrm{d}\,k, \quad r = |x_m - x_n|, \tag{4.14}$$

where $G(k)$ is the green function amplitude expressed in wavenumber domain, $U(k)$ is the amplitude of the wavelet function and J_0 is the Bessel function of zero order. Equation (4.14) considers the function radially symmetric which allows to reduce a two dimensional integral in wavenumber space to the presented 1D equation. The free-field Green function in wave number domain is given by Cremer et al. [2005]

$$G(k) = \frac{\mathrm{j}\,\omega\rho c k_a}{\sqrt{k_a^2 - k^2}}\ , \tag{4.15}$$

with k_a representing the acoustic wavenumber. The amplitude function $U(k)$ should be capable of representing shape functions which produce a smooth and accurate approximation to the displacement of the system. Langley [2007] proposed the use of jinc funtions which does not have sharp edges in space and can be simply formulated in wavenumber domain as

$$U(k) = \begin{cases} 0\,, & k > k_s \\ \frac{4\pi}{k_s^2}, & k \leq k_s \end{cases} \tag{4.16}$$

where $k_s = \sqrt{2}(\pi/dx)$, $d_x = dx_1 = dx_2$ for a regular mesh, is a convenient wave-number that corresponds to a half wavelength to be captured by the grid points based on the element length dx_1 of the surface mesh. It can be seen that $U(k)$ becomes zero for high values of k, which means that its representation in space domain $U(x)$ behaves like a delta function. The direct stiffness matrix integral presented in Equation 4.14 becomes finite in this context, given by

$$D_{mn}(r,\omega) = \frac{\mathrm{j}\,8\pi\omega\rho c k_a}{k_s^4}\int_0^{k_s}\frac{J_0(kr)k}{\sqrt{k_a^2 - k^2}}dk \tag{4.17}$$

By using this formulation, the dynamic stiffness matrix can be transformed into any set of generalized coordinates based on the mapping between the wavelets and the system displacement, including structural modes. The evaluation of this integral is problematic when $k \to k_0$, which induces a singularity. To avoid this problem, Equation (4.17) can be written as

$$D_{mn}(r,\omega) = \frac{\mathrm{j}\,8\pi\omega\rho c k_a}{k_s^4}\left(\int_0^{k_a}\frac{J_0(kr)k}{\sqrt{k_a^2 - k^2}}dk + \int_{k_a}^{k_s}\frac{J_0(kr)k}{\sqrt{k_a^2 - k^2}}dk\right)\ . \tag{4.18}$$

If assuming I_1 and I_2 the first and second integral terms in Equation (4.18), respectively, they can also be written as

$$I_1 = \int_0^{k_a} \frac{J_0\left(\frac{k}{k_a}k_a r\right) k/k_a}{\sqrt{1-\frac{k^2}{k_a^2}}} dk\,, \tag{4.19}$$

$$I_2 = \mathrm{j}\int_{k_a}^{k_s} \frac{J_0\left(\frac{k}{k_a}k_a r\right) k/k_a}{\sqrt{\frac{k^2}{k_a^2}+1}} dk \tag{4.20}$$

By assuming a variable changing $x = k/k_a$, the analytical solution of I_1 can be easily found Gradshteyn and Ryzhik [2000], given in total

$$I_1 = k_a\,\mathrm{sinc}\{k_a r\} = k_a\frac{\sin(k_a r)}{k_a r} \tag{4.21}$$

and I_2 will be equivalent to

$$I_2 = \mathrm{j}\,k_a\int_1^{k_s/k_a} \frac{J_0\left(x k_a r\right) x}{\sqrt{x^2+1}} dx = \mathrm{j}\,k_a\left(\int_1^{\infty} \frac{J_0\left(x k_a r\right) x}{\sqrt{x^2+1}} dx - \int_{k_s/k_a}^{\infty} \frac{J_0\left(x k_a r\right) x}{\sqrt{x^2+1}} dx\right)\,. \tag{4.22}$$

The analytical solution of the first integral on the right hand side of Equation (4.22) is $\cos(k_a r)/r$ Gradshteyn and Ryzhik [2000]. Additionally, it can be expected that $k_s >> k_a$ and $x >> 1$ in the integration range of the second integral. In this context, the ratio $x/\sqrt{x^2+1} \approx 1$ and I_2 can be given by

$$I2 = \mathrm{j}\,k_a\left[\frac{\cos(k_a r)}{k_a r} - \left(\int_0^{\infty} J_0\left(x k_a r\right) dx - \int_0^{k_s/k_a} J_0\left(x k_a r\right) dx\right)\right]\,. \tag{4.23}$$

The first integral term in Equation (4.23) has a well known solution being $1/(k_a r)$, resulting in

$$I2 = \mathrm{j}\,k_a\left(\frac{\cos(k_a r)}{k_a r} - \frac{1}{k_a r} + \int_0^{k_s/k_a} J_0\left(x k_a r\right) dx\right) = \mathrm{j}\,k_a\left(\frac{\cos(k_a r)-1}{k_a r} + \int_0^{k_s/k_a} J_0\left(x k_a r\right) dx\right)\,. \tag{4.24}$$

Finally, the direct field stiffness matrix will be simply given by a sum of I_1 and I_2 times the amplitude exposed in Equation (4.18), giving in total

$$D_{dir} = \mathrm{j}\,\frac{8\pi\omega\rho_0 c_0 k_a}{k_s^4}[I_1 + I_2]\,. \tag{4.25}$$

If expanding the term $\cos(k_a r)/(k_a r)$ in Laurent series, it can be observed

$$\frac{\cos(k_a r)}{k_a r} = \frac{1}{k_a r} - \frac{(k_a r)^2}{2} + \frac{(k_a r)^3}{24} - \frac{(k_a r)^5}{720} \dots \ . \tag{4.26}$$

when applying this series expansion in Equation 4.24, and taking into account that $\mathrm{sinc}(0) = 1$, the singularity for $r = 0$ will be canceled and Equation (4.25) becomes

$$D_{dir,(r=0)} = \mathrm{j}\,\frac{8\pi\omega\rho_0 c_0 k_a}{k_s^4}\left[k_a + \mathrm{j}\,k_a \int_0^{k_s/k_a} J_0\left(x k_a r\right) dx\right] \ . \tag{4.27}$$

Equation (4.25) and (4.27) bring the numerical advantage of computing the direct field matrix from just a single finite integral (I_2), avoiding the need of calculating a double integral in the space domain. The space domain approach will be discussed in Section 4.2.5.

Numerical validation and work contribution

A new tool was proposed in this research project for calculating the direct field matrix, in order to link with the Hybrid FE-SEA method. A mapped square mesh, composed by a grid of $N \times N$ samples was implemented over the structure surface to validate the proposed algorithm. Analytical modes were extracted by using the following relation Timoshenko et al. [1959]

$$\Phi_{nm}(x, y) = \sin(n\pi x/L) + \sin(m\pi y/L) \ , \tag{4.28}$$

$$k_{mn} = \frac{\pi}{L}\sqrt{(n^2 + m^2)} \tag{4.29}$$

with L representing the lateral dimension of the square plate, Φ_{nm} the mode shape and k_{nm} the propagating wavenumber of the (n, m) mode.

The validation was done in terms of the reactive and resistive parts of the radiation impedance Z_{dir}, which depends on the dynamic stiffness matrix folowing the relationship

$$Z_{dir,mn} = \frac{\Phi_{mn}^{\mathrm{T}} D_{dir} \Phi_{mn}}{\mathrm{j}\,\omega} \ , \tag{4.30}$$

where $\mathrm{j} = \sqrt{-1}$ is the complex and T the transpose operator. From the radiation impedance, it can be possible to extract the radiation efficiency σ_{rad} and the reactive

impedance κ of the square plate, given by Langley [2007]

$$\sigma_{rad} = \frac{4\,\mathrm{Re}(Z_{dir})}{\rho_0 c_0 L^2}\,, \tag{4.31}$$

$$\kappa_{rad} = \frac{4\,\mathrm{Im}(Z_{dir})}{\rho_0 c_0 L^2}\,. \tag{4.32}$$

Figure 4.4 compares the reactive impedance obtained in the validation step with a reference curve, while Figure 4.5 presents a comparison of the radiation efficiencies with data extracted from Langley [2007]. A grid was considered with $N = 20$, giving the total of 400 samples in the mesh. The number of integration points n_k is varying in 4, 8, 24, 32 to investigate the convergence of the developed numerical tool. Results are plotted in terms of the non-dimensional frequency represented by the ratio k_0/k_{mn}, where k_0 is the wavenumber in the air.

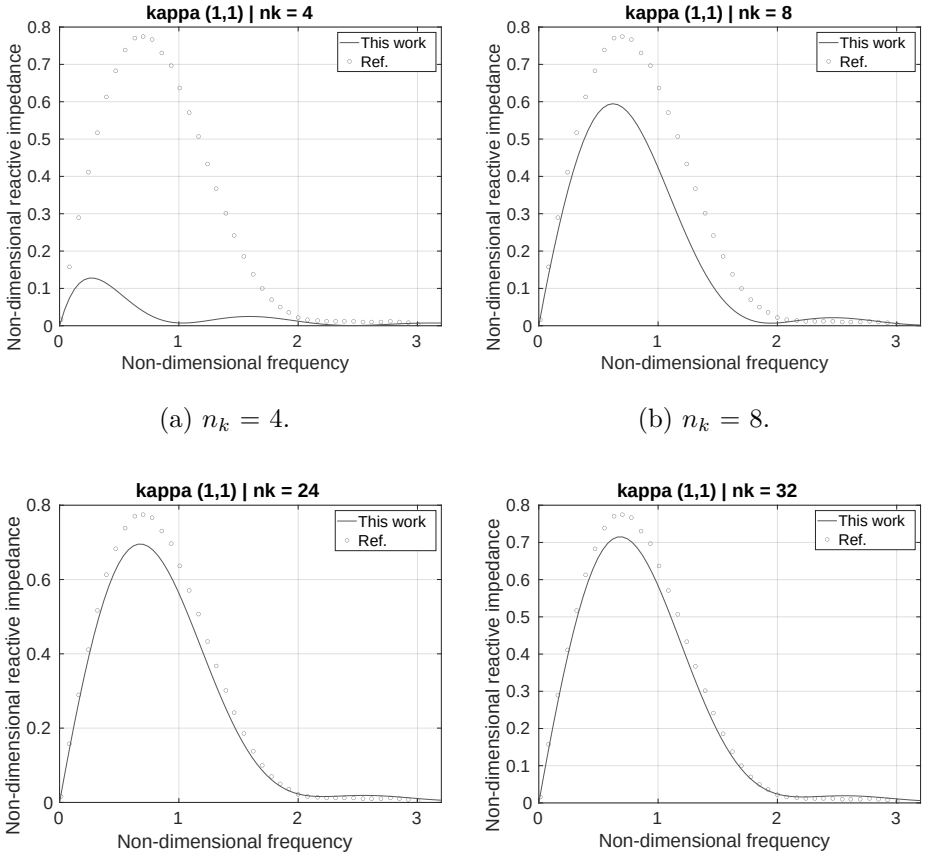

(a) $n_k = 4$.

(b) $n_k = 8$.

(c) $n_k = 24$.

(d) $n_k = 32$.

Figure 4.4: Reactive impedance of a simply supported plate considering the first analytical mode (1,1). Reference from Langley [2007].

It can be seen that σ_{rad} will depend on the real part of Z_{dir} and, consequently, the imaginary part of D_{dir}. Otherwise, κ_{rad} depends on the real part of D_{dir} wich is controlled by I_2 (see Equation (4.23)). It suggests that the numerical computation of κ is more complex than σ. Figure 4.4 shows that the real part of D_{dir}, which depends on the full wavenumber integration from 0 to k_s/k_a (see Equation (4.25)) presented a poor convergence with the reference for a small number of integration points, although the shape of the expected result arrives when the discretization increases. On the other hand, Figure 4.5 shows that the radiation efficiencies matched very well with the reference curve since it is not dependent of the integration points, but on the discretization (mesh) of the structure. It is expected, therefore, that the σ results converge for a single mesh.

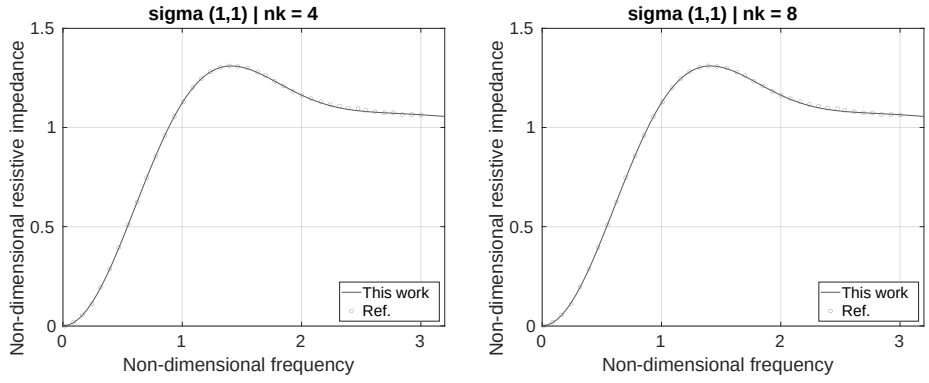

(a) $n_k = 4$.

(b) $n_k = 8$.

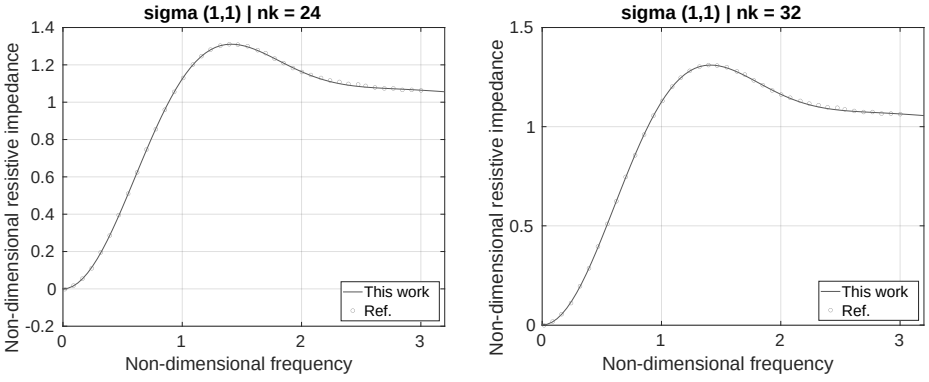

(c) $n_k = 24$.

(d) $n_k = 32$.

Figure 4.5: Resistive impedance of a simply supported plate considering the first analytical mode (1,1). Reference from Langley [2007].

The performance of the numerical methodology for the real part of D_{dir} has not

presented a good accuracy so far. The problems seen in Figure 4.4 for certain frequencies, mainly at the resonances which require an accurate sensitivity for computing the amplitude, can be related to a large integration interval. It was noticed that this lack of intervals was more important for very close points $k_a r \approx 0$ or when $x \approx 0$ (see Equation 4.23) .

Taking into account this behavior, a contribution of this work proposes a different strategy for computing the numerical integral. Instead of using a large number of integration points nk, the numerical integral was fragmented in a given number of small intervals. The integration region next to $x \approx 0$ was divided into a number n_i of small intervals, while a few intervals n_f were considered for the final region of integration.

The intervals of integration were implemented in terms of an initial length $d_i = 0.005$. It means that the n_i intervals chosen will be multiples of d_i. When n_i is reached, the remaining limits of integration are divided in n_f equally spaced intervals, since the final region is less sensitive to small variations. Figure 4.6 illustrates the numerical fragmentation of the integration limits. Figure 4.7 shows the non-dimensional reactive impedance calculated from this technique. In this simulation, $n_f = 2$ and $n_k = 8$ for the cases where intial intervals n_i is varying.

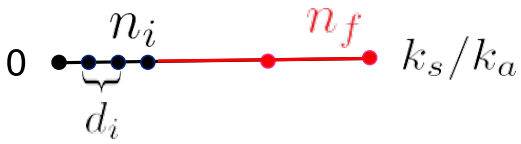

Figure 4.6: Integration limits for the numerical computation of the direct field matrix.

It can be noticed in Figure 4.7 that the proposed implementation reduces the dependency of a high number of Gauss points (n_k) and the technique provides a good convergence with the reference curve when a sufficient number of intervals n_i is used (Figure 4.7 (c)). The computational time of the best situation ($n_i = 6$) was considerably smaller than the time solution of the simulations presented in Figures 4.4 (c) and (d) with high number of gauss points n_k.

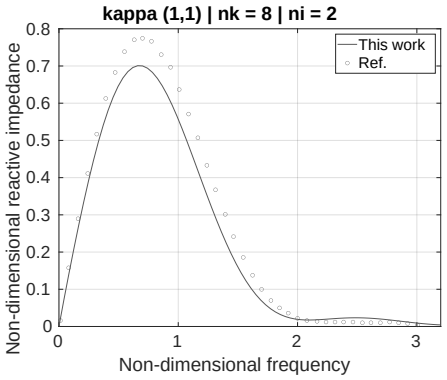

(a) $n_i = 2$.

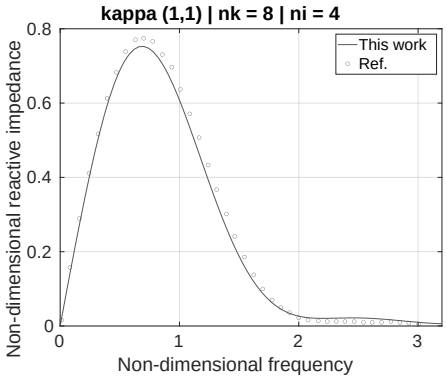

(b) $n_i = 4$.

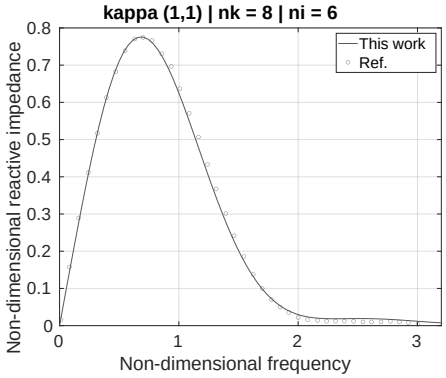

(c) $n_i = 6$.

Figure 4.7: Resistive impedance of a simply supported plate considering the first analytical mode (1,1). Reference from Langley [2007].

4.2.5 Direct-field dynamic stiffness using the space integration

As already mentioned in this section, acoustic spaces and solid plates are controlled by sound radiation, which is one of the most important phenomena on the fluid-structure coupling in vibroacoustics. The mathematical modeling of the sound radiation was introduced by Rayleigh [1896]. Lord Raleigh in his book "*Theory of Sound*" also presented his thinking about the reciprocity relationship of mathematical physics, which was not originated from him, but was explained in several forms empathizing that remarkable reciprocal relations exist between the forces and motions of different types in a linear problem Cook [1996]; Rayleigh [1896].

The Rayleigh's method was firstly developed for computing the sound propagation in semi-infinite medias. This methodology considers that the pressure field

generated by a vibrating structure is obtained by the superposition of the pressure at each element of the mesh by considering it as a monopole source. This formulation is widely used for many industrial applications nowadays. From the classical Hemholtz's equation Alia [2006], the sound pressure can be represented as

$$C(P)p(P) = -\int_S \mathrm{j}\,\rho\omega v_n G(r) + p\frac{\partial G(r)}{\partial n} dS \tag{4.33}$$

where $G(r) = \mathrm{e}^{-jkr}/(4\pi r)$ is the Green function propagating in free space, r is a distance between a given point P and the vibrating surface, v_n is the normal velocity, and $C(P)$ is a constant that depends on the boundary conditions. Figure 4.8 illustrates a sound source P and its image-source impinging at a vibrating surface S that coincides with a perfectly reflecting surface S_R (rigid baffle).

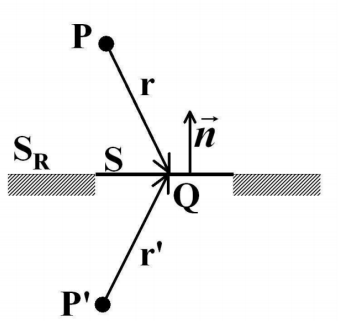

Figure 4.8: Illustration of the sound propagation in a semi-infinite medium Alia [2006].

The Green function of a semi-infinite domain, denoted as the distance between a point at the surface and the point P into the acoustic fluid, is given by the summation of the fundamental kernels and its image-source. As the distances are equal $r = r'$ and $\frac{\partial r}{\partial n} = -\frac{\partial r'}{\partial n}$, it can be proved that

$$G(r) + G(r') = 2G(r)\ ; \frac{\partial G(r)}{\partial n} + \frac{\partial G(r')}{\partial n} = 0, \tag{4.34}$$

and knowing that $C(P) = 1$ for this case Alia [2006], Equation 4.33 can be writen as

$$p(P) = -\int_S \mathrm{j}\,\omega\rho v_n \frac{\mathrm{e}^{-jkr}}{2\pi r}\,\mathrm{d}\,S\ . \tag{4.35}$$

If considering a planar structure described by its modal displacement $\Phi_n(x)$, knowing

that $\Phi_n(v_n) = \mathrm{j}\,\omega\Phi_n(x)$, the pressure response at a point x will be given as

$$p(x) = \frac{-\omega^2\rho}{2\pi}\int_s \frac{\Phi_n(x')\exp(-\mathrm{j}\,kr)}{r}\,\mathrm{d}\,x, \quad r = |x - x'| \tag{4.36}$$

The blocked force on the nth mode due to a unit displacement of the mth mode in matrix form is

$$\begin{aligned} D_{mn} &= \int_{s'} \Phi_m(x)p(x)dx \\ &= \frac{-\omega^2\rho}{2\pi}\int_{s'}\int_s \frac{\exp(-\mathrm{j}\,kr)}{r}\Phi_m(x)\Phi_n(x')\,\mathrm{d}\,x\,\mathrm{d}\,x' \end{aligned} \tag{4.37}$$

where D_{mn} represents the mnth entry of the direct field dynamic matrix D_{dir} of a baffled radiating plate.

Equation 4.37 was also numerically implemented in this study.

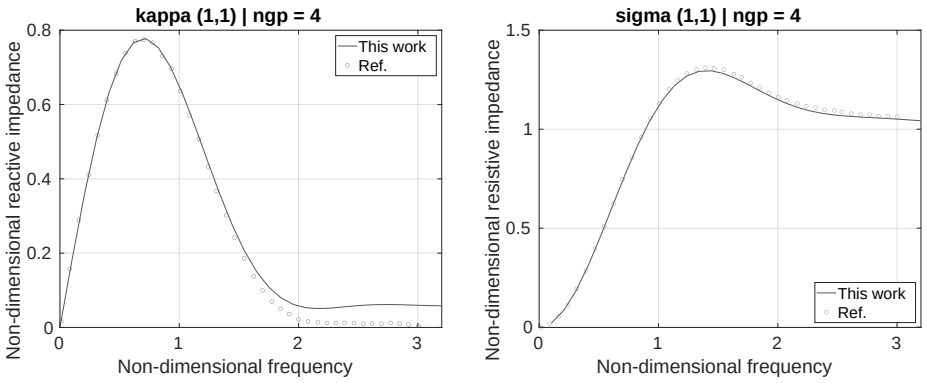

(a) (b)

Figure 4.9: (a) Reactive and (b) resistive impedances of a simply supported plate considering the first analytical mode (1,1) and space integration using 4 integration points. Reference from Langley [2007].

4.2.6 The Hybrid FE-SEA step-by-step

Section 4.2.3 brought a general idea of the Hybrid FE-SEA method. It is worthwhile to bring a more detailed theory on this topic, which will be given in the form of a step-by-step. Lets keep in mind the problem presented in Figure 4.3, which considers a FE plate coupled to an acoustic cavity.

4.2.6.1 Meshing

In this work, the degrees of freedom are extracted from the finite element modes of deterministic subsystems, and from the energy of statistical subsystems. In the finite element part, undamped and uncoupled modes are considered for each subsystem, as presented in Section 4.2. The importance of meshing becomes from the desired number of modes that should be included in the analysis. If the mesh is too coarse, the available number of degrees of freedom can not to be enough to capture high order modes.

As already mentioned, the finite element mesh will also affect the choice of a convenient wavenumber k_s to compute the dynamic stiffness matrix using the wavelet approach, which depends on the element size.

4.2.6.2 Input power from the direct field

Power is defined as the time averaged product of a force and the in-phase component velocity of in the direction of the force Hambric [1990]. In terms of amplitudes, the average power is given as

$$P = \frac{1}{2}\,\mathrm{Re}\{v^* F\}\,, \tag{4.38}$$

where Re v^* is the complex conjugate of the velocity and F is the force component of a given elementary source. Into the direct field, Equation (4.38) can be re-written as Shorter and Langley [2005a]

$$P_{dir} = \frac{1}{2}\,\mathrm{Re}\{(\mathrm{j}\,\omega\mathbf{q})^H D_{dir}\mathbf{q}\}\,, \tag{4.39}$$

with $\mathbf{q}$ being the displacement degrees of freedom of the structure, Re is the real part indicator, and H is the Hermitian operator. It can be noted that the term $((\mathrm{j}\,\omega\mathbf{q})^H)$ is equivalent to the complex conjugate of the velocity and, since D_{dir} is a stiffness matrix given in Newtons by meter. It means that the second term $D_{dir}\mathbf{q}$ results on a force.

Elliott and Johnson [1993] presented an alternative for computing the radiation modes, which can be used to describe the sound radiation in terms of a set of velocity degrees of freedom on the structure whose sound power radiation is independent of the amplitudes of the other velocity distributions. So the direct field radiation components can be found by solving the following eigenvalue problem

$$\begin{aligned} M\Pi &= \Omega\Pi \\ M &= \Pi^T\Omega\Pi \end{aligned} \tag{4.40}$$

where Π is an ortogonal matrix of eigenvectors and Ω is a diagonal matrix of eigenvalues of the structural radiation resistance M. The acoustic power can thus be written as

$$P = \mathbf{q}^{\mathrm{H}} M \mathbf{q} = \mathbf{q}^{\mathrm{H}} \Pi^{T} \Omega \Pi \mathbf{q}. \tag{4.41}$$

When defining a vector of transformed radiation mode amplitudes $\mathbf{b} = \Pi\mathbf{q}$, Equation 4.41 becomes

$$P = \mathbf{b}^{\mathrm{H}} \Omega \mathbf{b} = \sum_{n=1}^{N} \Omega_j |\mathbf{b}_j|^2 \,, \tag{4.42}$$

where j is the mode indicator, N the total number of modes, and the later expression is a consequence of Ω being diagonal. In the direct field, the right side of Equation 4.42, Ω_j will be given in terms of the imaginary part of $D_{dir,jk}$, which represents the modal radiation resistance matrix. The square module of the degrees of freedom $|\mathbf{b}_j|^2$ can be taken from the power spectral density of the random response, which is presented in Equation (4.13). The total power from the direct field to a statistical susbsystem is given by Shorter and Langley [2005b]

$$P_{in}^{dir} = \frac{\omega}{2} \sum_{jk} \mathrm{Im}\{D_{dir,jk}\} \left(D_{tot}^{-1} \, S_{FF}^{tot} \, D_{tot}^{-H} \right) \tag{4.43}$$

Equation (4.12) in (4.43) results in

$$P_{in}^{dir} = \frac{\omega}{2} \sum_{jk} \mathrm{Im}\{D_{dir,jk}\} \left(D_{tot}^{-1} \left(S_{FF}^{ext} + S_{FF}^{rev} \right) D_{tot}^{-H} \right) \,. \tag{4.44}$$

Equation (4.44) demonstrates that the SEA input power will depend on the external power on the FE subsystem and the blocked force from the reverberant part concentrated on the surface of the hybrid junction. The reverberant part of the power spectral density, which is the excitation from the statistical part at the deterministic surface, can be written in terms of its energy (see Equation (4.10)), giving in total

$$P_{in}^{dir} = P_{in,0} + \frac{\omega}{2} \sum_{jk} \mathrm{Im}\{D_{dir,jk}\} \left(D_{tot}^{-1} \, \mathrm{Im}\{D_{dir,jk}\} \, D_{tot}^{-H} \right) \left(\frac{4E_{(m)}}{\omega \pi n_{(m)}} \right) \,, \tag{4.45}$$

$$P_{in,0} = \frac{\omega}{2} \sum_{jk} \mathrm{Im}\{D_{dir,jk}\} \left(D_{tot}^{-1} \, S_{FF}^{ext} \, D_{tot}^{-H} \right) \,, \tag{4.46}$$

which results in

$$P_{in}^{dir} = P_{in,0} + \frac{2}{\pi} \sum_{jk} \mathrm{Im}\{D_{dir,jk}\} \left(D_{tot}^{-1} \, \mathrm{Im}\{D_{dir,jk}\} \, D_{tot}^{-H} \right) \left(\frac{E_{(m)}}{n_{(m)}} \right) . \tag{4.47}$$

where the index m represents the statistical subsystem in the hybrid connection. If considering $h_{nm} = \mathrm{Im}\{D_{dir,jk}\} \left(D_{tot}^{-1} \, \mathrm{Im}\{D_{dir,jk}\} \, D_{tot}^{-H} \right)$, Equation (4.47) becomes

$$P_{in}^{dir} = P_{in,0} + \frac{2}{\pi} \sum_{jk} h_{nm} \left(\frac{E_{(m)}}{n_{(m)}} \right) . \tag{4.48}$$

The coefficient h_{nm} is a hybrid coupling loss factor which gives the ensemble average input power to the direct field of the mth subsystem per unit modal energy density in the reverberant field of the nth subsystem Shorter and Langley [2005b].

4.2.6.3 Output power from the reverberant field

The output power leaving the statistical subsystem P_{out}^{rev} (see Figure 4.3) is given by

$$P_{out}^{rev} = \frac{\omega}{2} \sum_{jk} \mathrm{Im}\{D_{tot,jk}\} \left(D_{tot}^{-1} \, S_{FF}^{rev} \, D_{tot}^{-H} \right) \tag{4.49}$$

By comparison with Equation (4.43), it can be noted that when power is imposed on the deterministic system from the statistical one, the radiation resistance will depend on both the direct field matrix and the dynamic stiffness matrix of the finite element problem represented by $\mathrm{Im}\{D_{tot}\}$, but only the statistical excitation coming from the reverberant field (S_{FF}^{rev}) will have influence to the output power. If considering the reverberant excitation in terms of the subsystem energy, Equation (4.49) becomes

$$P_{out}^{rev} = \frac{2}{\pi} \sum_{jk} \mathrm{Im}\{D_{tot,jk}\} \left(D_{tot}^{-1} \, \mathrm{Im}\{D_{dir,jk}\} \, D_{tot}^{-H} \right) \left(\frac{E_{(m)}^{tot}}{n_{(m)}^{tot}} \right) . \tag{4.50}$$

If a similar procedure exposed in Section 4.2.6.2 is adopted, a new hybrid coefficient $h_{tot} = \mathrm{Im}\{D_{tot,jk}\} \left(D_{tot}^{-1} \, \mathrm{Im}\{D_{dir,jk}\} \, D_{tot}^{-H} \right)$ can be introduced, and Equation (4.50) becomes

$$P_{out}^{rev} = \frac{2}{\pi} \sum_{jk} h_{tot,m} \left(\frac{E_{(m)}^{tot}}{n_{(m)}^{tot}} \right) . \tag{4.51}$$

The coefficient $h_{tot,m}$ represents a hybrid loss factor related to the energy leaving per unit modal energy density in the mth reverberant field.

4.2.6.4 Dissipation power and SEA matrix

Classically, the dissipation of the average power within a statistical subsystem is controlled by a loss factor, as already mentioned in Chapter 3. The dissipated power of the mth subsystem will be given by

$$P_{diss,n} = \omega \eta_m E_m = M_m \frac{E_m}{n_m} \,, \tag{4.52}$$

where $M_m = \omega n_m \eta_m$ is the modal overlap of the mth statistical subsystem.

The power balance equations for the statistical systems of the hybrid method will depend on the input and output powers of each subsystem, which are, the input powers from the external load and direct field, and the output power leaving the reverberant field as well as the dissipated power, then,

$$P_{in}^{dir} = P_{out,rev} + P_{diss,n} \,, \tag{4.53}$$

which is

$$P_{in,0} = P_{out,rev} + P_{diss,n} - P_{in,rev} = M_m + h_{tot,m} \frac{E_m}{n_m} - \sum_n h_{nm} \frac{E_m}{n_m} \,. \tag{4.54}$$

where $P_{in,rev}$ represents the reverberant input power to the direct field composed by the second term of the right-hand side of Equation (4.48). In matrix form

$$\begin{bmatrix} M_1 + h_{tot,1} - \sum_{n \neq 1} h_{n1} & \dots & -h_{1m} \\ \vdots & \ddots & \vdots \\ -h_{m1} & \dots & M_m + h_{tot,m} + \sum_{n \neq 1} h_{mm} \end{bmatrix} \begin{Bmatrix} \frac{E_1}{n_1} \\ \vdots \\ \frac{E_m}{n_m} \end{Bmatrix} = \begin{Bmatrix} P_{in,0}^{(1)} \\ \vdots \\ P_{in,0}^{(m)} \end{Bmatrix} \tag{4.55}$$

which is the SEA matrix of the statistical part of the hybrid FE-SEA system.

4.2.7 FEM and SEA subsystems

The presented formulations of the dynamic stiffness matrix was applied in a FE plate-SEA cavity system for evaluating the solution efficiency of an in-house code concerning the hybrid FE-SEA method. A simply supported aluminum plate with surface area $S = 1$ m^2 and thickness $h = 1$ mm was proposed in this study. A structural mesh consisting of 400 elements was created. This simple mesh was selected as a reference to the numerical implementation considering that the goal of this simulation is the

comparison between two techniques, which means that the absolute value of velocity is not important at this point. A point force was applied on node 20 next to the boundary. The structural response was collected in the middle of the system. Figure 4.10 shows the structural FE model considered in the simulation.

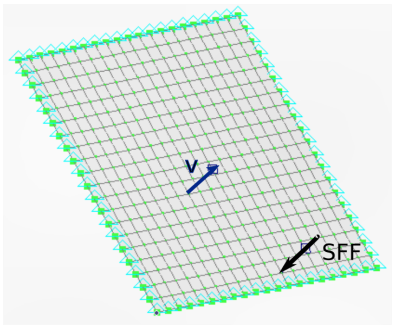

Figure 4.10: FE model with x quadrilateral elements.

The modal analysis considered X bending modes covering a range of frequencies from 100 Hz to 500 Hz. The structural loss factor was considered 1%. This modal damping parameter is applied on the FE structure as a complex proportional stiffness, acting at the resonances of the modal solution.

The proposed SEA cavity consists of a cube with 1 m^3 volume as illustrated in Figure 4.11. The acoustic loss factor into the cavity was considered 1% and it is used to calculate the mean energy by solving the SEA linear system.

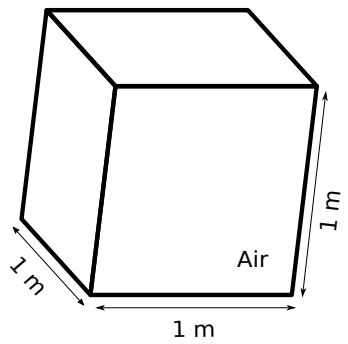

Figure 4.11: SEA cavity coupled to the hybrid model.

The cavity was considered a passive system, which means that the acoustic power into the subsystem was applied from the FE plate. Coupling factors were calculated by following the guidelines of the Hybrid FE-SEA method Shorter and Langley [2005b].

4.2.8 Case of a SEA cavity coupled to FE

Analysis in this report was done by using a frequency resolution of 5 Hz, but the curves should be improved in next steps. In order to validate the numerical approaches of the dynamic stiffness matrix, the radiation efficiency of the plate/fuid junction is presented in Figure 4.12. The Leppington's model Leppington et al. [1982], a classical formulation for radiation of flat structures used in full-SEA applications is also presented for comparison.

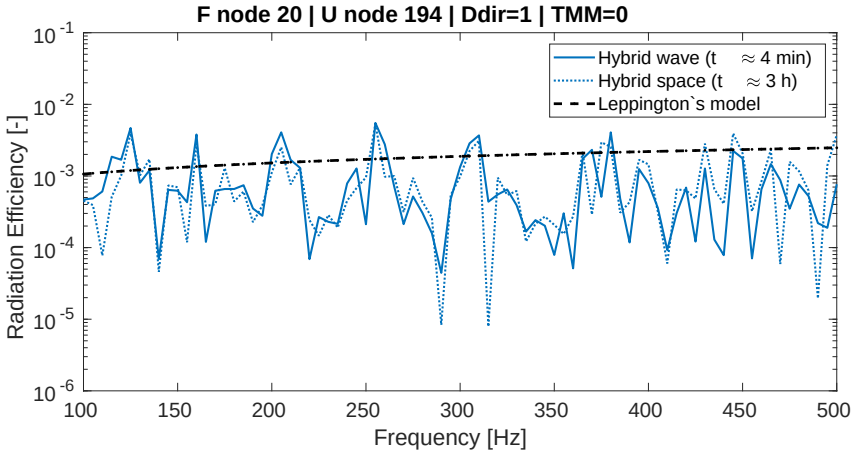

Figure 4.12: Radiation efficiency of the hybrid system.

Figure 4.12 shows slight difference between space and wavenumber domain radiation efficiency, although the time of processing the wave method was considerably small. It can be seen that the hybrid method is capable to capture the modal tendencies of the radiation efficiency which is important when the spectral regions with small modal densities. For this reason, Leppington's model cannot represent well the radiation in low/mid frequencies, but the curve becomes more relevant in high modal density spectral regions, where the full-SEA method is well established.

Figure 4.13 plots the RMS velocity calculated at node 194 of the FE plate before and after applying the SEA cavity. A full-SEA simulation is also presented, which is both systems represented by SEA subsystems, although this result is not local but a mean RMS velocity of the full subsystem.

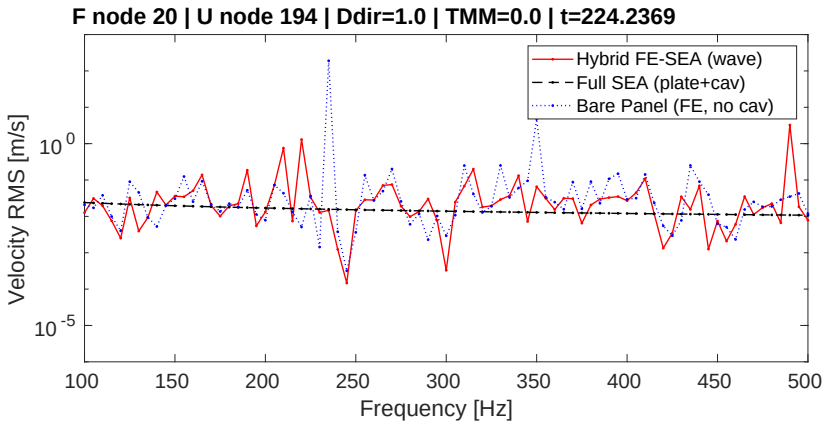

Figure 4.13: Plate RMS velocity.

It is possible to notice in Figure 4.13 the resistive and reactive effects of the dynamic stiffness matrix acting in the system employing the addition of damping (real part of D_{dir}) and shifting some resonance frequencies (imaginary part of D_{dir}). It can be seen that there are some modes where the velocity amplitude increases substantially (see $\approx$ 200 Hz), which means that its radiation capacity is high. It is also noticed that the mode around 250 Hz was completely canceled in presence of the cavity, which can be explained by the poor radiation efficiency in this frequency region (see also Figure 4.13).

Some energy parameters from the SEA simulation were also calculated. Figure 4.14 shows the input power from the FE plate to the cavity as well as the sound pressure level generated by the structural excitation into the SEA acoustic subsystem.

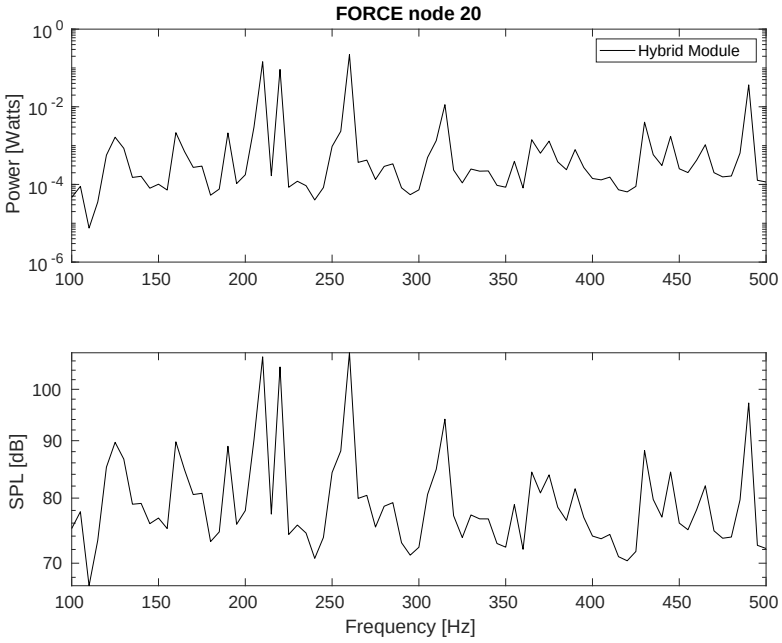

Figure 4.14: Mean quantities from the cavity.

As expected, Figure 4.14 shows the input power proportional to the pressure into the acoustic space. The magnitude of the sound pressure level represents the energetic level of a diffuse acoustic field in contact with the plate, which is a very useful application in the hybrid FE-SEA approach since this kind of excitation is very difficult or computationally expensive to implement in classical deterministic methods as FEM and BEM simulations. These results can be compared with the full-FE cavity mean parameters in future works.

4.3 Hybrid FE-TMM

Noise control in large spectral ranges is necessary for many situations. In the aerospace industry, structural vibration and high acoustic loads can damage sensitive components of the space rocket. In automotive and aeronautics, it is desirable a comfortable environment for the passengers into the vehicles. In this context, passive techniques are well established in the industrial sector for sound and vibration control employing multi-layer treatments, which can dissipate the energy and provide the impedance changing that difficult the wave propagation.

At low and mid frequencies, porous media in multi-layer configurations are clas-

sically modeled using finite elements (FE). In this context, many approaches can be highlighted from simple equivalent fluid elements to more complex models as Biot theory-based calculations Allard and Atalla [2009]. However, while well established, these latter approaches have the disadvantage of high computational cost for high discretized models and large spectral range analyses. These formulations are mainly based either on the classical displacement Kang and Bolton [1995] of Biot's poroelasticity equations or the mixed displacement–pressure equations Atalla et al. [1998] where six degrees of freedom per node are demanded.

An alternative to the full-FE modeling is the Transfer Matrix Method (TMM) Allard and Atalla [2009]; Brouard et al. [1995], which accounts for wave propagation in infinitely extended multilayered systems. Although the formulation was developed for flat configurations, the approach is also used to model curved systems such as aerospace or aircraft structures. Moreover, new studies have been also made to couple a FE model for the bare structure and a TMM for the sound package.

Tournour et al. [2007] presented a quick procedure to account the effects of acoustic trim modeling using transfer admittance and finite element method. In this study, the transfer matrix was used to compute the admittance parameter which was applied in the FE dynamic stiffness equation. The method considers a fixed propagating wavenumber into the multilayer for the full structure domain characterizing a locally reacting treatment modeling approach.

In 2010, Courtois et al. [2010] evaluated the admitance method for a plate-cavity system by comparing with experimental data. The presented model was able to represent well the effect of the trim on vibration of the panel and sound pressure of the cavity, although it was presented a tendency to over-estimate damping effects. In terms of computational cost, the time of solution reached one order of magnitude faster than poroelastic finite elements.

Rhazi and Atalla [2010] proposed a modal method for computing the transfer function of the NCT attached to a given bare panel. In this approach, the vibration modes of the bare structure was considered in the transfer matrix by means of a modal wavenumber. This study comprised analytical modes of the structure and numerical FE was not applied.

Alimonti [2014] suggested a new method based on wavenumber integration of Green functions obtained from the TMM approach, using a similar technique proposed by Langley [2007] for computing the acoustic direct field matrix of a radiating plate. The main advantage of this proposition in comparison to that one proposed in reference

Courtois et al. [2010] is the possibility of varying the propagation wavenumber into the treatment, which can provide a better approximation of non-locally reactive samples.

This work presents the implementation of the hybrid FE-TMM method for the FE-structure coupled to a quick noise control treatment formulation for porous media using transfer matrices. The aim of this paper is twofold: to provide a consistent review of the available methods in literature as well as evaluating the numerical capabilities of these approaches for efficient prediction of vibroacoustic indicators of multilayered systems over a large range of frequencies.

4.3.1 Fundamentals

As already mentioned in Section 4.3, many approaches have been developed in the last years to improve the capabilities of the FE-TMM method. The main idea of this tool is to apply the treatment sample represented by its stiffness matrix, which is calculated from simple linear system solutions. Figure 4.15 illustrates an FE-plate trimmed by a noise control treatment sample.

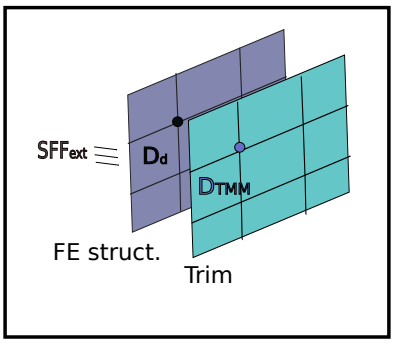

Figure 4.15: FE-TMM illustration.

Figure 4.15 shows the bare panel represented by its dynamic stiffness matrix D_d and the noise control treatment expressed by D_{TMM}. If the structural degrees of freedom of this system are undamped modes of the structure, D_d is computed from

$$D_d = -\omega^2[\Psi]^T[M][\Psi] + [\Psi]^T[K][\Psi] \,, \tag{4.56}$$

where Ψ are the structural modes, $[M]$ is the mass matrix and $[K]$ is the stiffness matrix of the FE structure. If Ψ is a matrix containing mass normalized eigenvectors,

Equation (4.57) can be written as

$$D_d = -\omega^2[\mathrm{I}] + [\omega_m]^2 \ , \tag{4.57}$$

where $[\omega_m]^2$ is a diagonal matrix of squared modal frequencies or the eigenvalues of the modal solution.

The full model presented in Figure 4.15 will be characterized by an equivalent dynamic stiffness calculated from the sum $D_{eq} = D_d + D_{TMM}$. For computing D_{TMM}, an appropriate integration should be implemented in order to distribute the impedance conditions over the entire structural domain. In the TMM analysis Allard and Atalla [2009], the propagation equations are written in terms of a set of matrices in accordance with the involved physics for each layer. The matrices are assembled to produce a response of the multi-layer treatment leading the following relation

$$\left\{ \begin{array}{c} p_2 \\ v_2 \end{array} \right\} = \left[\begin{array}{cc} T_{11} & T_{12} \\ T_{21} & T_{22} \end{array} \right] \left\{ \begin{array}{c} p_1 \\ v_1 \end{array} \right\} \tag{4.58}$$

where p_1 and p_2 are the pressures, v_1 and v_2 are the velocities at the beginning and the final point of the treatment, respectively. The components of matrix T are equivalent transfer functions that correlates pressure and velocity at the two extremities of the trim.

The equivalent transfer matrix can be interpreted as Green functions that characterize the wave propagation between two points. This system will be able to represent the condition at the opposite surface in contact with the bare panel, which configures the dynamic stiffness allocated at the FE nodes. From the resolution of the linear system exposed in Equation (4.58), it is possible to calculate a green function g_{11} as

$$g_{11} = \mathrm{j}\,\omega Z_s(\omega) = \mathrm{j}\,\omega \frac{p_1}{v_1} \ , \tag{4.59}$$

where Z_s is the surface impedance of the multilayer to be applied at the structural FE model surface. A more general result is given in Ref. Alimonti and Atalla [2016] as

$$g_{11}(k, \omega) = \mathrm{j}\,\omega \frac{T_{11}}{T_{22}} \ , \tag{4.60}$$

where, in this case, just the assembling of the global matrix is necessary. If there are fluid elements and FE vibroacoustic coupling, two more green functions can be calculate from matrix $[T]$ fo applying in acoustic degrees of freedom and FE coupling

terms. However, these Green functions need to be integrated over the surface of the base structure. In this context, three methods can be highlighted: the locally reactive, the modal FE/TMM and the non-locally reactive formulation. These methods are presented in the following sections.

4.3.2 Locally reacting FE/TMM

The simplest method considers a fixed propagation wavenumber for each frequency of analysis, which means that th Green function is assumed to vary slowly over the wavenumber spectrum, characterizing the locally reacting FE/TMM. If considering the incidence from the FE vibrating plate, the bending wavenumber of the structure can characterize the trace wavenumber of the incident wave in contact with the first layer of the treatment given by

$$k_b = \left(\frac{\omega^2 \rho_s h}{B} \right)^{0.25} \tag{4.61}$$

where ρ_s is the structural density, h is the thickness of the bare plate, $B = Eh^3/(12(1-\nu^2))$ is the bending stiffness of the structure that depends on the Young's modulus E and the Poisson's ratio ν. The longitudinal propagating wavenumber into the layer n of the noise control treatment will be

$$k_x = \sqrt{k_n^2 - k_b^2}\,, \tag{4.62}$$

where k_n is the wavenumber which characterizes the layer propagation. If it is a fibrous material, k_n is generally a complex number obtained from classical models of equivalent fluids. The consideration of k_x in the transfer matrices will make possible the simulation of the normal components at the surface of the multilayer setup.

As the wavenumber k_x is fixed, $g_{11}(k, \omega)$ is space independent and the distribution of this variable will be given by a simple element integration over the surface S. If the plate are represented by its modes $\Psi_i(x)$, the modal dynamic stiffness will be

$$D_{TMM}(\omega) = g_{11}(\omega) \int_S |\Psi_i(x)|^2 \, \mathrm{d}\, S$$

Equation (4.63) presents a simple and efficient way to consider the response of the multilayer in Finite Element simulations. A mass correction can be also implemented to the equivalent system. The calculation of $g_{11}(\omega)$ and the integration can be done separately.

4.3.3 Modal FE/TMM

An alternative formulation considers the modal wavenumber k_m in the solution of the characteristic green function. This parameter can be easily found from the eigenvalue solution of the modal system as following

$$k_m = \frac{\sqrt{\lambda_m}}{c_b} = \frac{\omega_m}{c_b} \tag{4.63}$$

where λ_m are the eigenvalues from the modal solution and $c_b = \omega/k_b$ is the bending propagation velocity.

When assuming that the modal coupling is zero, which is $D_{TMM}(\Psi_n, \Psi_m, \omega) = 0$ if $n \neq m$, the modal stiffness matrix of the treatment becomes diagonal and it represents a boundary impedance on the structural surface given by

$$D_{TMM}(\Psi_m, \omega) = g_{TMM}(\omega, k_m) \int_S |\Psi_m(x)|^2 \, \mathrm{d}\, S$$

where $g_{TMM}(\omega, k_m)$ is the green function extracted from the global transfer matrix of the noise control treatment when applying $k_x = \sqrt{k_a^2 - k_m^2}$ for the wave propagation analysis.

4.3.4 Non-locally reacting FE/TMM

A new approach proposed by Alimonti and Atalla [2016] considers the variation of the propagating wavenumber into the noise control treatment. The author suggests implementing a grid of wavenumber which depends on the finite element discretization. If using degrees of freedom represented by generic wavelet functions, as already approached in Section 4.2.4, the n, m component of the dynamic stiffness matrix of the noise control treatment D_{TMM} is given by a full integration in the k_x, k_y space, which is

$$D_{TMM}(\Phi_n, \Phi_m, \omega) = \frac{1}{(2\pi)^2} \int_{Sk} \Phi_m^*(k) g_{TMM}(\omega, k) \Phi_n(k) \, \mathrm{d}\, Sk \;, \tag{4.64}$$

where $[]^*$ indicates the complex conjugate of a function, S_k is the bi-dimensional wavenumber space (k_x, k_y). The functions $\Phi(k)$ are the Fourier transforms of the structural or cavity modes over the FE surface. Equation (4.64) shows that a discrete set of traveling waves gives the response of the base system as a consequence of the presence of lateral boundaries, the modes of the finite size acoustic treatment. On the other hand, the response of the infinite acoustic treatment is given by a distribution

of waves that propagate continuously, which means that all the wavenumber domain $(k_x; k_y)$ can propagate through the thickness.

If using radially symmetric shape functions, as the wavelet functions presented in Section 4.2.4, Equation (4.64) is reduced to a 1D integration for a given distance r_{ij} between two points in a grid, which means that

$$D_{TMM}(r,\omega) = \frac{1}{2\pi}\int_0^{k_s} g_{TMM}(r,k)|U(k)|^2\,\mathrm{J}_0(kr)kdk$$

being $k_s = \sqrt{2}(\pi/dx_1)$ a convenient wavenumber that corresponds to a half wavelength to be captured by the grid points based on the element length dx_1 of the finite element mesh, J_0 is the first order Bessel function, and $U(k)$ is the amplitude of generalized shape functions proposed by Langley [2007] as

$$U(k) = \begin{cases} 0\,, & k > k_s \\ \frac{4\pi}{k_s^2}, & k \leq k_s\,. \end{cases} \tag{4.65}$$

The Green functions g_{TMM} will be taken from the evaluation of the global transfer matrix (see Chapter 2) for a 1D dicrete grid of k from 0 to k_s, where the propagating wavenumber inside the treatment is computed as

$$k_x = \sqrt{k_a^2 - k^2}\,. \tag{4.66}$$

4.3.5 Analysis and discussion

A baseline fiber of 50 mm was considered for preliminary analysis in applying the methods exposed in Sections 4.3.2 to 4.3.4. The exercise considers a limp model, with sample's apparent density equal to 16kg/m^3. Macroscopic properties of the equivalent fluid are given in Table 4.1.

Table 4.1: Properties of a baseline fiber.

	σ [kN/m^4]	ϕ [-]	α_∞ [-]	Λ [μm]	Λ' [μm]
Fiber 16 [kg/m^3]	9.0	0.99	1.0	192	384

This fiber was coupled to the FEM deterministic system characterized in Section 4.2.7. In this section, however, the coupling with the considered NCT is evaluated

and no longer with the SEA cavity investigated in the previous section. Figures 4.16, 4.17, and 4.18 show the velocity response in the FEM plate before and after treatment coupling, considering the locally reactive, modal, and non-locally reactive models, respectively.

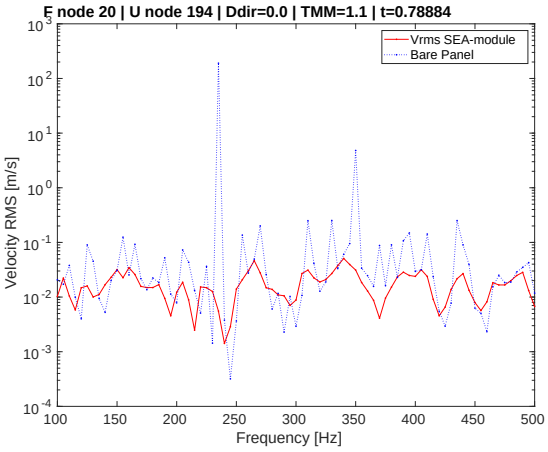

Figure 4.16: Point velocity for the plate-TMM configuration using the locally reactive method.

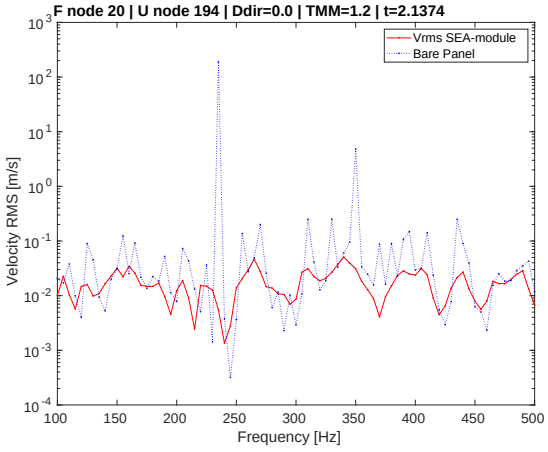

Figure 4.17: Point velocity for the plate-TMM configuration using the modal method.

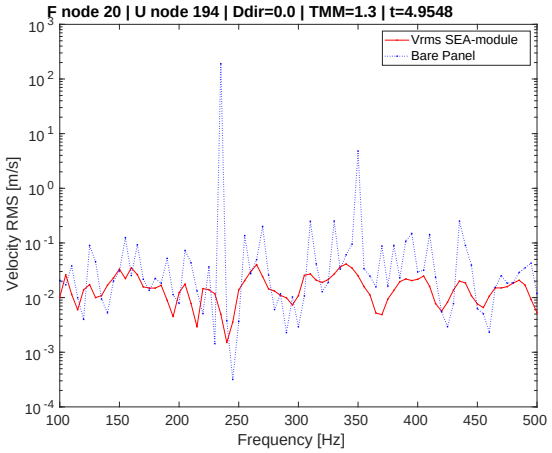

Figure 4.18: Point velocity for the plate-TMM configuration using the non-locally reactive method.

One can notice that the models captured the damping addition to the plate response commanded by the imaginary part of the dynamic stiffness matrix calculated from the transfer matrices method and slightly altered the peak frequencies due to its real part. Figures 4.16 to 4.18 also shows that the responses for the different methods were similar in this configuration, although the solution times varied significantly between the methods. Table 4.2 shows the running time of the simulation in seconds for each case.

Table 4.2: Mean time of the runs.

	LR FE-TMM	Modal FE-TMM	NLR FE-TMM
Mean CPU Time	0.79 s	2.13 s	4.95 s

Even so, any alternative demonstrated good computational efficiency regarding solution time. The difference is due to the number of Green's functions needed to calculate the dynamic matrix D_{TMM} for each approach.

Conclusions and perspectives

This thesis aimed to create essential tools for the continuity of studies focused on vibroacoustics and noise control. In this context, the work proposed here can contemplate a wide range of methods used in the academic and industrial sectors regarding effective alternatives of hybrid simulations for mid and high frequencies.

The inverse characterization of porous materials based on classical models and the experimental sound absorption coefficient was investigated, proving to be an effective alternative to be used with methods with less rigor in details, such as statistical energy analysis and transfer matrices.

A new implementation of the transfer matrix method (TMM) was proposed and studied regarding modeling noise control treatments in multilayer configurations. In this phase, the inclusion of solid, poroelastic layers, and porous materials as equivalent fluids was considered. The implemented methodology allowed the extraction of three distinct responses from a multilayer model: the sound absorption coefficient, the sound insertion loss, and the structural loss factor of the treatment.

An analysis of finite-size samples using the transfer matrix method was also discussed to obtain the sound absorption coefficient in reverberant environments under diffuse field applications for single and multilayer systems. Validation with experimental reference data was performed for single-layer samples of different thicknesses. The developed tool demonstrated advantageous computational efficiency compared to other references on the subject. However, the results differed from the experimental results when considering multilayer setups in combination with an air gap.

The transfer matrix method was incorporated into SEA-Module, an in-house tool in statistical energy analysis (SEA). When coupled to the SEA system in an area connection (plate+cavity), the noise control treatment applies a sound insertion loss to the junction coupling factors as well as the dissipation loss factors in each system involved, controlled by the coefficient of sound absorption seen by the cavity and by the power variation suffered by the structure.

A leak model was proposed in the SEA calculation to introduce numerically the effect of leaks which is common in experimental tests, mainly at high frequencies (shorter wavelengths). Sound transmission loss analysis was performed for single and double panels with a porous sample. This application of double panels with interlayer treatment is well-known in the aeronautical and automotive industries.

The final phase of this work proposed a study on coupling energetic models to the finite element (FE) method. It was verified that the FE processing in the modal domain is more efficient than the direct harmonic solution. Therefore, a finite element tool in the modal domain was developed, considering the undamped modes of each FE domain in the model. Modal damping was implemented directly into the model's dynamic stiffness matrix as a proportional loss factor.

It was verified that the FE-SEA coupling of a hybrid area connection occurs from the direct field dynamic stiffness matrix being coupled to the modal FE equation. This matrix governs a FE deterministic subsystem's radiation characteristic when in contact with a reverberant SEA statistical system. From the dynamic matrix analysis, a numerical strategy was proposed to treat the singularity in the integration. Two theoretical alternatives were evaluated for the hybrid coupling, one considering integration in the modal domain and the other considering wavelet functions to obtain the solution in the wavenumber domain. A numerical technique was proposed to avoid the need of using a large number of gauss points in the wavenumber integration, which can be seen as an important contribution of this work. There was a clear computational advantage in using this technique on this application.

Finally, considering a structural FE bare system, three numerical coupling methods between finite element models (FE) and transfer matrices (TMM) were implemented. One of the methods considers a locally reactive porous sample when there is no variation in the propagation wave number along the sample's surface. The practical case in which this variation occurs and the sample becomes non-locally reactive was also considered in the numerical development, as well as an intermediate model that deals with wave propagation considering the modal wave numbers of the deterministic system under analysis. There was a similarity between responses from the three methods for the proposed case study. However, validation studies should be carried out in future research.

Although several vibroacoustic analysis techniques have been approached, this work main contributions were given in the tools development scope. These tools are expected to serve as a basis for future research in the context of computational vibroa-

coustics.

Future work

As a suggestion for future work, the following topics are proposed.

- Validations of implemented tools from experiments;
- Implementation of the direct field dynamic stiffness matrix to 1D systems to extend the functionality of the hybrid solver;
- Study of the functionality of hybrid methods to anisotropic materials

Appendix A

Numerical examples in Octave/Matlab

This appendix brings some application codes that simulates a treated plate system that can be solved by using the proposed energy approaches. The transmission loss problem was used for exemplifying the capabilities of the SEA method together with the TMM formulation. Section A.1 solves a thin plate + equivalent fluid model in terms of the Insertion Loss (IL) parameter. This quantity is applied to the SEA code for a transmission loss problem numerically exemplified in Section A.2.

A.1 Simple TMM plate-fiber problem

Figure A.1 ilustrates the problem aproached in the folowing code. The physical properties of the Plate 1 for the bare panel and Material B for the equivalent fluid material was considered in this example. All the properties are presented in Table 2.3.

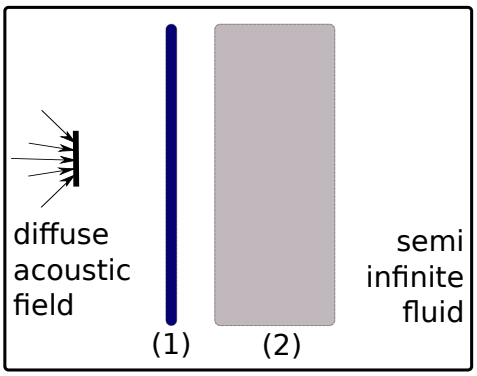

Figure A.1: TMM problem composed by a (1) bare panel layer and a (2) equivalent fluid (fiber) material.

TMM code:

```
%% TRANSFER MATRIX METHOD
%%% This code simulates the insertion loss of a plate-porous system by using
%%% the Transfer Matrix Method

clear all; close all;

v0=1; % input velocity
Ntheta = 1000; % number of angles
theta_final = 78; % THETA in degrees -field incidence

f = [250 315 400 500 630 800 1000 1250 1600 2000 2500 ...
    3150 4000 5000 6300 8000]; % third octave freq vector
j = sqrt(-1); % complex operator

   %% Air props
     Po = 101320; % atm pressure
     mu = 1.83e-5; % dynamic viscosity
     gama = 1.4; % cp/cv
     Pr = 0.71; % Prandtl number
```

```
    c0 = 343; % Sound velocity
    rho0 = 1.21; % Fluid density

  %% MATERIAL B props
    rho_1 = 9.6 ; % fiber density
    sigma = 3.872e+004; % flow resistivity
    por = 0.92; % porosity
    tor = 1.06; % tortuosity
    vis_length = 3.7e-005; % viscous length
    ter_length = 0.000148; % thermal length
    h_fib = 0.050; % thickness

  %% SOLID properties
    hplate = 0.001; rho_pla = 2700; Es = 71e9;
    eta1 = 0.01; Es = Es*(1+j*eta1); poiss = 0.33;
    D_bend = Es*hplate^3/(12*(1-poiss^2)); % bending stiffnes


%% Layers [type    h ]
layers = [1      h_fib       % fluid layer
          2     hplate    ];      % thin plate

num_layers = length(layers(:,1));
TM_fluid = zeros(2,2);
TM_solid = zeros(2,2);
Z0 = rho0*c0;

%% from eq. fluid simulation - complex wavenumber and equivalent density
    %%%%          % keq                          rho_eq
JCA_simulation = [1.4518e+01 - 2.7297e+00i   9.3692e+00 - 3.0720e+00i
                  1.7704e+01 - 4.0580e+00i   8.7653e+00 - 3.5359e+00i
                  2.1442e+01 - 5.9306e+00i   7.9679e+00 - 3.9285e+00i
                  2.5286e+01 - 8.1614e+00i   7.0980e+00 - 4.1453e+00i
                  2.9580e+01 - 1.0897e+01i   6.1452e+00 - 4.1676e+00i
                  3.4393e+01 - 1.4013e+01i   5.2060e+00 - 3.9731e+00i
                  3.9408e+01 - 1.6994e+01i   4.4473e+00 - 3.6380e+00i
                  4.5237e+01 - 1.9885e+01i   3.8382e+00 - 3.2219e+00i
                  5.3147e+01 - 2.2887e+01i   3.3357e+00 - 2.7416e+00i
```

```
                6.2163e+01 - 2.5439e+01i   3.0101e+00 - 2.3353e+00i
                7.3522e+01 - 2.7930e+01i   2.7750e+00 - 1.9782e+00i
                8.8403e+01 - 3.0588e+01i   2.5970e+00 - 1.6666e+00i
                1.0791e+02 - 3.3594e+01i   2.4580e+00 - 1.4034e+00i
                1.3077e+02 - 3.6793e+01i   2.3539e+00 - 1.2038e+00i
                1.6024e+02 - 4.0647e+01i   2.2622e+00 - 1.0355e+00i
                1.9830e+02 - 4.5338e+01i   2.1785e+00 - 8.9362e-01i
                2.4248e+02 - 5.0477e+01i   2.1076e+00 - 7.8405e-01i];

for ifreq=1:length(f) % loop frequency

  freq = f(ifreq);
  omega = 2*pi*freq;

  for itheta = 1:Ntheta % loop theta

  dtheta = (theta_final/90)*(pi/2)/(Ntheta-1); % trapezoidal integration
  theta =  (itheta-1)*dtheta;
  kt = (omega/c0)*sin(theta);

    for l=1:length(layers(:,1)) % loop layers

      if layers(l,1)==1    % equivalent fluid

          h=layers(l,2);
          ka = JCA_simulation(ifreq,1);
          rho= JCA_simulation(ifreq,2);

          k3 = sqrt(ka^2 - (kt)^2); % this is k3

          TM_fluid = [      cos(k3*h)          j*omega*rho*sin(k3*h)/k3
                        j*k3*sin(k3*h)/(omega*rho)      cos(k3*h)];
      else % solid thin plate

       m = rho_pla*hplate; % surface mass
       Z = j*omega*m*(1 - D_bend*kt^4/(omega^2*m));
       Ts11 = 1; Ts12 = -Z; Ts21 = 0; Ts22 = 1;
```

```
        TM_solid = [Ts11     Ts12
                    Ts21     Ts22 ] ;
    end % end if fluid

end % end loop layers

%% ASSEMBLING

Ift = eye(2,2); Jft = [-1 0; 0 1]; % fluid - thin plate/septum
Itf = Jft; Jtf = Ift;
D0_11 = Ift;
D0_12 = Jft*TM_solid;
D0_22 = Itf;
D0_23 = Jtf*TM_fluid;
D0_21 = zeros(size(D0_11));
D0_13 = zeros(size(D0_23));

D0 = [D0_11 D0_12 D0_13
      D0_21 D0_22 D0_23];

%%%%%%%%%%%%%%%%%%%%%%%%%%%%%%%%%%%%%%%%%%%%%%%%%%%%%%%%%%%%%%%%%%%%%%%%%%%%%%%%
%%% Applying boundary conditions -- rigid wall for last layer

    Zc = Z0/cos(theta); % sif impedance
    bcY = zeros(1,length(D0(1,:))); % zeros for the boundary line
    bcY(end-1) = -1; bcY(end) = Zc; % [-1 Zc] for sif
  %bcY(end-1) = 0; bcY(end) = 0; % [0 1] for rigid
      D = [D0
           bcY];
%%%%%%%%%%%%%%%%%%%%%%%%%%%%%%%%%%%%%%%%%%%%%%%%%%%%%%%%%%%%%%%%%%%%%%%%%%%%%%%%
%%% Piston excitation
F = -D(:,2)*v0;  % initial velocity degree of freedom - 2nd column
D_final =  [D(:,1) D(:,3:end)]; % eliminating 2nd column from D
V2 = D_final\F; % solving linear system

%%%%%%%%%%%%%%%%%%%%%%%%%%%%%%%%%%%%%%%%%%%%%%%%%%%%%%%%%%%%%%%%%%%%%%%%%%%%%%%%
%%% Acoustic indicators
```

```
Zs = V2(1)/v0; % surface impedance
R = (Zs*cos(theta) - Z0)./(Zs*cos(theta) + Z0); % reflection coeff.

T1 = (1+R).*V2(end-1)/V2(1);  % transmission factor
T1sq(itheta) = abs(T1)^2*sin(theta)*cos(theta); % square for integration

 %% BARE PANEL response
   sigma33_bare = -1/(1-(Z/Zc));
   va_bare = -sigma33_bare/Zc;
   Zs_bare = 1/va_bare;
   R_bare = (Zs_bare*cos(theta) - Z0)./(Zs_bare*cos(theta) + Z0);

   T_bare = (1+R_bare)*(-sigma33_bare);
   Tbare_sq(itheta) = abs(T_bare)^2*cos(theta)*sin(theta);

end % end loop theta

   TA = trapz(T1sq*dtheta); % trapezoidal integration treated plate
   Tbare_int =  trapz(Tbare_sq*dtheta); % trapezoidal integration bare plate
   IC(ifreq) = TA/Tbare_int; % insertion coefficient

end % end loop freq

IL = -10*log10(IC); % Insertion loss
format shortE
IL_show = [f' IL']
```

The result from this simulation is the treatment's Insertion Loss parameter. The obtained value for the studied system can be applied to the SEA simulation, as explained in the next section.

A.2 Importing the Insertion Loss to the SEA model

The obtained Insertion Loss can be applied to a structural system used in automotive or aerospace industry to simulate the NCT performance in the design phase. A SEA model cavity-plate-cavity is approached in this section and the numerical results are compared with experimental data extracted from Kulakauskas [2016]. The SEA

problem is composed by the flexural energy of the plate and longitudinal energy of the cavities. Figure A.2 illustrates the proposed example.

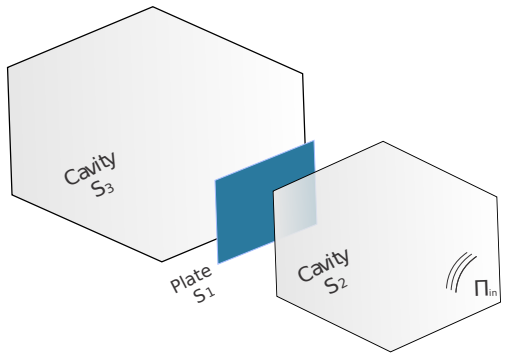

Figure A.2: Example of a sound transmission loss problem.

The problem shown in Figure A.2 can be represented by the following linear system

$$\omega \begin{bmatrix} \eta_{1,diss}+\eta_{12}+\eta_{13} & -\eta_{12} & -\eta_{13} \\ -\eta_{21} & \eta_{2,diss}+\eta_{21}+\eta_{23} & -\eta_{23} \\ -\eta_{31} & -\eta_{32} & \eta_{3,diss}+\eta_{31}+\eta_{32} \end{bmatrix} \begin{Bmatrix} E_1 \\ E_2 \\ E_3 \end{Bmatrix} = \begin{Bmatrix} 0 \\ \Pi_{in} \\ 0 \end{Bmatrix} . \tag{A.1}$$

The mean square value of the pressure inside the cavities $p_i^2 = E_i \rho_i c_i^2 / V_i$ can be recovered from the solution, with ρ_i being the fluid density, c_i the sound velocity and V_i the volume of the cavity $i = 2, 3$. The transmission loss of the partition can be calculated as ISO:10140-2 [2010]

$$TL = 10 \log_{10} \left(\frac{p_2^2}{p_3^2} \right) + 10 \log_{10} \left(\frac{S}{A_{eq}} \right) , \tag{A.2}$$

where $A_{eq} = 4\omega V_3 \eta_{3,diss} / c_3$ is the equivalent absorption area of the reception cavity and S is the area of the panel, being V_3 the volume and c_3 the sound velocity of subsystem 3.

```
clear all ; close all
% FREQUENCY 1/3 octave
freq = [250 315 400 500 630 800 1000 1250 1600 2000 2500 3150 ...
  4000 5000 6300 8000];

% Input Insertion Loss from TMM - Plate + Material B
```

```
insertion_tmm = [4.4799e-01 6.3228e-01 1.1387e+00 2.1244e+00 3.7099e+00...
    5.6754e+00 7.5447e+00 9.3200e+00 1.1134e+01 1.2660e+01 1.4151e+01...
    1.5792e+01 1.7730e+01 1.9778e+01 2.2270e+01 2.5598e+01];
  % Experimental data from the bibliography
Exp_TL = [13.4139 15.1725 17.3777 19.9746 23.2683 27.0320 30.5854 34.0621...
     37.7966 41.0511 44.2793 47.7323 51.5522 55.3433 59.6216 64.6599];
Exp_bare_panel=[13.886 14.910 16.504 19.008 20.601 21.626 ...
  23.219 24.926 26.634 28.000 30.162 32.097 33.577 34.715 36.650 36.764];
nfreqs = length(freq);

%%% SEA subsystems properties
        plate_dim = [1.006 1 0.001]; % [l b h]
        plate_props = [2700 71e9 0.33]; %[rho Youngs poisson]
        eta_diss_plate = 0.01; % diss. loss factor

        cav_dim = [70 190 147.54
                   72 209 199      ];
        cav_props = [1.21 343
                     1.21 343];
        eta_diss_cav = 0.01;
        inp_pow = 1;

        n11 = eta_diss_plate;
        n22 = eta_diss_cav; n33=n22;

  %%% coupling factors from classical models of sig rad and tau
  %%% n12 n13 n21 n23 n31 n32(Section 1.2.2)
coup_fac=[...
1.6652e-04   1.6652e-04   1.5126e-05   3.1329e-05   1.1619e-05   2.3228e-05
1.4931e-04   1.4931e-04   8.8963e-06   1.6776e-05   6.7893e-06   1.2438e-05
1.3363e-04   1.3363e-04   5.1081e-06   8.6818e-06   3.8764e-06   6.4367e-06
1.2074e-04   1.2074e-04   3.0303e-06   4.6454e-06   2.2897e-06   3.4441e-06
1.0900e-04   1.0900e-04   1.7605e-06   2.4101e-06   1.3253e-06   1.7869e-06
9.8447e-05   9.8447e-05   1.0037e-06   1.2139e-06   7.5329e-07   9.0001e-07
8.9930e-05   8.9930e-05   5.9467e-07   6.3611e-07   4.4524e-07   4.7162e-07
8.2633e-05   8.2633e-05   3.5347e-07   3.3185e-07   2.6415e-07   2.4604e-07
7.5933e-05   7.5933e-05   2.0013e-07   1.6088e-07   1.4930e-07   1.1928e-07
7.1127e-05   7.1127e-05   1.2079e-07   8.3357e-08   9.0003e-08   6.1801e-08
```

```
6.7594e-05   6.7594e-05   7.3865e-08   4.3089e-08   5.4984e-08   3.1947e-08
6.5503e-05   6.5503e-05   4.5290e-08   2.1712e-08   3.3686e-08   1.6098e-08
6.5581e-05   6.5581e-05   2.8225e-08   1.0673e-08   2.0979e-08   7.9130e-09
6.8901e-05   6.8901e-05   1.9030e-08   5.4911e-09   1.4138e-08   4.0711e-09
7.8878e-05   7.8878e-05   1.3754e-08   2.7560e-09   1.0213e-08   2.0433e-09
1.0882e-04   1.0882e-04   1.1789e-08   1.3504e-09   8.7513e-09   1.0012e-09];


%% SEA EQUATIONS
for ifreq = 1:nfreqs

    f=freq(ifreq);
    w = 2*pi*f; % circular frequency omega

n12 = coup_fac(ifreq,1); n13 =  coup_fac(ifreq,2);
n21 = coup_fac(ifreq,3); n23 = coup_fac(ifreq,4);
n31 = coup_fac(ifreq,5); n32 = coup_fac(ifreq,6);

   for ind_il = 1:2 % 1 for bare panel | 2 for treated panel

       if ind_il == 2 % it is treated panel
       IL = insertion_tmm(ifreq);
       n13 = n12*(10^(-IL/10)); n31 = n21*10^(-IL/10); % plate-cav
       n23 = n23*10^(-IL/10); n32 = n32*10^(-IL/10); % cav-cav
       end

SEA_mat = [n11+n12+n13      -n12            -n13
           -n21          n22+n21+n23        -n23
           -n31             -n32          n31+n32+n33];
Pow = [0;1;0]; % input power in the cavity
E = linsolve(SEA_mat,Pow/w);

for icav = 1:2

V = cav_dim(icav,3);
rho = cav_props(icav,1);
c =  cav_props(icav,2);
```

```
 p_sq(icav) = E(icav+1)*rho*c/V;
    if icav==2 % reception
       Aeq = 4*w*V*eta_diss_cav/c;
    end
end

S = plate_dim(1)*plate_dim(2); % surface area of the panel
TL(ifreq, ind_il) =  10*log10(p_sq(1)/p_sq(2)) + 10*log10(S/Aeq);

    end %loop IL
end % loop freq

a = colormap(gray);
figure()
set(gca, 'fontsize', 15)
semilogx(freq,TL(:,1), 'color', a(1,:), 'linewidth', 2 ); hold on
semilogx(freq,Exp_bare_panel, 's', 'color', a(1,:), 'linewidth', 2); hold on
semilogx(freq,TL(:,2),':.','color',a(140,:), 'linewidth', 3); hold on
semilogx(freq,Exp_TL, 's','color',a(140,:), 'linewidth', 2); hold on
xlim([200 8000])
ylim([10 65])
ylabel('TL [dB]')
xlabel('Frequency [Hz]')
grid on
legend('Bare Panel - SEA', 'Bare Panel - Exp', 'Treated Panel - SEA',...
    'Treated Panel - Exp','Location', 'Northwest')
```

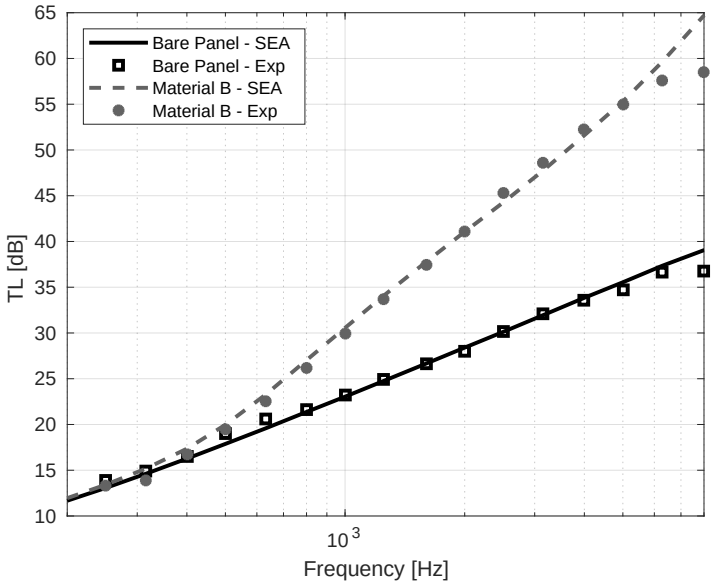

Figure A.3: Sound Transmission Loss obtained for the single-wall configuration Plate 1 + Material B. Experimental results are extracted from Kulakauskas [2016].

Bibliography

Alia, A. (2006). *Simulation numérique en vibroacoustique et en interaction fluide structure*. PhD thesis, Université de Lille.

Alimonti, L. (2014). *Development of a hybrid finite element-transfer matrix methodology for the modeling of vibroacoustic systems with attached noise control treatments*. PhD thesis, Université de Sherbrooke.

Alimonti, L. and Atalla, N. (2016). Efficient modeling of flat and homogeneous acoustic treatments for vibroacoustic finite element analysis. direct field formulations. *Journal of Sound and Vibration*, 367:84–100.

Allard, J. and Atalla, N. (2009). *Propagation of sound in porous media: modelling sound absorbing materials*. John Wiley & Sons, United Kingdon, 2 edition.

Allard, J.-F. and Champoux, Y. (1992). New empirical equations for sound propagation in rigid frame fibrous materials. *The Journal of the Acoustical Society of America*, 91(6):3346–3353.

Atalla, N. (2017). Structural and acoustic noise control material modeling. In Hambric, S. A., Sung, S. H., and Nefske, D. J., editors, *Engineering vibroacoustic analysis: methods and applications*, pages 230–265. John Wiley & Sons, United Kingdom.

Atalla, N., Panneton, R., and Debergue, P. (1998). A mixed displacement-pressure formulation for poroelastic materials. *The Journal of the Acoustical Society of America*, 104(3):1444–1452.

Atalla, N. and Sgard, F. (2015). *Finite element and boundary methods in structural acoustics and vibration*. CRC Press, Florida, USA.

BASF (2015). Acoustics Basotect B: Product description. *Technical information TI G-PMF/SM*.

Bathe, K. J. (1982). *Finite element procedures in engineering analysis*. Prentice-Hall.

Beranek, L. L. (1954). *Acoustics*. Acoustical Society of America, New York, USA.

Beranek, L. L. and Ver, I. L. (1992). *Noise and vibration control engineering: principles and applications*. John Wiley & Sons, Inc., 814 p., Cambridge, USA.

Biot, M. A. (1956). Theory of propagation of elastic waves in a fluid-saturated porous solid. ii. higher frequency range. *The Journal of the acoustical Society of america*, 28(2):179–191.

Blanchet, D. and Feist-Muench, M. (2020). Innovative acoustic material concept integration into vehicle design process. In *SAE Technical Paper*. SAE International.

Bonfiglio, P., Pompoli, F., and Lionti, R. (2016). A reduced-order integral formulation to account for the finite size effect of isotropic square panels using the transfer matrix method. *The Journal of the Acoustical Society of America*, 139(4):1773–1783.

Brouard, B., Lafarge, D., and Allard, J.-F. (1995). A general method of modelling sound propagation in layered media. *Journal of Sound and Vibration*, 183(1):129–142.

Brunskog, J. (2012). The forced sound transmission of finite single leaf walls using a variational technique. *The Journal of the Acoustical Society of America*, 132(3):1482–1493.

Cockburn, J. A. and Jolly, A. C. (1968). Structural-acoustic response, noise transmission losses and interior noise levels of an aircraft fuselage excited by random pressure fields. Technical report, WYLE LABS INC HUNTSVILLE AL TESTING DIV.

Cook, R. K. (1996). Lord rayleigh and reciprocity in physics. *The Journal of the Acoustical Society of America*, 99(1):24–29.

Cordioli, J. A. and Cotoni, V. (2009). Applications of the hybrid fe-sea method to vibro-acoustic analysis of complex engineering structures. In *Proceedings of the Brazilian Congress on Mechanical Engineering*, Gramado, RS, Brazil.

Cordioli, J. A., Gerges, S. N., Pererira, A. K., Carmo, M., and Grandi, C. (2004a). Vibro-acoustic modeling of aircrafts using statistical energy analysis. In *Proceedings of the Brazilian Congress on Mechanical Engineering*, Natal, RN, Brazil.

Cordioli, J. A., Trichês, M., and Gerges, S. N. (2004b). Applications of the statistical energy analysis to vibro-acoustic modeling of vehicles. Technical report, SAE Technical Paper.

Courtois, T., Bertolini, C., and Ochs, J. (2010). A procedure for efficient trimmed body fe simulations, based on a transfer admittance model of the sound package. *SAE International Journal of Passenger Cars-Mechanical Systems*, 3(2010-01-1405):1–13.

Cox, T. J. and D'Antonio, P. (2009). *Acoustic Absorbers and Diffusers: Theory, design and application*. Taylor & Francis e-Library, New York, USA, second edition edition.

Cremer, L., Heckl, M., and Petersson, B. A. T. (2005). *Structure-borne sound: structural vibrations and sound radiation at audio frequencies*. Springer Berlin Heidelberg, 3rd edition edition.

Delany, M. and Bazley, E. (1970). Acoustical properties of fibrous absorbent materials. *Applied acoustics*, 3(2):105–116.

Desmet, W. and Vandepitte, D. (2002). Finite element method in acoustics. In *Proceedings of the International Seminar on Applied Acoustics (ISAAC13)*, Leuven.

Elliott, S. J. and Johnson, M. E. (1993). Radiation modes and the active control of sound power. *The Journal of the Acoustical Society of America*, 94(4):2194–2204.

Fahy, F. (2000). *Foundations of Engineering Acoustics*. Elsevier's Science & Technology, Oxford, UK.

Fahy, F. J. (1994). Statistical energy analysis: a critical overview. *Philosophical Transactions of the Royal Society of London. Series A: Physical and Engineering Sciences*, 346(1681):431–447.

Folds, D. and Loggins, C. (1977). Transmission and reflection of ultrasonic waves in layered media. *The Journal of the Acoustical Society of America*, 62(5):1102–1109.

Ghinet, S. and Atalla, N. (2001). Sound transmission loss of insulating complex structures. *Canadian Acoustics*, 29(3):26–27.

Gradshteyn, I. and Ryzhik, I. (2000). *Table of Integrals, Series, and Products*. Academic Press, New York, 6th edition.

Hambric, S. A. (1990). Power flow and mechanical intensity calculations in structural finite element analysis. *Journal of Vibration, Acoustics, Stress, and Reliability in Design*, 112(4):542–549.

Hambric, S. A., Sung, S. H., and Nefske, D. J. (2016). *Engineering vibroacoustic analysis: methods and applications*. John Wiley & Sons, United Kingdom.

Horoshenkov, K. V. and Swift, M. (2001). The acoustic properties of granular materials with pore size distribution close to log-normal. *Journal of the Acoustical Society of America*, 110(5):2371–2378.

ISO:10140-2 (2010). Laboratory measurement of sound insulation of building elements: *Measurement of air-borne sound insulation*. International Standard Organization.

ISO:10534-2 (2001). Determination of sound absorption coefficient and impedance in impedance tubes: *Transfer-function method*. . International Standard Organization.

ISO:354 (2003). Acoustics: *Measuremente of sound absorption in a reverberation room*. International Standard Organization.

Johansson, D. and Comnell, P. (2010). *Statistial energy analysis software. Development and implementation of an open source code in Matlab/Octave.* Master Thesis, Chalmers University of Technology.

Johnson, D. L., Koplik, J., and Dashen, R. (1987). Theory of dynamic permeability and tortuosity in fluid-saturated porous media. *Journal of fluid mechanics*, 176:379–402.

Kang, Y. J. and Bolton, J. S. (1995). Finite element modeling of isotropic elastic porous materials coupled with acoustical finite elements. *The journal of the acoustical society of america*, 98(1):635–643.

Kulakauskas, F. L. V. Q. (2016). *Avalição do Uso de Materiais Porosos na Perda de Transmissão de Painéis Duplos*. Master Thesis (*in Portuguese*), Universidade Federal de Santa Catarina, Brasil.

Kuttruff, H. (2007). *Acoustics: An Introduction*. Taylor & Francis e-Library, New York, USA.

Langhe, K. D. (1996). *High frequency vibrations: contributions to expiremental and computational sea parameter identification techniques*. PhD thesis, Katholieke Universiteit Leuven.

Langley, R. (2007). Numerical evaluation of the acoustic radiation from planar structures with general baffle conditions using wavelets. *The Journal of the Acoustical Society of America*, 121(2):766–777.

Lauriks, W., Mees, P., and Allard, J. F. (1992). The acoustic transmission through layered systems. *Journal of sound and vibration*, 155(1):125–132.

Leppington, F. G., Broadbent, E. G., and Heron, K. (1982). The acoustic radiation efficiency of rectangular panels. *Proceedings of the Royal Society of London. A. Mathematical and Physical Sciences*, 382(1783):245–271.

Li, W. and Gibeling, H. (2000). Determination of the mutual radiation resistances of a rectangular plate and their impact on the radiated sound power. *Journal of Sound and Vibration*, 229(5):1213–1233.

Lyon, R. H., DeJong, R. G., and Heckl, M. (1995). Theory and application of statistical energy analysis.

Mareze, P. H. (2013). *Análise Da Influência Da Microgeometria Na Absorção Sonora De Materiais Porosos De Estrutura Rígida (in portuguese)*. PhD thesis, Universidade Federal de Santa Catarina.

Mareze, P. H., Pereira, M., Godinho, L., and Amado Mendes, P. (2019). Study of analytical and numerical models for diffuse field sound absorption prediction according to the porous panel dimensions. In *INTER-NOISE and NOISE-CON Congress and Conference Proceedings*, volume 259, pages 6941–6953. Institute of Noise Control Engineering.

Massahel, R. (2016). *Formulations ALE et SPH en Interaction Fluide-Structure : impact d'ondes de choc*. PhD thesis, Université de Lille.

Nieuwenhof, B. V. D., Lielens, G., and Coyette, J. P. (2008). An enhanced modal approach for random vibro-acoustics. In *Proceedings of ISMA 2008*, pages 1–15, Leuven.

Oliveira, T. (2020). Numerical evaluation of the sound transmission of a structural system with attached noise control treatments using statistical energy analysis. In *Proceedings of International Conference in Structural Dynamics (EURODYN)*, Athens, Grece.

Oliveira, T. A. (2021). 5 - noise control treatments modeling using statistical energy analysis and the transfer matrix method. In Moatamedi, M., Rahulan, T., and Khawaja, H., editors, *Multiphysics Simulations in Automotive and Aerospace Applications*, Multiphysics: Advances and Applications, pages 91–131. Academic Press.

Peiffer, A. (2016). Full frequency vibro-acoustic simulation in the aeronautics industry. In *Proceedings (Keynote) of ISMA 2016 including USD 2016 International Conference on Uncertainty in Structural Dynamics, Leuven*, pages 1–15.

Pereira, M., Carbajo San Martín, J., Godinho, L., Amado-Mendes, P., Mateus, D., and Ramis-Soriano, J. (2019). Acoustic behavior of porous concrete. Characterization by experimental and inversion methods. *Materiales de Construcción*, 69(336).

Pereira, M., Mareze, P., Godinho, L., Amado-Mendes, P., and Ramis, J. (2021). Proposal of numerical models to predict the diffuse field sound absorption of finite sized porous materials–bem and fem approaches. *Applied Acoustics*, 180:108092.

Pirk, R. and Souto, C. D. A. (2014). Deterministic, hybrid and statistical vibro-acoustic models - a methodology to detemine the vls payload fairing acoustic behaviour. *Journal of Aerospace Technology and Management*.

Putra, A., Oliveira, T., Souli, M., and Kassim, D. H. (2021). Characterizing and modeling of acoustical performance of natural sound absorber. In *Multiphysics Simulations in Automotive and Aerospace Applications*, pages 49–64. Elsevier.

Rao, M. D. (2003). Recent applications of viscoelastic damping for noise control in automobiles and commercial airplanes. *Journal of Sound and Vibration*, 262(3):457–474.

Rayleigh, J. W. S. B. (1896). *The theory of sound*, volume 2. Macmillan.

Rhazi, D. and Atalla, N. (2010). A simple method to account for size effects in the transfer matrix method. *The journal of the acoustical society of america*, 127(2):EL30–EL36.

Shorter, P. J. and Langley, R. S. (2005a). On the reciprocity relationship between direct field radiation and diffuse reverberant loading. *The Journal of the Acoustical Society of America*, 117(1):85–95.

Shorter, P. J. and Langley, R. S. (2005b). Vibro-acoustic analysis of complex systems. *Journal of Sound and Vibration*, 288(3):669–699.

Smith Jr, P. (1962). Response and radiation of structural modes excited by sound. *The Journal of the Acoustical Society of America*, 34(5):640–647.

Thaynan Oliveira, e. a. (2016). Sound absorption coefficient measurement based on the transfer function method specified by the standard iso 10534-2 using low-cost alternatives. In *Proceedings of Iberoamerican Congress on Acoustics (FIA)*, Buenos Aires, Argentina.

Thomasson, S.-I. (1980). On the absorption coefficient. *Acta Acustica united with Acustica*, 44(4):265–273.

Thomson, W. T. (1950). Transmission of elastic waves through a stratified solid medium. *Journal of applied Physics*, 21(2):89–93.

Timoshenko, S., Woinowsky-Krieger, S., et al. (1959). *Theory of plates and shells*, volume 2. McGraw-hill New York.

Tournour, M. A., Kosaka, F., and Shiozaki, H. (2007). Fast acoustic trim modeling using transfer admittance and finite element method. Technical report, SAE Technical Paper.

Vercammen, M. and Lautenbach, M. (2012). Influence of sample size on the sound absorption. *Proceedings DAGA, Darmstadt*.

Villot, M., Guigou, C., and Gagliardini, L. (2001). Predicting the acoustical radiation of finite size multi-layered structures by applying spatial windowing on infinite structures. *Journal of sound and vibration*, 245(3):433–455.

Wijker, J. J. (2009). *Random vibrations in spacecraft structures design: theory and applications*, volume 165. Springer Science & Business Media.

Williams, E. G. and Maynard, J. D. (1982). Numerical evaluation of the rayleigh integral for planar radiators using the fft. *The Journal of the Acoustical Society of America*, 72(6):2020–2030.

Zwikker, C. and Kosten, C. W. (1949). *Sound absorbing materials*. Elsevier.